Intermittency in turbulence

INTERMITTENCY
IN
TURBULENCE

Adrian Daniel Staicu

Omslagontwerp: Paul Verspaget
Druk: Universiteitsdrukkerij, TUE

CIP-DATA LIBRARY TECHNISCHE UNIVERSITEIT EINDHOVEN

Staicu, Adrian Daniel

Intermittency in turbulence / by Adrian Daniel Staicu. -
Eindhoven: University of Technology Eindhoven, 2002. -
Proefschrift. - ISBN 90-386-1545-0
NUR 926
Trefwoorden: turbulentie / intermittentie / schaling
Subject headings: turbulence / intermittency / scaling

INTERMITTENCY
IN
TURBULENCE

PROEFSCHRIFT

ter verkrijging van de graad van doctor aan de
Technische Universiteit Eindhoven, op gezag van
de Rector Magnificus, prof.dr. R.A. van Santen,
voor een commissie aangewezen door het College
voor Promoties in het openbaar te verdedigen op
woensdag 4 december 2002 om 16.00 uur

door

Adrian Daniel Staicu

geboren te Craiova

Dit proefschrift is goedgekeurd door promotoren:

prof.dr.ir. W. van de Water
en
prof.dr.ir. G.J.F. van Heijst

CONTENTS

Chapter 1

INTRODUCTION

1.1 Why turbulence?

Turbulence is a omnipresent phenomenon of Nature. In our everyday life, we either rarely notice it when swimming, driving a car, riding a bike, skating, or suddenly pay serious attention to it, when the ride gets bumpy on board a plane on stormy weather or when flying over tall mountains.

Let's imagine for a second how the early morning cup of coffee would be without it. If it weren't for the beneficial effects that come with turbulence, mixing milk and coffee would become a very tricky process. Instead of thoughtlessly stirring it with the spoon once and then wait shortly for turbulence do the rest of the work, we would have to repeat the process many times such that the fluid would be sufficiently folded over itself and the milk evenly split over the cup. Of course, there is the alternative of not touching the cup for some time and let the milk slowly diffuse, but then coffee is not enjoyable anymore when it gets cold.

However, designing the most effective method of stirring coffee is not why turbulence is important to science. Actually, the diversity of situations where we discover turbulence as an important scientific phenomenon is impressive: flow around ships and aircrafts, combustion in car engines and plane turbines, flow in the ocean, atmosphere, air flow in lungs, flow of blood in arteries and heart, flow in pipelines, even the dynamics of the financial markets can also be viewed as analogous to turbulent flows. The entire Universe appears to be in a state of turbulent motion, and turbulence seems to be a decisive factor helping in the formation of stars and solar systems, as indicated by astronomical observations and theoretical considerations in astrophysics.

From the large variety of situations mentioned above, many of them are cases in which turbulence is attractive from the point of view of the engineer, since studying it leads to technological improvement. It is more fruitful then to model regions where the turbulent flows interact with boundaries, and then learn how to control and apply them.

For the physicist, the interesting part is how the small-scale structure of tur-

bulence is organized, preferably isolated from any boundary effects. This is where universal aspects can be sought, in the sense that they should be independent of the nature of the fluid or the geometry of the problem. It is universality that makes turbulence an exciting research subject for physicists and mathematicians.

1.2 What is turbulence?

Despite of being such a familiar notion, the use of the term "turbulent" is relatively new, as Hinze clarifies in his textbook [45]. Osborne Reynolds himself, a pioneer in the study of turbulence, called it "sinuous motion". Skipping over the dictionary definition, which does not suffice to characterize the modern physical sense of the word, we stop at the definition given in 1937 by Taylor and Von Kármán: "Turbulence is an irregular motion which in general makes its appearance in fluids, gaseous or liquid, when they flow past solid surfaces or even when neighboring streams of the same fluid past or over one another". To make this more clear, we need to use the terminology of fluid dynamics. Flows of gases and liquids can be divided into two very different types: "laminar" flows, which are smooth and regular, and "turbulent", totally opposite, in which physical quantities as velocity, temperature, pressure, etc. fluctuate in a sharp and irregular manner in space and time, the latter being actually the more natural state of a flow. To illustrate how unpredictable a typical turbulent flow is, we show in Fig. 1.1 the time evolution of the velocity field simultaneously observed in different locations in the flow. The variety of time-scales and amplitudes of the velocity seen in this picture illustrates the complexity of turbulence structure. It is this structure that makes turbulence very efficient in transferring momentum and therefore an interesting subject for practical applications, such as delaying the boundary layer separation, which decreases drag forces on objects submerged in a turbulent flow.

1.3 History of turbulence

It appears that Leonardo Da Vinci was probably the first to distinguish this special state of the fluid motion and use the term "turbulence". Modern turbulence started with the experiments of Osborne Reynolds in 1883, who analyzed the conditions under which laminar flows of fluids in pipes become turbulent. The study led to a criterion of dynamical stability based on the "Reynolds number"

$$Re = \frac{UD}{\nu}, \tag{1.1}$$

where U and D are the characteristic velocity and length scales of the flow and ν is the kinematic viscosity. The Reynolds number may be interpreted as the ratio

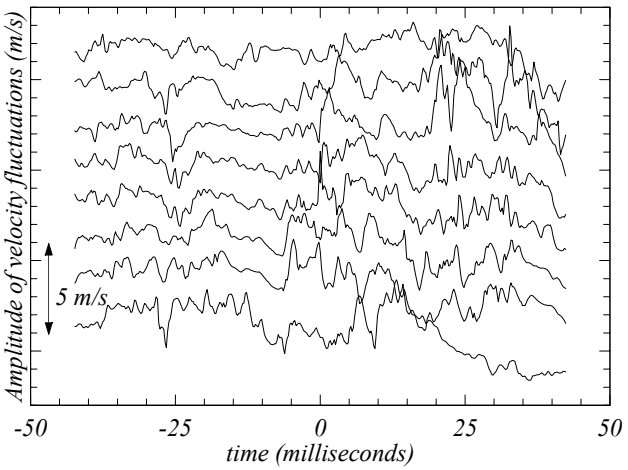

Fig. 1.1: *The fluctuations of the velocity in a turbulent flow have a irregular, complicated and unpredictable evolution in time and space, as captured in a typical measurement of turbulence produced in the laboratory, where the different traces are registered at closely spaced points. Tines were measured relative to the occurence of a violent event.*

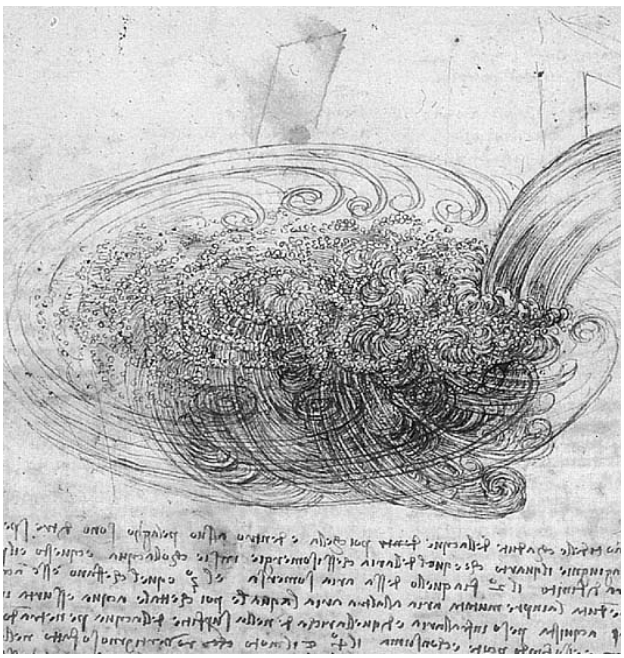

Fig. 1.2: *Drawing of a turbulent eddy by Leonardo da Vinci.*

of inertial to viscous forces present in the fluid, and for an incompressible flow, it is the only control parameter of that system. Intuitively, as Frisch points out in his book on turbulence [35], its value can also be seen as an indicator for the degree of symmetry of the flow. This can easily be imagined in the experimental situation of a flow past a cylinder. For values of the Reynolds number departing from 1, visualizations of the flow show a gradual increase of the degree of asymmetry in the flow surrounding the obstacle, before and after it.

Based on the technological interest raised by the remarkable momentum transfer properties of the large scales of turbulence, experiments in the beginning of the 20th century led to decisive advances in the theory of turbulence. Representative of this time are the so-called semi-empirical approaches made by great fluid-dynamicists, such as G. Taylor, L. Prandtl and T. Von Kármán in the 1920s and '30s, which were used to solve important practical problems.

In a remarkable paper, Lewis Fry Richardson advanced in 1922 the assumption that turbulence is organized as an hierarchy of eddies of various scales, each generation borrowing energy from its immediately larger neighbor in a "cascade" process of eddy-breakdown [75]. This picture, though more appropriate in wavenumber space, was poetically immortalized in his book inspired from observation of clouds and the verses of Jonathan Swift:

"Big whorls have little whorls,
Which feed on their velocity;
And little whorls have lesser whorls,
And so on to viscosity
(in the molecular sense)"

This era culminated with the now fundamental ideas of Andrei Nikolaevich Kolmogorov in the "theory of locally isotropic turbulence" (1941) [48]. Inspired by Richardson's energy cascade description, he assumed that with each step in the energy transfer towards smaller scales, the anisotropic influence of the large scales will gradually be lost, such that at sufficiently small scales the flow will be statistically homogeneous and isotropic. This steady situation, characterized by a mean flux of energy $\langle\epsilon\rangle$, was postulated by Kolmogorov to be universal and determined by only one parameter, $\langle\epsilon\rangle$. Moving further down the scales, there comes a length-scale where the flow gradients are so large that viscous effects can no longer be ignored. The scale is determined (in a dimensional argument) from the viscosity ν and $\langle\epsilon\rangle$

$$\eta = \left(\frac{\nu^3}{\langle\epsilon\rangle}\right)^{1/4}. \tag{1.2}$$

We introduce below the famous self-similarity hypotheses in their original form (according to Hinze [45]):

◊ (a) *"At sufficiently large Reynolds numbers there is a range of high wave-numbers (inertial-range) where the turbulence is statistically in equilibrium and uniquely determined by the parameters $\langle\epsilon\rangle$ and ν. This state of equilibrium is universal."*

◊ (b) *"If the Reynolds number is infinitely large, the energy spectrum in the inertial range is independent of ν and solely determined by the parameter $\langle\epsilon\rangle$."*

1.4 The nature of the turbulence problem

The equations that govern turbulence are essentially a form of Newton's law for the motion of a fluid that is forced (at large scales) and affected by viscous dissipation (at small-scales)

$$\frac{\partial \boldsymbol{u}(\boldsymbol{r},t)}{\partial t} + \boldsymbol{u}(\boldsymbol{r},t)\cdot\nabla\boldsymbol{u}(\boldsymbol{r},t) = -\frac{1}{\rho}\nabla p(\boldsymbol{r},t) + \nu\nabla^2\boldsymbol{u}(\boldsymbol{r},t) + \boldsymbol{F}(\boldsymbol{r},t). \tag{1.3}$$

Here the vector $\boldsymbol{u}(\boldsymbol{r},t)$ denotes the velocity field at position $\boldsymbol{r}$ at moment t, $p(\boldsymbol{r},t)$ the pressure, $\boldsymbol{F}(\boldsymbol{r},t)$ the forcing, ρ is the density and ν is the kinematic viscosity, which for air is $1.5\cdot10^{-5}m^2s^{-1}$ (at standard pressure and temperature conditions).

The equation (1.3) is known as the Navier-Stokes equation, after the physicists who added the viscous term $\nu\nabla^2\boldsymbol{u}(\boldsymbol{r},t)$, C.L.M.H. Navier in 1827 and G.G. Stokes in 1845. Through this term, the kinetic energy is no longer conserved, but lost to heat.

The Navier-Stokes equation is a continuum equation. Later on we will learn that in 3-dimensional turbulence fluid motion occurs on smaller and smaller scales if the Reynolds number increases. Still, it can be proven that these scales will never be so small that the scale of molecular graininess of of the fluid is reached. Remarkably, the argument proving this rests intimately on the Kolmogorov scaling hypotheses of turbulence, the very hypotheses that are under attack in this thesis.

The flow velocities we consider are much smaller than the velocity of sound, which gives the incompressibility condition

$$\nabla\cdot\boldsymbol{u}(\boldsymbol{r},t) = 0. \tag{1.4}$$

Given an initial state of the flow field, together with the prescription of $\boldsymbol{u}(\boldsymbol{r},t)$ at the boundaries, Eq. 1.3 suggests that the evolving field $\boldsymbol{u}(\boldsymbol{r},t>0)$ is deterministic. However, we are uncertain about the uniqueness of the solution and therefore cannot characterize the phenomenon of turbulence as *deterministic chaos*. Moreover, the number of degrees of freedom of a turbulent flow is extremely large, which warrants a statistical rather than a deterministic description. The

immense magnitude of the number of degrees of freedom N precludes the performance of direct numerical simulations of turbulent flows that can readily be made in the laboratory. With the number N increasing as $Re^{9/4}$, it will take many decades in the evolution of large-scale computing before the experiments of this thesis can be numerically simulated.

Understanding the nature of the turbulence problem is however a different story. What we need is "a method of understanding the *qualitative* content of equations" (Feynman 1963 [32]). Though it may seem rather pessimistic, Tsinober (2001 [90]) notes that there "is no consensus on what is (are) the problem(s) of turbulence and what would constitute its (their) solution. Neither is there agreement on what constitutes understanding". However, there seems to be agreement on what the culprits for this situation are:

- ◊ Nonlinearity - the term $u_i \partial_i u_j$ in the Navier-Stokes equations
- ◊ Existence and smoothness of solutions at all time
- ◊ Non-locality - to determine the local fields one has to integrate over the entire space.

A more rewarding approach to deal with the extreme complexity of turbulence is a statistical description. The Kolmogorov statistical hypotheses form the starting point of the present thesis. In fact, a major effort will be to prove that the first hypothesis needs serious amendment.

There are some other direct theoretical approaches to turbulence, but they are neither the subject of the thesis nor constitute the mainstream of turbulence research interests. We will mention that, since it is a system of interacting fields (but of non-linear nature), turbulence is similar to quantum field theory, therefore the use of diagrammatic and functional integrals has been tailored to the needs of turbulence. The main results and an introduction to this method are given elsewhere, e.g. Antonov *et al.* (1999 [3]).

1.5 Statistical approach and phenomenology

In principle, the phenomenology of turbulence is characterized by simple statistical quantities, such as averages, probability distribution functions, spectra, correlations, etc., which are calculated from data experimentally measured or from direct computer simulations. In general, the term "averaging" is never equivalent to a proper ensemble average (over all possible states of the system), but ergodicity is invoked to replace it by time-averaging or mixed time and limited spatial averaging. These tools are sufficient to reveal some of the most important universal features of turbulence.

1.5.1 Small-scales of turbulence and universality

While turbulence at large Reynolds numbers consists of a wide range of dynamical scales that contain its energy, they are bounded naturally by a largest scale at which turbulence is stirred, and a smallest scale η, defined in Eq. 1.2, where most of the energy is dissipated. By *small scales* we will understand the dissipative range close to η and the inertial range postulated by the first Kolmogorov hypothesis (a). Phenomenological studies of turbulence are mostly aimed at the study of the small scales, since it is here that universal properties of turbulence are seen, and their characterization is considered important for the "turbulence problem".

The second hypothesis of Kolmogorov (b) implies that small-scale turbulence is *isotropic and homogeneous* at sufficiently large Reynolds numbers, and its statistics will be determined only by the average dissipation rate

$$\langle \epsilon \rangle = \frac{\nu}{2} \sum_{i,j=1}^{3} \left\langle \left(\frac{\partial u_i}{\partial x_j} + \frac{\partial u_j}{\partial x_i} \right)^2 \right\rangle \tag{1.5}$$

where ν is the fluid viscosity. If we consider the histogram of the fluctuations of normalized velocity increments over a small-scale separation $\Delta u(r)/(r\langle\epsilon\rangle)^{1/3}$, it follows then from (b) that this statistical quantity should be *universal*, *i.e.* independent of the flow, Reynolds number or r. We will see next how the Kolmogorov prediction is reflected and can be quantized using simple statistical tools.

1.5.2 Structure functions and intermittency

One of the most common statistical quantities used in the phenomenology of turbulence is the *structure function*. We define the structure function of order p to be

$$S_p(r) = \langle \Delta u(r)^p \rangle = \int_{-\infty}^{\infty} \mathcal{P}_r(\Delta u) \Delta u^p \, d(\Delta u), \tag{1.6}$$

where Δu are the velocity increments and $\mathcal{P}_r(\Delta u)$ is their probability distribution function. The postulated universality of the normalized $\mathcal{P}_r(\Delta u/(r\langle\epsilon\rangle)^{1/3})$ implies that structure functions exhibit *scaling* behaviour for high Reynolds numbers

$$S_p(r) = C_p (r\langle\epsilon\rangle)^{p/3}, \tag{1.7}$$

when the separations r are within the inertial range, with C_p universal constants. The values of the *scaling exponents* $\zeta_p = p/3$ follow from the postulate. The equivalent form of the above relation for order $p = 2$ gives the well-known scaling law for the energy spectrum

$$E(k) = C\langle\epsilon\rangle^{2/3} k^{-5/3}. \tag{1.8}$$

The only known exact relation for structure functions can be derived directly from the Navier-Stokes equations, namely the Kolmogorov 4/5 law

$$S_3^L(r) = -\frac{4}{5}\langle\epsilon\rangle r. \tag{1.9}$$

For high orders $p \geq 4$, it is well-known the that scaling exponents ζ_p deviate from the Kolmogorov dimensional prediction, that is $\zeta_p < p/3$. These deviations are known as anomalous scaling and imply that the form of the probability distributions $\mathcal{P}_r(\Delta u)$ will vary inside the inertial range, such that with the decrease of the scale towards the dissipative range, their "tails" will be increasingly flared out. This phenomenon is called *intermittency* and the *anomalous scaling* is a measure of it, since higher orders emphasize increasingly larger velocity excursions $\Delta u(r)$.

To account for intermittency, the refined (RSH) versions of the self-similarity hypotheses were proposed by Kolmogorov (1962) [49], which incorporated the suggestion of Obukov that the mean energy dissipation rate exhibits strongly non-Gaussian fluctuations. In the case of anomalous scaling, one defines a local mean dissipation rate

$$\epsilon_r(\mathbf{r}, t) = \int_{V_r} \epsilon \, dV, \tag{1.10}$$

such that its own scaling exponents

$$\langle\epsilon_r\rangle^p \sim r^{\tau_p} \tag{1.11}$$

will contribute to the new scaling

$$\langle\Delta u^p(r)\rangle = C'_p(\langle\epsilon_r\rangle r)^{p/3} \tag{1.12}$$

with exponents

$$\zeta_p = p/3 + \tau_p \tag{1.13}$$

Implicitly, the constants C'_p lose their universality (the famous "Landau objection", originally formulated in 1944 [52]). The failure of the Kolmogorov theory to explain the anomalous scaling does not stop here however. Continuous improvement of experiments on intermittency brings increasing evidence that a description of turbulence beyond the Kolmogorov formulation, which dominated the turbulent research for more than half a century, is acutely needed. A number of intermittency models were proposed, which attempt to explain in particular the anomalous scaling exponents. The most popular model to explain the anomalous scaling exponents is the multifractal model of Frisch (1985 [66]).

1.5.3 The multifractal model

In the Richardson cascade picture, when a mother-eddy breaks up into smaller daughter eddies, they uniformly occupy the entire space. In the fractal description, the resulting eddies will occupy only a fraction $0 < \beta < 1$ of the initial volume. Therefore, the fraction of the space that remains active at scale r (after some n breakdowns of the largest eddies r_0) is

$$p_r = \beta^n = \left(\frac{r}{r_0}\right)^{3-D} \tag{1.14}$$

Here the notation $3 - D$ justifies the interpretation of D as a *fractal dimension*. Then the energy flux (per unit mass) at scale r is

$$\Pi \sim \frac{E_r}{t_r} \sim p_r \cdot \frac{v_r^2}{t_r} = \frac{v_r^3}{r}\left(\frac{r}{r_0}\right)^{3-D} \tag{1.15}$$

which in the inertial range should not depend on the scale and therefore can be computed at the large energy injection scale

$$\langle \epsilon \rangle \sim \frac{v_0^3}{r_0}. \tag{1.16}$$

The two relations (1.15) and (1.16) lead to a scaling exponent for the velocity field

$$v_r \sim v_0 \left(\frac{r}{r_0}\right)^h \tag{1.17}$$

where

$$h = \frac{1}{3} - \frac{3-D}{3}. \tag{1.18}$$

If rather than being single valued, the turbulent flow is assumed to possess a continuous range of scaling exponents h, then for each h there is a set $\mathcal{S}_h \in \mathbb{R}^3$ of fractal dimension $D(h)$ in which the velocity scales with this exponent. When we sum over all sets to compute the total scaling of the structure function

$$\frac{S_p(r)}{r_0^p} \sim \int d\mu(h) \left(\frac{r}{r_0}\right)^{ph+3-D(h)} \tag{1.19}$$

where $\mu(h)$ reflect the different weight of different fractal sets. In the limit $r \to 0$, the power-law with the smallest exponent will dominate, such that the scaling exponent of the structure function will be

$$\zeta_p = \inf_h [ph + 3 - D(h)] \tag{1.20}$$

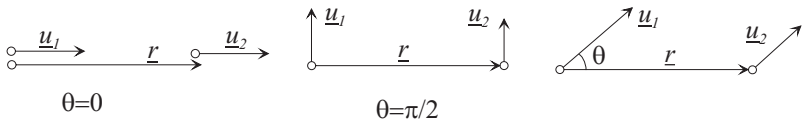

Fig. 1.3: *Geometries in which structure functions can be measured.*

irrespective of the weights. It can be seen that the dimensions $D(h)$ and the scaling exponents are related by a *Legendre transform*, such that the inverse

$$D(h) = \inf_h [ph + 3 - \zeta_p] \tag{1.21}$$

can be used to experimentally measure the deviations of the fractal dimension $D(h) \leq 3$ from the scaling exponents. So far, the multifractal model does not explain the anomalous scaling exponents, other than stating that anomalous scaling is equivalent to a non-trivial value of the multifractal dimension function $D(h)$. However, it is possible to construct more explicit models which do predict numerical values of the scaling exponents. One example is the log-Poisson model by She and Leveque [80], which reproduces the scaling exponents that are measured experimentally.

1.6 Geometry: the theme of the thesis

In the previous section we have encountered a geometric description of the organization of turbulent fluctuations: the multifractal model. Geometry is a central theme in this thesis. The velocity field $\boldsymbol{u}(\boldsymbol{r}, t)$ is a vector field that depends on the position $\boldsymbol{r}$. So far, we have ignored this circumstance when we have considered the velocity magnitude $\Delta u(r)$ of eddies with size r irrespective of the orientation of the vectors $\Delta\boldsymbol{u}$ and $\boldsymbol{r}$. Clearly, the turbulent velocity field is much richer and we will have to bring in its vector character to describe its fluctuations.

A simple extension of the traditional experiments results if we realize that we can choose a relative orientation of the vectors $\Delta\boldsymbol{u}$ and $\boldsymbol{r}$, with the extremal situations called longitudinal, if they point in the same direction and transverse if they are orthogonal. These geometries are illustrated in Fig. 1.3.

The extensive literature on scaling issues in turbulence is dominated by studies of the statistics of longitudinal increments. The reason is that these are easily accessed experimentally: a time series of velocity fluctuations measured using a stationary probe in a turbulent flow with a relatively large mean velocity component U suffices. Through invocation of Taylor's frozen turbulence hypothesis time differences τ can be translated into spatial separations r as $r = U\tau$. In Chapter 4 of this thesis we describe a concentrated effort to use more sophisticated

instrumentation needed to measure the statistics of $\Delta\boldsymbol{u}(\boldsymbol{r})$ at an arbitrary relative orientation of $\Delta\boldsymbol{u}$ and $\boldsymbol{r}$.

Intermittency is caused by extreme velocity excursions that happen more often than expected on basis of Gaussian statistics. It is believed that these velocity excursions are caused by strong concentrated vortical events (the "sinews of turbulence" [56]). In Chapter 3 we devise tools to capture these events in an experiment. Naturally, these tools rely on the geometry of the detection technique. We argue that some geometrical arrangement is more efficient in capturing concentrated vortices than others, and that the measured intermittency depends also on this arrangement.

At large scales, turbulence is always driven anisotropically. In our experiments, this is the consequence of the way we stir turbulence using special grids through which we pass our windtunnel flow. In almost all practical applications, turbulence is stirred anisotropically. This implies that small scales forget the way in which turbulence is stirred, which is extremely important for the design of turbulence models for practical calculations of turbulence flows.

At least remnants of anisotropy remain at small scales and the question is how to describe these weakly anisotropic fluctuations. An exciting recent idea [55] is to expand these anisotropies in terms of irreducible representations of the rotation group. There is a beautiful analogy between this description and the well-known concept of angular momentum in quantum mechanics. In Chapter 4 we critically evaluate these ideas and describe experiments aimed to detect the irreducible representations in turbulence.

In recent years, the concept of universality in turbulence came under considerable pressure, triggered not only by the non-unique aspects of scaling (such as observed in Chapter 3), but also because large-scale anisotropies seem to survive at dissipative scales, even at very high Reynolds numbers. In Chapter 5, we examine this possibility by investigating the scaling properties and small-scale strong events in a flow with a simple large scale anisotropy: homogeneous shear turbulence. This type of turbulence has a constant mean velocity gradient, but its (second-order) statistical properties are constant. The question then is if the large scale gradient survives at small scales. Through the measurement of structures and structure functions we find that these gradients are actually amplified in extremely strong events which carry almost all the large-scale velocity difference over a few Kolmogorov scales.

In Chapter 6 a classical problem of turbulence is treated: the deviations from Gaussianity of the velocity derivatives statistics. Variations in the derivative statistics are studied in two geometrical configurations (longitudinal and transverse), over a range of Reynolds numbers $Re_\lambda \approx 450 \ldots 800$. This investigation is motivated by a suspected transitional behaviour around $Re_\lambda \sim 600$ [9], attributed to

breakdown of small-scale coherent flow structures. Since the transition signifies the occurrence of another type of turbulence at very large Reynolds numbers, we deemed it worthwhile to scrutinize this extremely intriguing suggestion. Here the Reynolds number is defined as

$$Re_\lambda = \frac{u'\lambda}{\nu}, \tag{1.22}$$

where u' is the r.m.s. of the velocity fluctuations and the Taylor micro-scale λ is defined by the relation

$$\frac{u'^2}{\lambda^2} = \left\langle \left(\frac{\partial u}{\partial x}\right)^2 \right\rangle. \tag{1.23}$$

We will show that the transition can be caused by insufficient resolution of the instrumentation, which affects the two experimental geometries used in different ways.

Our interest in the geometry of turbulence culminates in a final chapter where we directly explore the fractal geometry of turbulence. If fractals form indeed a relevant tool to understand turbulent flow, we wonder whether it is possible to stir turbulence in a fractal manner. In Chapter 7 we stir turbulence using objects which have a fractal structure. The strong turbulent wakes resulting from three such objects with different fractal dimensions are studied, in an attempt to relate the self-similar behaviour of turbulence to the inner scaling of the fractals. We find evidence of the distinct fractal contamination in the dissipative tail of the spectrum.

Chapter 2

EXPERIMENTAL METHODS

2.1 Introduction

In this chapter we introduce the experimental setup that was used to generate and measure high Reynolds number windtunnel turbulence. Before we proceed with the actual description, it is useful to go over some of the factors that were taken into account prior to establishing the experimental method. Since the geometric facets of turbulence are central in this work, it is essential to employ an experimental technique that probes the spatial structure of the turbulent velocity field. Experimentally, this is achievable if the velocity fields can be captured simultaneously at different locations in the flow. Large Reynolds numbers, a prerequisite for observation of universal aspects in turbulence, are synonymous to a large dynamical range of scales. It is important that they can all be properly resolved experimentally.

These requirements prompted us to choose multipoint hot-wire anemometry as the measurement technique. We will start this chapter with introducing this reliable experimental method (section 2.2).

In section 2.2.1 we present the windtunnel facility and the mechanism used for stirring turbulence. The characteristics of the turbulent flows studied in this thesis can vary significantly, depending on the particular aspect of turbulence that is investigated. We will therefore restrict the discussion here to general considerations, but we will treat each new experimental configuration as the thesis progresses.

In section 2.2.2 we describe the array of hot-wire probes that is employed for capturing the turbulent velocities. The use of such a tool will be justified, when we evaluate (section 2.2.3) the Reynolds number and the size of the small-scales that are expected in our windtunnel, and the accuracy with which they will be resolved in our experiments.

The use of sensors arrays is a next step in turbulence instrumentation, that has, so far, been based on precise point measurements of the velocity field. Arrays of probes require accurate velocity calibration of the probes. We will describe a

new technique to achieve this. The prime quantity of interest is the structure function; it turns out that our calibration technique greatly improves the quality of measured structure functions.

In section 2.3.3 we analyze the problems inherent to computing structure functions of high orders. We see that long duration experiments are needed to insure the convergence of high-order statistics.

2.2 Hot-wire anemometry

A velocity sensor for hot-wire anemometry essentially consists of a very thin (of the order of microns in diameter) wire of tungsten which is electrically heated. When the sensor, with a length of the order of 200 μm, is exposed to a flow of air, the cooling of the wire is compensated by an electronic device, usually an electronic bridge that monitors the variations of the wire's resistance. A fast adjustment in the voltage supplied to the wire, needed to restore its temperature to a constant initial value, reflects the velocity of the flow at the sensor location. When the hot-wire sensors are small enough and they are accompanied by suitable fast-response electronics, they can resolve the instantaneous turbulent velocity fluctuations in high Reynolds-number flows. This technique is called constant temperature anemometry (CTA).

While it appears to have been used as early as 1909 (according to Tsinober (2001 [90])) and despite its conceptual simplicity, constant temperature hot-wire anemometry remains a very flexible and wide-spread measurement method of fluid dynamics. For the measurements of turbulence of moderate intensity, a decisive factor that makes it so popular is the ability to capture intermittency effects. In fact, hot-wire anemometry is still the only reliable technique to study intermittency in strong turbulence, no wonder it is the measurement technique of choice in this thesis. Let us briefly contrast it to other modern techniques and argue why these are unsuited. Modern, non-intrusive optical techniques are laser-Doppler anemometry and particle image velocimetry.

Laser-Doppler velocimetry is based on the scattering of light off a particle that passes a narrow and well-defined scattering volume. The velocity of the particle is inferred from a Doppler shift of the scattered light. Measuring intermittency is concerned with measuring statistical properties of the velocity field. The problem with laser-Doppler velocimetry is that in high velocity regions, more particles pass the measurement volume in a given time interval than in low velocity regions. Therefore, high velocity episodes have a larger weight in the statistics than low velocity spells. There is no way to correct measured high-order statistics for this effect. Thus, laser-Doppler velocimetry is unsuited for intermittency studies.

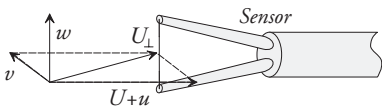

Fig. 2.1: *The hot-wire sensor is sensitive only to the velocity component perpendicular to it, $U_\perp$, if the fluctuations u, v, w are small relative to the mean velocity U.*

Particle image velocimetry (PIV) is a technique in which (a planar cut of) the velocity field is inferred from snapshots of the distribution of particles in the measurement plane. By correlating these snapshots it is possible to obtain a 2-dimensional projection of the velocity field in the measurement plane. Since, as laser-Doppler velocimetry, PIV is also based on seeding the flow with particles, a first problem is that the particle density needs to be large enough to resolve the smallest scales in the flow. In air flow, where the generation of strong turbulence can be done most readily, this demands a very high density of added scatterers. A second problem is that the deduction of velocity vectors from the correlated images is not always unambiguous and particle image velocimetry must involve a validation step in which the "improbable" velocity vectors are rejected. The trouble is that such velocities may precisely be caused by intermittency.

The precision of hot-wire anemometry as a measurement method has improved considerably since its introduction, but it should be noted that its application can be a very frustrating experience. A.E. Perry, who is internationally renowned for his contribution to this measurement technique, argued that "it leads many people not only to worry about the calibration of the instrument, but also about the calibration of the person carrying the measurements". His book (1982 [69]), together with that of Bruun (1995 [13]), provide an introduction to the technique and an extensive bibliography.

It is obvious that the cooling of a heated wire is quite insensitive to the direction of the incoming velocity vector in the plane perpendicular to the wire. However, if there is a relatively large mean flow in this plane, mainly the component in the direction of the mean flow is detected. As Fig. 2.1 illustrates, the velocity $U_\perp$ that determines the cooling of the wire is the vector sum of the mean U and fluctuating (u, v) components, and has the size

$$U_\perp = \left((U+u)^2 + v^2\right)^{1/2}, \tag{2.1}$$

which equals $U_\perp = U + u$ to first order in u/U and v/U. With a single wire, therefore, an unambiguous assignment of the signal to the $u-$component of the velocity field is only possible if the turbulent fluctuations are relatively small. It is

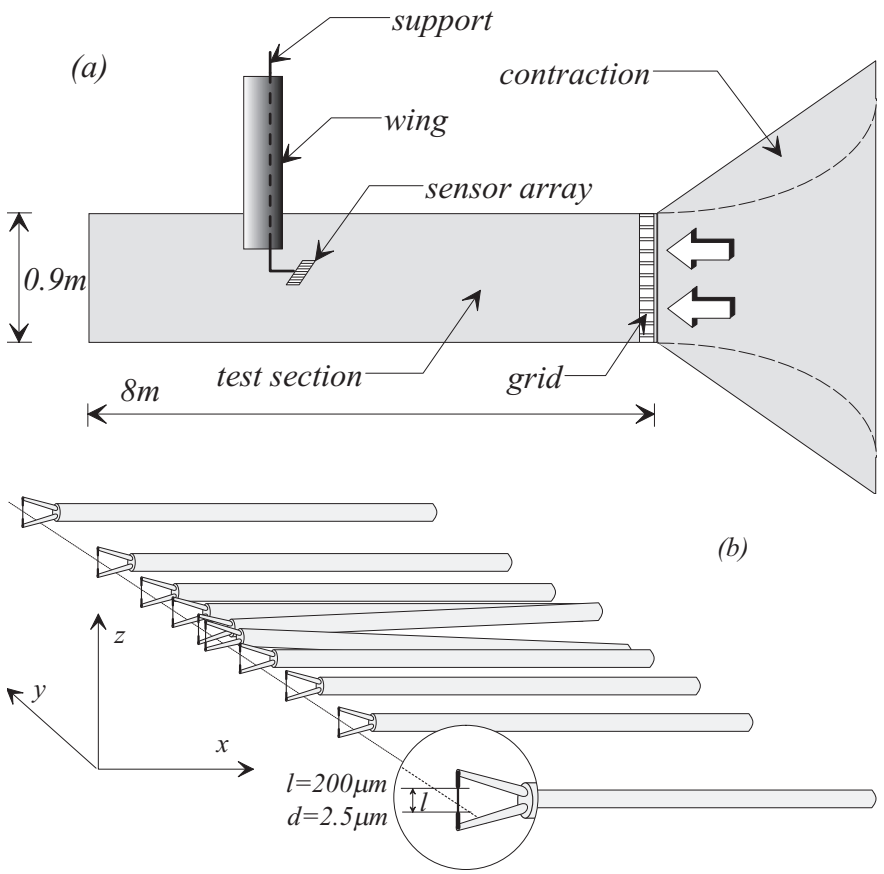

Fig. 2.2: *(a) Sketch of the windtunnel facility where the experiments were performed. (b) Close-up of the array arrangement of the 10 hot-wire sensors used to measure turbulent velocity fluctuations.*

also possible to construct probes with more sensing parts, the simplest one consisting of two perpendicular hot wires (often called $\times$-probe), which can measure simultaneously two components of the fluctuating velocity.

2.2.1 Windtunnel turbulence

Generating an appropriate turbulent flow is of great importance in this work. A relevant example is given in chapter 5, where observation of novel scaling properties in homogeneous shear turbulence owes mainly to the special care with which we designed the turbulence stirrer. The form of the stirrer can vary significantly depending on the type of turbulent flow that is investigated, therefore it will be described in detail with every new experimental setup.

Our principal method of creating turbulence is to pass the laminar flow of

a windtunnel through a planar passive grid, which serves as turbulence generator (see Fig. 2.2(a)). A classical example of a grid, which will however not be used here, consists of equally spaced vertical and horizontal rods that cover the windtunnel cross-section. The grids that we will employ can depart more or less from this design, but they all serve the same purpose, that of creating a strong turbulent wake behind them. The only slightly different situation will be encountered when fractal objects are used to play the role of the grid (chapter 7), but then the stirrer has a 3-dimensional structure. The turbulent flow achieves a stationary state at some position downstream, where it is intercepted by an array of 10 single hot-wire sensors, which will be described in the next section.

The width of the recirculating windtunnel, not shown in Fig. 2.2(a), is $W = 0.7m$. The air flow is driven by an electric turbine that can produce a laminar flow with a maximum velocity of $22m/s$. When a grid is used, its solidity (obstructing areas) cause the mean velocity of the flow to decrease substantially, such that the mean velocity of our flows will always be less than $15m/s$.

2.2.2 The hot-wire array

A closer look at the array of sensors is given in Fig. 2.2(b), where we can see that the 10 probes are positioned at various separations, such that each of the 45 pairs is characterized not only by a different spacing, but also that increasing separations are approximately exponentially spaced. The scaling properties of structure functions refer to an algebraic dependence of velocity differences on the distance over which they are registered. This dependence can be studied in log-log graphs, in which exponentially spaced distances come equidistantly.

The smallest and largest separations between two probes are chosen to resolve (if possible) the dissipative scales of the turbulent flow and the homogeneity of the large forcing scales. To avoid cross-talking of different sensors, the separation of probes in the closest pair, situated in the center of the array, was limited to approximately $1mm$.

The support of the array is approximately $25cm$ wide (which is also the largest separation of a pair of probes) and can be rotated in various positions and additionally translated vertically by a computer-controlled stepper motor. This feature serves for checks of flow homogeneity.

Each of the sensors in the array is made of tungsten/platinum wire of $2.5\mu m$ diameter and has a sensing part of $200\mu m$. The remaining length of the wire and the welding to the supporting prongs are gold-plated to improve electrical conduction.

The sensors are controlled by 10 digital constant temperature anemometers (CTA channels) that were manufactured in our group. Their signals are digitized

using a 10-channel 12-bit analog-to-digital converter (ADC) that samples them simultaneously at 20kHz each, after they have been appropriately low-pass filtered. The CTAs have been adjusted and the turbulence frequency spectra that they measure are checked against a high-quality CTA produced by the Danish company Dantec Dynamics. Finally, data which routinely amount to more than 10^9 velocity samples are stored on the hard-disks of a computer. Before each measurement, the array of wires is calibrated in laminar flow, by using either the flow produced by a separate nozzle or the flow of the unobstructed windtunnel. For the first method, a computer-controlled calibration unit (producing variable speed laminar flow) is mounted on a positioning system that moves sequentially in front of each sensor and calibrates it. The calibration itself consists of varying the known laminar velocity to which the sensor is exposed and recording the corresponding changes of the wire voltage in calibration curves. The entire procedure, including the readings of a built-in Pitot tube that monitors the laminar flow, was automated such that in a relatively short time a large number of sensors can be handled .

Comparable results are obtained when the calibration is done with the windtunnel flow in the absence of a grid, when the procedure is considerably shortened, but the flow can be slightly turbulent even when the sensor array is far from the boundary layers.

For the translation of the calibration curves from each sensor into velocities in an actual measurement, we use the "look-up" table method. To simplify the procedure, we keep from the calibration voltage-velocity curves only the coefficients of a 4th order polynomial fit.

Since the windtunnel is of recirculating type, the continuous energy injection will cause a slow rise in the air temperature inside it. This has a small effect on the amplitude of the measured turbulent velocity fluctuations, but causes errors in the determination of the mean velocity of the flow (Fig.2.3). This effect can be understood from the working principles of hot-wire anemometry. Since the calibration of the hot-wires is performed at a different initial temperature, the overheating factor of the sensors will slowly change when the temperature in the windtunnel varies. To implement an appropriate correction for this effect, we additionally sampled the air temperature in the windtunnel at short time intervals. When analyzing registered time-series, all probe calibration tables are recomputed every few seconds using the recorded windtunnel temperatures.

2.2.3 Resolving small-scale quantities

Our flow diagnostics was designed to resolve both the smallest and the largest scales in turbulence, the largest scale L was set by the typical size of a grid mesh

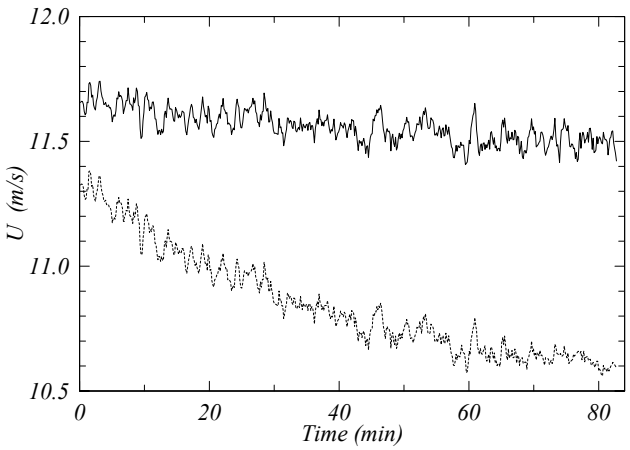

Fig. 2.3: *Correction for the air temperature drift in the windtunnel during an extended experimental run prevents a measuring a wrong value (dashed curve) of the mean velocity. The noise in the curves reflects the short time intervals from which the "local" mean velocity is calculated (approximately 5 seconds).*

which is $L \sim 0.1m$. With a mean velocity of $15ms^{-1}$, this gives a large-scale Reynolds number of

$$Re = \frac{L \cdot U}{\nu} \approx 10^5, \tag{2.2}$$

Since the ratio of the forcing and dissipation scales grows like $L/\eta \sim Re^{3/4}$, we estimate the dissipative scales in our windtunnel to be as small as

$$\eta \approx 10^{-4}m, \tag{2.3}$$

with actual measurements slightly larger than this value ($\eta \geq 1.5 \cdot 10^{-4}m$). This scale is several times smaller than the separation between the closest sensors, but from the high value of the frequency used for sampling the time-signals, we can resolve comparable time-scales

$$1/\tau = \frac{U}{2\pi\eta} \cong 1.6 \cdot 10^{-4}m. \tag{2.4}$$

It is obvious that the accuracy in resolving the dissipative scales using this configuration will be slowly lost when the Reynolds number grows. The manner in which this phenomenon develops and affects specific dissipative statistics is described in detail in chapter 6. To avoid such complications, an ideal situation would be to construct sensors that are an order of magnitude smaller than the estimated dissipative scales. Using conventional (micro-) mechanical engineering,

this is an impossible task as it would require handling of wires that have a mere thickness of $0.25\mu m$. In the past decade there have been several serious attempts to produce velocity sensors using micro-machining. However, these sensors have not yet matured.

Insufficient resolution of the small-scales is an acute problem of present-day experimental turbulence, since an increase in the Reynolds number invariably decreases the dissipative scale $\eta \sim Re^{-3/4}$. High Reynolds numbers are however indispensable to the study of universal aspects of turbulence. Only in such flows, a clear separation from the anisotropic effects of the large forcing scale and the viscous scale can be achieved, and without it, it is very difficult to argue that we measure universal aspects and not some finite-size exotic behaviour.

Using high energy injection, or using gases with a smaller kinematic viscosity than air at room temperature and atmospheric pressure, it is possible to create large Reynolds-number flows in the laboratory. Examples are the experiments on cryogenic helium gas by Tabeling *et al.* [87, 29], who reached Reynolds numbers of $Re_\lambda \cong 5000$, and the possibility to work with air at high pressure. However, with laboratory-size injection scales, the dissipative scales in these flows will be very small, so small that no adequate instrumentation exists to resolve them. A natural, but expensive solution would be to move to very large scale setups. In this respect we mention the experiments performed by Gagne *et al.* [39] in the return channel of the ONERA S1 high-speed windtunnel in France, which has a cross-section of $45m^2$and has a Taylor-microscale Reynolds number $Re_\lambda \sim 2500$, but where the dissipative scales remain large ($\eta \sim Re_\lambda^{-3/2}$). The construction scales related with such projects translate in an inflexibility in controlling the flow properties; actually the gain in the Reynolds number domain is less impressive. Combined with an ingenious design of the stirrer, the turbulence achieved in the present work will have a Re_λ as high as 860.

However, clear steps ahead in the progress of experimental turbulence will not be made unless new measurements methods emerge. There are however positive signals that we are going in the right direction: for example, positron-collider detector technology was borrowed to resolve microscopic scale trajectories of a particle carried by turbulence at an incredible rate of 70,000 frames per second (see Porta *et al.* [71]). Another exciting technology is to spectroscopically tag molecules at small scales in turbulent air flow (Noullez *et al.* [61]). This is a non-intrusive optical method that does not suffer from either velocity bias or seeding problems that plague laser-Doppler anemometry or particle image velocimetry.

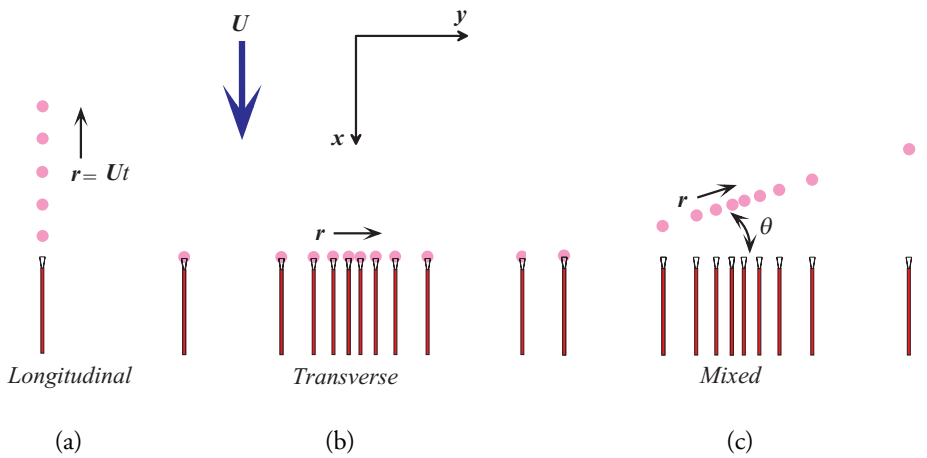

Fig. 2.4: *Methods of calculating velocity differences using a transverse sensor array.*

2.3 Measuring structure functions

2.3.1 Velocity increments

For the measurements of the structure functions of some order p, one needs to compute the time-average of the velocity differences over a separation $\boldsymbol{r}$

$$S_p = \langle [u(\boldsymbol{x}+\boldsymbol{r},t) - u(\boldsymbol{x},t)]^p \rangle. \tag{2.5}$$

To achieve this, there are essentially two alternatives, whenever an array of sensors is used. The simplest method to evaluate velocity differences is by considering time-delays $u(\boldsymbol{r}, t_0+t) - u(\boldsymbol{r}, t_0)$, when only the time-series of single sensors (placed at some fixed position $\boldsymbol{r}$) are involved. The typical low-intensity of wind-tunnel turbulence justifies the re-interpretation of the time-lags as longitudinal separations, or what is known as the *Taylor hypothesis*. If the intensity of turbulence is $u/U \ll 1$, then

$$u(t_0, x) = u'(t_0, x - Ut), \tag{2.6}$$

or simply $\Delta x = U \cdot t$. This situation and the choice of the coordinates are illustrated in Fig. 2.4(a). Then the velocity difference is

$$u(x+\Delta x, t_0) - u(x, t_0) = \Delta u(\Delta x) \equiv \Delta u^L(r), \tag{2.7}$$

and we can construct the *longitudinal* structure functions.

The most obvious way to construct velocity increments in the present configuration is when the velocities u recorded by different sensors situated at locations

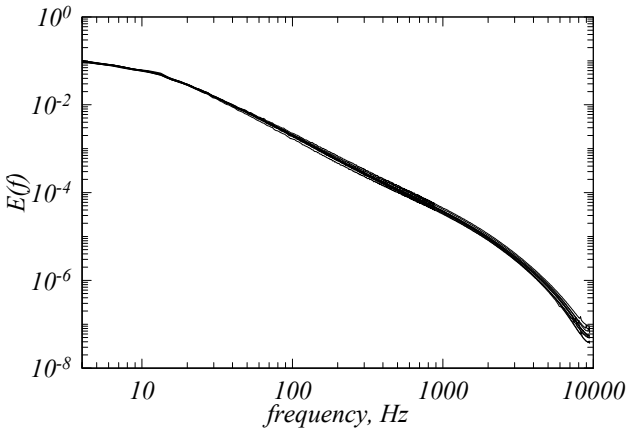

Fig. 2.5: *Small differences in the dynamical response of different sensors are revealed by the turbulence spectra measured in homogeneous flow experiments.*

y_i, y_j are compared at equal time, which is equivalent to saying that the vector r points *transversely* to the measured velocity component

$$u(y_i, t_0) - u(y_j, t_0) = \Delta u(\Delta y) \equiv \Delta u^T(r), \tag{2.8}$$

such that we can calculate *transverse* structure functions (see Fig. 2.4(b)). The obvious benefit is that the Taylor hypothesis is not needed in this case.

In general, in longitudinal velocity increments the vector r points in the same direction as the measured velocity component, whereas they are at right angles in the transverse case. In chapter 4 we will explain how to measure increments at any angle (Fig. 2.4(c)). Of course, when we want to capture the spatial structure of the flow in a direction perpendicular to the mean flow, we have to use an array of hot-wire sensors.

2.3.2 Compensating for sensor differences

One of the great advantages of the used transverse arrangement is that spatial separations are explicit, and do not follow implicitly from Taylor's hypothesis. A problem is, however, that velocities at different points are measured by different probes whose characteristics may slightly differ. This problem is absent in the longitudinal direction, where these velocities are measured using the same probe through time delays.

In principle, the calibration procedure that precedes each experiment takes care of the different probe characteristics. However, the calibration procedure only pertains to the *static* response of the wires, and it would apply at all frequencies if the wires and the control electronics would not have any dynamics of

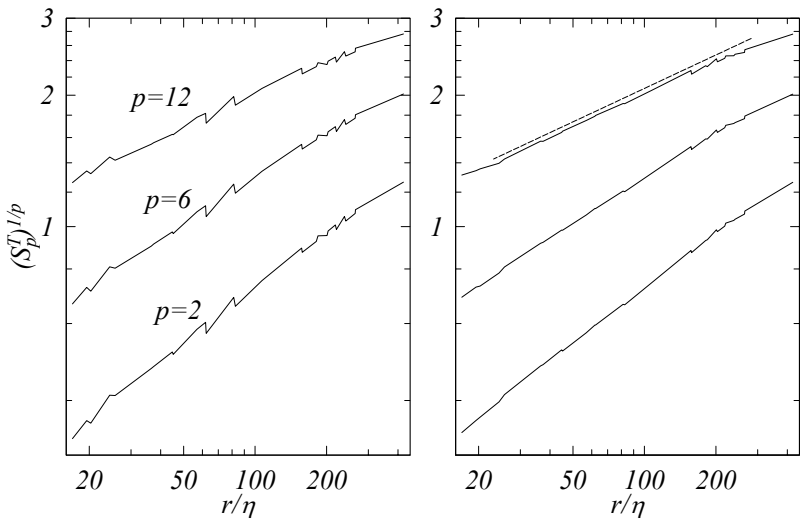

Fig. 2.6: *The effect of instrumentation noise on transverse structure functions, before (left) and after (right) correction using Eq. 2.12.*

their own. This is not the case, and the dynamical characteristics may vary from one wire to another and from one CTA controller to the next.

These differences manifest strongest when contributions from all sensors are combined to compute the transverse structure functions $S_p^T(r)$.

With 10 probes, each of the 45 discrete separations r involve a different pair of probes at the locations y_i, y_j, $r_{ij} = y_i - y_j$. The slightly different dynamical response of the members of each of the 45 different pairs causes a (systematic) error in the statistics of te corresponding velocity increments $\Delta u_{ij} = u_i - u_j$.

The entire situation can become very frustrating when the purpose of the experiments is to fit scaling exponents to transverse structure functions. To illustrate this, we show in Fig. 2.6 how the relative noise of different channels manifests in large (systematic) fluctuations in the measurement of transverse structure functions. We propose a simple correction method that drastically improves the quality of the structure functions and allows the determination of scaling exponents with better accuracy.

Due to a different dynamical response, different probes may measure slightly different turbulent intensities $\langle u^2 \rangle^{1/2}$. As a first step, this may be corrected for by replacing Δu_{ij} with

$$\widetilde{\Delta u}(\Delta y_{ij}) = u_i \frac{\overline{\langle u^2 \rangle}^{1/2}}{\langle u_i^2 \rangle^{1/2}} - u_j \frac{\overline{\langle u^2 \rangle}^{1/2}}{\langle u_j^2 \rangle^{1/2}}, \tag{2.9}$$

where for M sensors $\overline{\langle u^2 \rangle}$ is the averaged squared turbulent velocity

$$\overline{\langle u^2 \rangle} = \frac{1}{M} \sum_{i=1}^{M} \langle u_i^2 \rangle. \tag{2.10}$$

However, the turbulent intensity is only an average over the energy spectrum,

$$\langle u_i^2 \rangle = \int_0^\infty E_i(f)\, df, \tag{2.11}$$

whereas the difference in dynamical response between wires may be a function of frequency. That this is actually so is illustrated in Fig. 2.5, where we show the frequency spectra of each wire of the array, measured in homogeneous turbulence. These frequency spectra are seen to be slightly but significantly different.

To make a frequency dependent correction, the idea is to normalize velocities such that each probe of a given pair sees the same turbulent energy at the wavenumber k_x set by the probe separation r_{ij}, $k_x = 2\pi/r_{ij}$. Instead of energy spectra, we will work with the second order structure functions, which are only a Fourier transform away. If $S^L_{2,i}(r)$ are the second order structure functions of probe i, the correction then becomes

$$\widetilde{\Delta u^T}(r_{ij}) = u_i \frac{\overline{S_2^L}(r_{ij})^{1/2}}{S^L_{2,i}(r_{ij})^{1/2}} - u_j \frac{\overline{S_2^L}(r_{ij})^{1/2}}{S^L_{2,j}(r_{ij})^{1/2}}, \tag{2.12}$$

where $\overline{S_2^L}$ is the averaged second order structure function. This results in a dramatic improvement of measured transverse structure functions as shown in Fig. 2.6. In the second order structure function $(S_2^T(r))^{1/2}$ the systematic noise has now been reduced from $0.1 ms^{-1}$ to $0.01 ms^{-1}$.

Although the basis of the correction Eq. 2.12 is the (approximate) isotropy of turbulent fluctuations, it does not make the structure functions trivially isotropic, neither does it change the overall scaling behaviour.

2.3.3 Long integration times

When the order p of the structure functions $S_p = \langle \Delta u^p \rangle$ is increasing, velocity fluctuations Δu increasingly larger than the r.m.s. value, $\langle \Delta u^2 \rangle^{1/2}$, will dominate the contributions $\langle \Delta u^p \rangle$. However, the larger the velocity increment is, the lower the probability of its occurrence. If we construct the PDFs of velocity increments $\mathcal{P}_r(\Delta u)$, taken at a separation r over a long time interval, then we observe that from a total number of samples collected ($N_t = 2 \cdot 10^8$) in an experiment, only about $N \sim 10^3$ have $\Delta u / \langle \Delta u^2 \rangle^{1/2} \geq 6$ (see Fig. 2.7(a)). Therefore, at a large enough order p, N will be too small to insure a statistically convergent value of

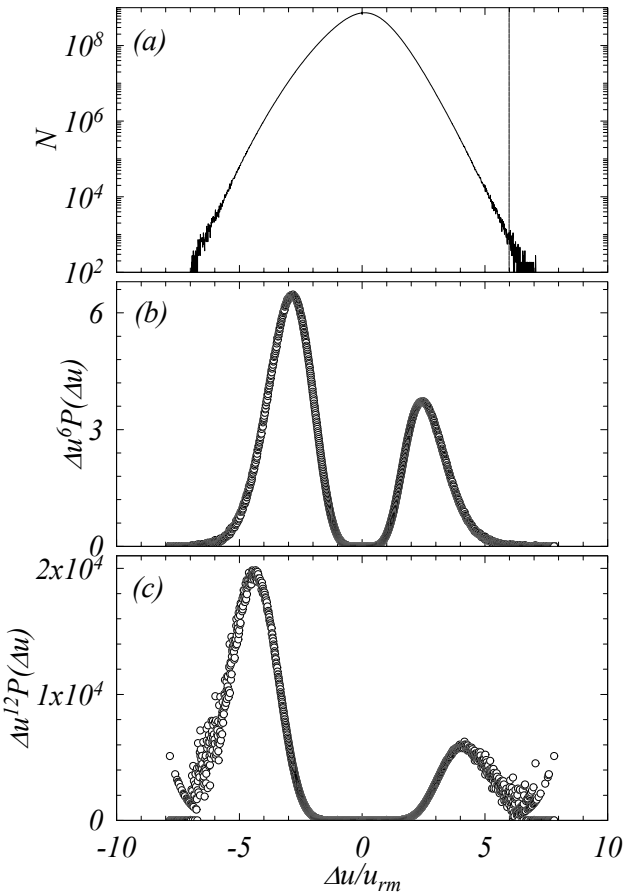

Fig. 2.7: *(a) Histogram of velocity increments taken over a longitudinal separation $r/\eta \sim 400$ in the inertial range, in turbulence with $Re_\lambda \sim 600$. The total number of collected samples was in this case $N_t = 2 \cdot 10^9$. Moments $p = 6$ (b) and $p = 12$ (c) of the probability density function $\mathcal{P}_r$ show that the number of collected samples N_t is sufficient to insure convergence of the structure functions of corresponding orders.*

the structure function S_p at the separation r. Alternately, the structure functions can be calculated directly from the PDFs as

$$S_p(r) = \langle \Delta u^p \rangle = \int_{-\infty}^{\infty} \Delta u^p \mathcal{P}_r(\Delta u)\ d(\Delta u). \tag{2.13}$$

When the order p grows, the low probability tails of $\mathcal{P}_r(\Delta u)$ will give most of the contribution to the value of $S_p(r)$. The exact correspondence between the order p of the structure function and the probability level that contributes significantly to it will be described in chapter 3. Insufficiently long experiments will therefore result in unconverged high-order structure functions, since the histograms will be depleted of large velocity increments. An efficient method of determining the highest order p structure function that is still converged, is to examine the moments of the probability density functions

$$M_p(\Delta u) = \Delta u^p \mathcal{P}_r(\Delta u), \tag{2.14}$$

We show the functions $M_p(\Delta u)$ for two orders, a moderate $p = 6$ and a large $p = 12$ in Fig. 2.7(b,c). When the tails of M_p

$$\lim_{\Delta u \to \pm\infty} M_p(\Delta u) \tag{2.15}$$

have smoothly decreased to 0, then the contribution from separation r to the structure function

$$S_p = \int_{-\infty}^{\infty} M_p d(\Delta u)$$

is statistically converged. If the values of M_p oscillate at large $|\Delta u|$, then a longer time-series is needed to resolve order p. We can see that this behaviour starts in our case at order $p \sim 12$.

Therefore, an accurate determination of high-order structure functions needs very long integration times. It is important that these integration times involve many uncorrelated events, that is, contain many large-eddy turnover times. Since in experiments the velocity field is sampled so sparsely, collecting many velocity samples automatically involves many turnover times. In numerical simulations, the situation is opposite: each snapshot of the computed velocity field contains millions of points, but the integration time is only a few turnover times. Therefore, the total number of collected velocity samples is not a good criterion for assessing the accuracy of high-order structure functions. In our experiments, each run lasted many (up to 6) hours, during which the velocity field was sampled at approximately the Kolmogorov frequency.

Chapter 3

STRONG EVENTS AND INTERMITTENCY

3.1 Introduction

Experimental work in turbulence pointed out the existence of violent rare events, commonly referred to as *worms*. They are believed to be filamentary vortical objects containing a large vorticity concentration within a scale of the order of the dissipation scale. Consequently, the velocity difference across such objects would be an important fraction of the mean velocity of the flow.

Visual evidence of worms first came from numerical simulations by She *et al.* [79] and bubble visualization techniques by Douady *et al.* [26], which revealed their vortex filament structure. This step was followed by sustained efforts to quantify their properties in the work of Siggia [83] and Jimenez *et al.* [46], from investigations of low Reynolds number numerical simulations.

The key question of this chapter is to find these strong vortical events in experiments on fully developed turbulent flow with a large Reynolds number. To this aim we will exploit the velocity information measured by an array of hot-wire probes in a windtunnel. A problem is to define detection schemes that can identify these strong events with a vortical signature. This chapter describes a concentrated effort to find them reliably.

Next, the question will be in what manner these events contribute to intermittency and anomalous scaling. Loosely, intermittency is characterized by the preference of turbulence for large velocity gradients, which is reflected in strongly non-Gaussian tails of the probability density functions of velocity differences. While it is obvious that these tails are determined by extreme events, a question is their relation with anomalous scaling.

3.2 Longitudinal and transverse scaling

In the past few years it has become clear that different geometrical arrangements of turbulence detection may discriminate between different types of turbulent structures. In fact, the measured statistical properties, including even general

aspects such as scaling exponents, may depend on the geometrical arrangement. A detailed analysis of this effect in terms of elements of the rotation group will be presented in chapter 4, but here it suffices to make a simple distinction between the longitudinal and transverse arrangements.

In statistical turbulence, we are interested in velocity increments $\Delta \boldsymbol{u}(\boldsymbol{r}) = \boldsymbol{u}(\boldsymbol{x}+\boldsymbol{r}) - \boldsymbol{u}(\boldsymbol{x})$ measured over a distance r, loosely the strength of eddies with size r. If the measured velocity component points in the same direction as the vector $\boldsymbol{r}$, then we obtain a longitudinal velocity increment, and if $\boldsymbol{r}$ points perpendicular to it, then we measure transverse velocity increments. Accordingly, a similar distinction can be made between the structure functions of order p, such that $G_p^L(r) = \langle \Delta u_L^p(r) \rangle$ and $G_p^T(r) = \langle \Delta u_T^p(r) \rangle$ are longitudinal, respectively transverse structure functions.

A few years ago it was realized that the longitudinal structure function may have a different algebraic behavior than the transverse one, $G_p^L(r) \sim r^{\zeta_p^L}$, $G_p^T(r) \sim r^{\zeta_p^T}$, with $\zeta_p^L \neq \zeta_p^T$. This was first observed by van de Water et al. [92] and attributed to the large scale anisotropic structure of the flow, and then confirmed by experiments (Dhruva *et al.* [24]) and numerical simulations (Chen *et al.* [18]).

Scaling behavior of structure functions is an inertial range property and occurs at r values (much) larger than the dissipative length-scale, but smaller than the external length-scale. A simple dimensional argument links the structure function to the energy dissipation rate rate ϵ_r averaged over scales r

$$\epsilon_r(\boldsymbol{r}, t) = \frac{1}{V_r} \int_{B_r} \epsilon \, d\boldsymbol{r}, \tag{3.1}$$

where B_r is a sphere of radius r centered at $\boldsymbol{r}$ and ϵ is the local dissipation

$$\epsilon = \frac{\nu}{2} \sum_{i,j=1}^{3} \left(\frac{\partial u_i}{\partial x_j} + \frac{\partial u_j}{\partial x_i} \right)^2 . \tag{3.2}$$

To be specific, whilst the *longitudinal* structure function can be associated with the local dissipation ϵ, the *transverse* structure function is associated with the local enstrophy ω^2. This is because in isotropic turbulence the dissipation can be expressed in the longitudinal derivative only $\epsilon = 15\nu\langle(\partial u/\partial x)^2\rangle$, whilst the transverse derivatives are determining the vorticity $\boldsymbol{\omega}$.

The circumstance that scaling exponents are different from their self-similar values $p/3$ implies that the local dissipation rate ϵ fluctuates, such that the locally averaged mean dissipation

$$\langle \epsilon_r^p \rangle \sim r^{\tau_p}, \tag{3.3}$$

where the scaling exponents τ_p and $\zeta_p = p/3 + \tau_p$ are related through Kolmogorov's refined similarity hypotheses ([49]).

To account for the different scaling of the longitudinal and transverse structure functions, it was recently shown by Chen *et al.* [18] that the local enstrophy follows different scaling rules

$$\langle \Omega_r^p \rangle \sim r^{\xi_p}, \tag{3.4}$$

with $\xi_p < \tau_p$ of Eq. 3.3. As a consequence, an alternative refined similarity hypothesis was proposed (Chen *et al.* [19]), separating the scaling of transverse structure functions

$$\langle \Delta u^p(y) \rangle \sim (\langle \Omega_r \rangle y)^{p/3} \tag{3.5}$$

from the scaling of longitudinal structure functions

$$\langle \Delta u^p(x) \rangle \sim (\langle \epsilon_r \rangle x)^{p/3}, \tag{3.6}$$

such that the total transverse scaling exponents are smaller. These arguments favor the idea that the transverse velocity increments are more connected to intermittent structures that the longitudinal ones. However, in a paper by He *et al.* [44] it was pointed out that no thinkable vortical structure would support different scaling of dissipation and enstrophy.

Another explanation for the different scaling of the longitudinal and transverse exponents may be that the transverse arrangement is more effective in capturing vortical events (Noullez *et al.* [61]).

These two ideas prompted us to develop methods for extracting vortical events from the time-series of turbulence measurements. While structure functions are well-defined quantities in the statistical analysis of turbulence, the extraction of structures is a wide-open problem. There is an urgent need for more sophisticated ways of extracting statistical information from turbulence data. After all, the traditional statistical quantities are based on two-point measurements of the velocity field, whereas nowadays much more information is available, in numerical simulations but also in experiments. In this chapter, we will move from the quantification of intermittency by means of structure functions, to measuring structures.

In section 3.3, the experimental setup is described, and then basic properties of the turbulent flow, such as isotropy and homogeneity, are evaluated. Next, we measure the scaling behaviour of the structure functions and compare it to what was found by others. We confirm that the scaling anomaly is larger in the transverse direction, especially so at large orders p.

We continue with an extensive discussion on how to find strong (vortical) events in an experimental signal. A naive strategy would be to just look for large velocity increments. For this we would only need the probability density functions of velocity increments. Their shape and contribution of their extreme

velocity increments tails to high-order structure functions are discussed in section 3.5. This discussion provides a reference point for more sophisticated techniques to extract worms.

After reviewing previous methods for extracting worms from numerically simulated turbulent fields, we propose in section 3.6 a simple algorithm that can be applied to experimental time-series of velocity fields measured in discrete points along a line. The purpose of this conditional algorithm is to find large vortical events together with their atmospheres. As all conditional algorithms suffer from the problem that their result may be determined by the imposed condition rather than by genuine structures, we first test it on a synthetic turbulence signal. A second null-test will be performed in the context of the experiment.

A synthetic turbulent velocity field is constructed in section 3.6.2 by a random collection of Burgers vortices. We will then investigate wether our algorithm indeed identifies these vortices from a simulated measurement. As expected, it approximately does so in the transverse direction.

Next, we apply our algorithm to an experimental signal. Perhaps surprisingly, we obtain vortex signatures which resemble Burgers vortices with a size that is a few times the dissipative length scale. In a null test, we randomize the experimental signal, in a way that leaves its second-order statistical properties invariant: a signal with the same turbulence properties, which lacks all turbulent structures. Also this test prefers the transverse arrangement.

Finally, in section 3.7, we assess the importance of worms to inertial range intermittency. This is done by analyzing the contribution of worms to the anomalous scaling of structure functions. To this aim, transverse worms are removed from the velocity time-series and the structure functions are recomputed.

3.3 Experimental setup

Before we start the actual quest for finding the worms, a suitable experiment has to be devised. The purpose is to create strong turbulence that has a large Reynolds number and exhibits clear scaling. To this aim a special grid is used to stir the flow, which is described in detail in [2]. In the present measurements we work at the highest Reynolds number $Re_\lambda \sim 900$ that could be obtained in our windtunnel. Other studies with varying Re_λ will be discussed in chapters 6 and 7. The grid is placed at the beginning of the test section of a recirculating windtunnel, with a length of $8m$ and $0.9 \times 0.7m^2$ cross-section. The choice of the Cartesian coordinate system is that the x-direction is that of the measured velocity component u. The distribution of velocity fields u will be measured in the (transverse) y-direction. From the sketch of the experimental setup, shown in Fig. 3.1, we can see that the geometry of the grid is less filling in the spanwise z-

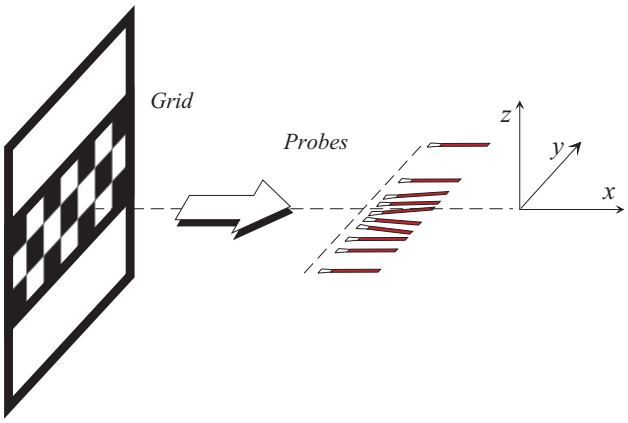

Fig. 3.1: *Sketch of the experimental setup and the reference frame used. The separation between the grid and the hot-wire array is approximately* $x/L = 5.1$*, where* $L = 0.88m$ *is the height of the windtunnel.*

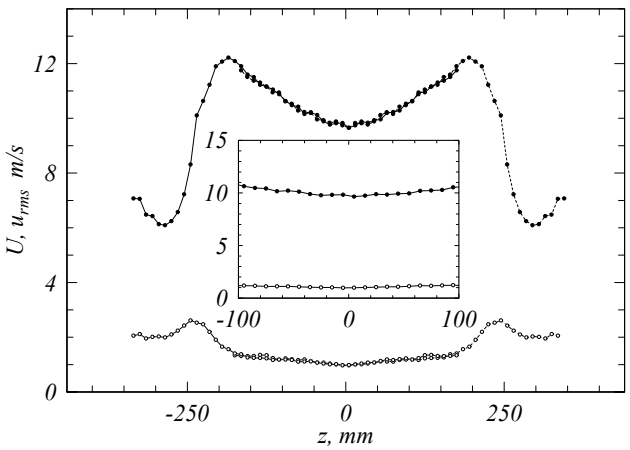

Fig. 3.2: *Mean and r.m.s velocity profiles in the* z*-direction, at* $(x, y) = (0, 0)$*. The choice of the coordinate system is indicated in Fig. 3.1, such that its origin is taken in the center of the spanwise plane at a separation of 4.5m downstream from the grid. A small region of the flow (*$z \geq 200$*) was not tested, but predicted from mirroring the profiles around the* $z = 0$ *point (dashed lines). The inset shows details of the central region of the flow, which is approximately homogeneous over a length comparable to the width of the sensor array.*

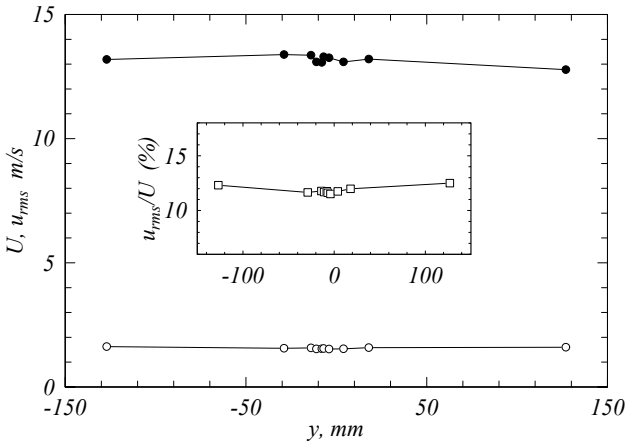

Fig. 3.3: *Mean and r.m.s velocity profiles in the y-direction, at* $(x, z) = (0, 0)$. *They were measured using the array of hot-wire sensors.*

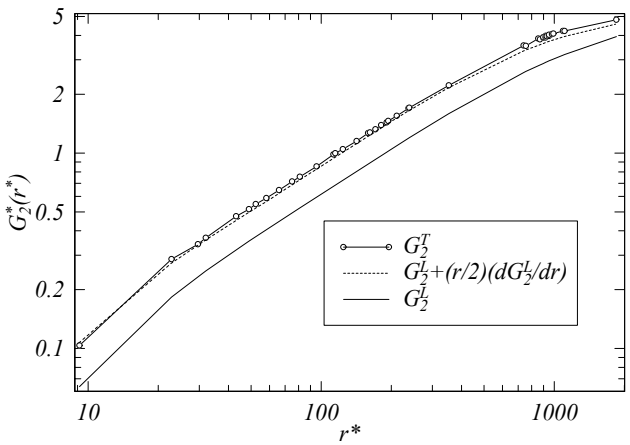

Fig. 3.4: *Second order transverse (∘) and longitudinal (full line) structure functions measured at* $Re_\lambda \sim 840$. *The longitudinal structure function is used to estimate what the transverse structure function would be in a truly isotropic turbulent flow (see Eq. 3.7). The computed transverse structure function (dashed line) and the measured one are almost identical. All quantities are normalized on dissipative scales:* $r^* = r/\eta$, $G_2^* = G_2/v_K^2$, *with the Kolmogorov velocity* $v_K = \nu/\eta$.

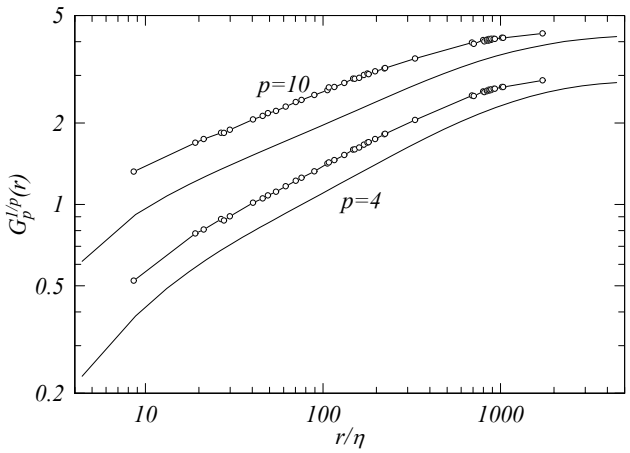

Fig. 3.5: *Transverse (open markers) and longitudinal (solid lines) structure functions of orders $p = 4$ and $p = 10$.*

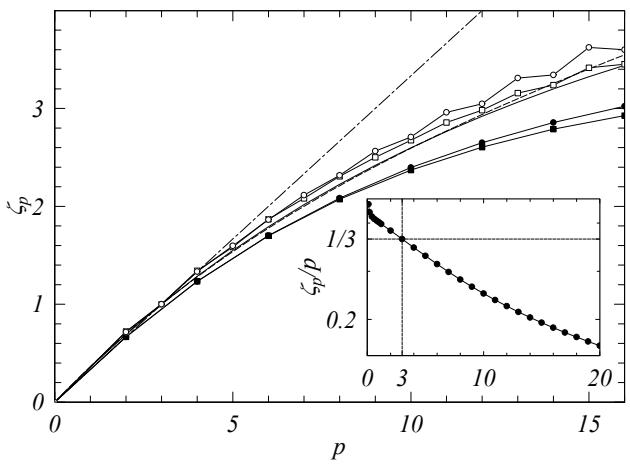

Fig. 3.6: *Scaling exponents measured at $Re_\lambda \sim 840$ (circles) and $Re_\lambda \sim 860$ (squares) deviate strongly from the Kolmogorov prediction (dash-dotted line). The longitudinal exponents (empty symbols) follow closely the She-Leveque model (dashed lines), while the transverse (full symbols) show higher intermittency. Also shown are the longitudinal exponents determined from structure functions of absolute values of velocity increments (solid line). The inset shows an alternative way of plotting the transverse scaling exponents which emphasizes the anomalous scaling, also present at small orders $0 \leq p \leq 1$.*

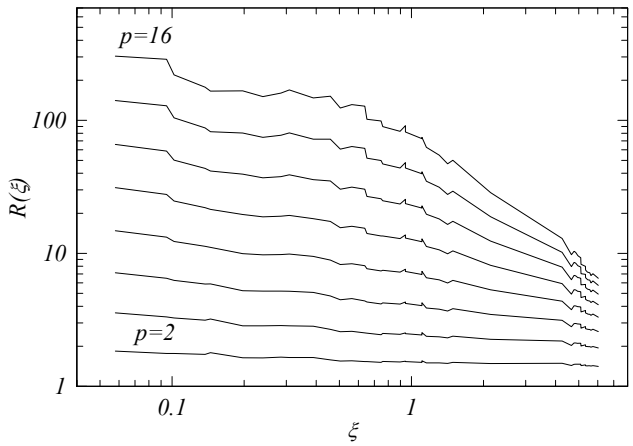

Fig. 3.7: *The different longitudinal and transverse scaling anomaly is better exposed when structure functions are plotted against each other and relative scaling exponents are extracted ([10]). Here we show the ratio of the $G_p^{L,T}$ plotted as functions of $\xi = G_3^L$, $R_p(\xi) = \tilde{G}_p^T(\xi)/\tilde{G}_p^L(\xi)$. If $\zeta_p^{T,L}$ are the scaling exponents of the original structure functions, then $R_p(\xi) \sim \xi^{\tilde{\zeta}_p^T - \tilde{\zeta}_p^L}$, with $\tilde{\zeta}_p^T = \zeta_p^T/\zeta_3^L$ and $\tilde{\zeta}_p^L = \zeta_p^L/\zeta_3^L$.*

direction, therefore one is concerned about the homogeneity of the downstream turbulent flow in both y and z directions. This arrangement generates a maximum Reynolds number $Re_\lambda \cong 860$ in our windtunnel, which we measure about $4.5m$ downstream from the grid, on the centerline of the tunnel.

The velocity fields are captured by an array of 10 hot-wire sensors, oriented orthogonally to the direction of the mean flow. The hot-wires with thickness of $2.5\mu m$ have a sensitive length of $200\mu m$, which is slightly larger than the Kolmogorov length is these experiments $\eta = 1.4 \cdot 10^{-4} m$. In a turbulent flow with a large mean flow component in the x-direction, they are mainly sensitive to the u-component of the fluctuating velocity field. The use of an array gives access to the transverse $u(y)$-distribution. The velocity can also be evaluated at different positions in the x-direction aligned with the mean velocity U, by making use of the Taylor frozen turbulence hypothesis. This converts time-delays from fixed probes in longitudinal separations and is valid when the intensity of the turbulence fluctuations is a small fraction of the mean velocity U, $u/U \ll 1$. An extensive discussion of the Taylor hypothesis will be presented in chapter 7.

Simple statistics of the velocity field show that the y-averaged turbulent intensity at the measurement position is $\sim 12\%$, at a mean velocity slighty larger than $13m/s$. This might be considered too large to ensure a safe use of the Taylor hypothesis, but in our study we will mostly use the physical transverse separations

$U\ (ms^{-1})$	$\langle u^2\rangle^{1/2}(ms^{-1})$	$\lambda\ (m)$	$\langle\epsilon\rangle\ (m^2s^{-3})$	$\eta\ (m)$	Re_λ
13.17	1.56	$8.29\cdot10^{-3}$	7.97	$1.43\cdot10^{-4}$	862.9

Tab. 3.1: *Flow characteristics: U is the mean velocity, u the r.m.s. velocity, λ the Taylor microscale, ϵ the mean dissipation, η the Kolmogorov scale and Re_λ is the Taylor-microscale Reynolds number. In isotropic and homogeneous turbulence, only one component of the velocity derivative is needed to evaluate the mean dissipation $\langle\epsilon\rangle = 15\nu\langle(\partial u/\partial x)^2\rangle$.*

between probes, rather than time delays.

The multiscale grid (Fig. 3.1) that is used produces a strongly turbulent wake whose center is approximately homogeneous. We show in Fig. 3.2 the mean and r.m.s longitudinal velocity profiles in the z-direction, extracted in a separate experiment with a single probe, taken at $y = 0$. This position is situated halfway between the vertical walls of the windtunnel. The Reynolds number of this separate test was slightly smaller than the maximal value, such that at the location $z = 0$ the mean velocity was $U \sim 10m/s$. From the appearance of the curve we can see that, except for a relatively homogeneous region of length $\Delta z_0 \leq 20cm$, the flow exhibits a strong shear in the z-direction. The symmetric peaks in the mean velocity curve show the empty regions where the flow is no longer obstructed. The strong enhancement of the turbulent intensity in the shear regions can also be observed. Our turbulence measurements were always done in the (homogeneous) y-direction, which had negligible variations of U and u over the length of the probe array, as can be seen in Fig. 3.3.

The characteristics of the turbulent flow are listed in table 3.1. The anisotropy of the flow can be quantified through the relation between the second order longitudinal and transverse structure functions, which holds in isotropic turbulence

$$G_2^T(r) = G_2^L(r) + \frac{r}{2}\frac{dG_2^L}{dr} \tag{3.7}$$

From the measured longitudinal structure function, a transverse $\tilde{G}_2^T(r)$ was calculated from the r.h.s. of Eq. 3.7. In Fig. 3.4 we plot this together with the actually measured G_2^T. The results, for a flow with $Re_\lambda = 840$, show that G_2^T is very close to $\tilde{G}_2^T(r)$. This is only a partial isotropy check which is flattered by the circumstance that in our arrangement $G_2^T(r\to\infty) = G_2^L(r\to\infty) = 2\langle u^2\rangle$.

3.4 Anomalous scaling exponents

A measurement of scaling exponents starts with recording a long time-series of turbulent velocities. From those, histograms of both longitudinal $\Delta u_L(r)$ and transverse $\Delta u_T(r)$ velocity increments are built. The transverse separations r are true spatial separations (the distances between probes), and the longitudinal separations are made from time-delays $r = U\tau$ through Taylor's frozen turbulence hypothesis.

The histograms are, up to a normalization factor, the same as the probability density functions (PDFs) from which the structure functions follow as

$$G_p^T(r) = \langle \Delta u_T(r)^p \rangle = \int_{-\infty}^{\infty} \mathcal{P}_r(\Delta u_T) \Delta u_T^p d(\Delta u_T), \tag{3.8}$$

and analogously for the longitudinal increments. Since measured velocities are discrete, computing the moments through the discrete histograms is done without loss of accuracy.

The low-probability tails of the PDFs can be represented accurately through stretched exponentials

$$\mathcal{P}_r(\Delta u) = a e^{-\alpha |\Delta u|^\beta}, \tag{3.9}$$

with constants a, α and β that in general depend on the separation r and the sign of Δu. A full account of this stretched exponential approximation will be given in section 3.5. A significant improvement in the measured structure functions can be obtained by computing the contribution of the low-probability tails through integration over the stretched exponentials, rather than directly summing over the measured histograms.

Several measured structure functions are shown in Fig. 3.5. Clearly, it is possible to assign a scaling exponent to each of the curves. Since we plot the structure functions as $G_p^{1/p}$, they would have the same slope $1/3$ in a log-log plot. Instead we see that the slopes ζ_p/p *decrease* with increasing order: the scaling exponents are anomalous.

The scaling exponents as a function of the order p are shown in Fig. 3.6. Since the transverse PDF is reflection symmetric $\mathcal{P}_r(\Delta u_T) = \mathcal{P}_r(-\Delta u_T)$, we will use absolute values $|\Delta u_T|$. Several observations can be made from this figure. First, both ζ_p^T and ζ_p^L are strongly anomalous, *i.e.* very different from the K41 self-similar prediction. This defies suggestions in the literature ([40]) that scaling anomaly is a finite size effect that would either disappear at infinite Reynolds number or an infinite number of velocity samples. Second, scaling anomaly is not only a property of the large orders p (where large velocity increments are emphasized), but also of the low orders. Third, the longitudinal scaling exponents ζ_p^L are represented well by the log-Poisson model of She and Leveque [80].

Finally, the transverse exponents appear to be more anomalous than the longitudinal ones $\zeta_p^T < \zeta_p^L$. The difference is small, but significant as we will argue below.

In order to demonstrate the significance of the difference between the longitudinal and transverse exponents, we introduce the notion of *relative scaling* (Benzi et al. [10]). The idea is to plot structure functions $G_p(r)$ as functions of another structure function, say $G_3(r)$, on a log-log plot. In this way, *some* non-universal behavior will drop out (van de Water et al. [91]) which results in an improved scaling and less ambiguous scaling exponents. The method is often referred to as *extended self-similarity* (ESS [10]). Here we will use the same procedure and plot both G_p^L and G_p^T as a function of $\xi = G_3^L$. Let's call these relative functions $\tilde{G}_p^L(\xi)$, $\tilde{G}_p^T(\xi)$. If $G_p^{L,T}(r)$ have scaling behavior, so will $\tilde{G}_p^L(\xi) \sim \xi^{\tilde{\zeta}_p^L}$ and $\tilde{G}_p^T(\xi) \sim \xi^{\tilde{\zeta}_p^T}$, with $\tilde{\zeta}_p^L = \zeta_p^L/\zeta_3^L$ and $\tilde{\zeta}_p^T = \zeta_p^T/\zeta_3^L$, respectively. If $\zeta_p^T < \zeta_p^L$, so will $\tilde{\zeta}_p^T < \tilde{\zeta}_p^L$. Conversely, the ratio

$$R_p(\xi) = \frac{\tilde{G}_p^T(\xi)}{\tilde{G}_p^L(\xi)} \tag{3.10}$$

will be a decreasing function of its argument ξ, and will itself be an algebraic function with exponent $\tilde{\zeta}_p^T - \tilde{\zeta}_p^L$. These ratios are plotted in Fig. 3.7, where we computed the structure functions using absolute values $|\Delta u_{L,T}|$. The use of absolute value velocity increments has been recognized Grossmann et al. [41] as essential for the ESS method to work. It is seen that for $p > 3$, $R_p(\xi)$ is indeed a decreasing function of ξ, but the assignment of a scaling exponent to large moments is problematic. However, we must remember that this scaling exponent is only the small *difference* between transverse and longitudinal exponents. On basis of Fig. 3.7, we believe that this difference is significant.

At this point we would like to remark that differing ζ_p^L and ζ_p^T may not be the only way that scaling of structure functions may be geometry dependent. In chapter 4, we will exploit a description based on angular momentum theory in which structure functions embody a *sum* of algebraic behaviors.

3.5 Asymptotic behavior of probability distribution functions

Strong vortical events in which we are interested come with large velocity increments. However, large increments *per se* do not necessarily point to coherent structures. Still, it is interesting to study the influence of large velocity increments on high-order structure functions. Such a study provides a reference point for attempts later in this chapter to educe these structures from our signals. The

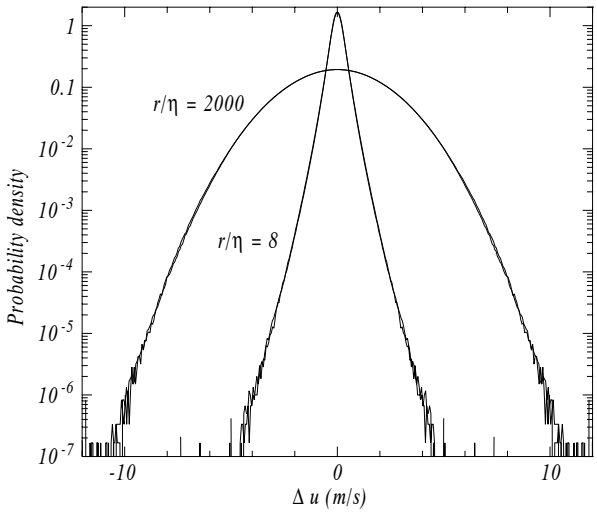

Fig. 3.8: *Probability density function of transverse velocity increments $\Delta^T u(r)$ at $r/\eta = 8$ and $r/\eta = 2000$. To demonstrate the symmetry of the measured transverse PDFs, $\mathcal{P}(x)$ and $\mathcal{P}(-x)$ are shown overlayed. The PDFs can be represented well by stretched exponentials $\mathcal{P}(x) = a\exp(-\alpha|x|^\beta)$, with, apparently, $\beta < 1$ for the smallest separation and $\beta \approx 2$ for the largest separation.*

occurrence of velocity increments Δu is captured by their PDFs $\mathcal{P}(\Delta u)$, and the present discussion can be done entirely through these PDFs.

The probability density functions $\mathcal{P}(\Delta u)$ of velocity increments are experimentally constructed from long time-series of recorded velocity signals. Their tails contain large velocity increments that have a low probability of occurrence. They may be considered as contributions from vortical structures. Using the stretched exponential parametrization of $\mathcal{P}(\Delta u)$, we will give in this section estimates of the importance of large velocity increments to high order structure functions.

In van de Water & Herweijer [93] it was shown that PDFs can be represented well using stretched exponentials. This conclusion was reached after a careful analysis of the statistical fluctuations of measured PDFs. Experimentally, probability density functions are determined by collecting measured velocity differences in discrete bins. The fluctuation of the contents of these bins was found to be near-Poissonian. It allowed to devise a χ^2 test of the goodness of fit of stretched exponentials

$$\mathcal{P}(\Delta u) = a\mathrm{e}^{-\alpha|\Delta u|^\beta}, \tag{3.11}$$

with the stretching exponent β ranging from values $\beta < 1$ in the dissipation range

to $\beta = 2$ at large scales, where Δu is made of uncorrelated velocity readings and the PDF becomes a Gaussian. The parameters a, α and β are different for the left ($\Delta u < 0$) and right ($\Delta u > 0$) tails of the PDF. In our fits, χ^2 rarely exceeds 1.5. Values larger than 1 may signify the presence of finite correlations between Δu samples in adjacent bins.

First we will discuss the consistency of the stretched exponential description. As this description facilitates observations based on experimental PDFs, we will next use this parametrization to resolve questions about the number of samples that significantly contribute to high-order moments, and the influence of the truncation of the tails of the PDFs on these moments.

The stretched exponential approximation works for both longitudinal and transverse velocity increments, but it appears to work best for the transverse case. Therefore, we will restrict the discussion to the transverse increments in homogeneous turbulence.

Stretched exponentials may be a practical way to represent the tails of PDFs, but they violate the simple constraint that the chances of finding a large velocity *difference* Δu of size, say, x, must always be smaller than finding a *velocity* u with size x. In other words, the PDF of the velocity increment $\Delta u = u_1 - u_2$ at $r \ll L$ can never intersect the one at the integral scale L where u_1 and u_2 are uncorrelated. With β ranging from $\beta < 1$ at dissipative scales to $\beta = 2$ at integral scales, these intersections are inevitable, and the stretched exponential description must break down. However, the probability level where such intersections would occur are prohibitively small. That is, the number of velocity samples needed to observe this breakdown is astronomically large.

More precisely, this argument can be phrased as in Noullez et al. [61]. The point made there is that the probability to find a velocity increment Δu larger than a certain value x, $\mathrm{Prob}\{|\Delta u| > x\}$, requires that at least one of u_1, u_2 in $\Delta u = u_1 - u_2$ must in absolute value be larger than $x/2$, so that

$$\mathrm{Prob}\{|\Delta u| > x\} \leq \mathrm{Prob}\{|u_1| > x/2 \ \text{ or } \ |u_2| > x/2\}. \tag{3.12}$$

In case that u_1 and u_2 are independent (at large separations), this condition can be written as

$$\begin{aligned} \mathrm{Prob}\{|\Delta u| > x\} &\leq 2\mathrm{Prob}\{|u| > x/2\} \\ \int_{|\xi|>x} \mathcal{P}^d(\xi)\,\mathrm{d}\xi &\leq \int_{|\xi|>x/2} \mathcal{P}^s(\xi)\,\mathrm{d}\xi, \end{aligned} \tag{3.13}$$

where $\mathcal{P}^d$ en $\mathcal{P}^s$ are the PDFs of the velocity difference and the velocity, respectively. We may express $\mathcal{P}^s(\xi)$ in terms of the velocity increment PDF $\mathcal{P}^d_{r=\infty}(\xi)$ at large separations where both are Gaussian,

$$\mathcal{P}^d_{r=\infty}(\xi) = \int \mathcal{P}^s(x+\xi)\mathcal{P}^s(x)\,\mathrm{d}x,$$

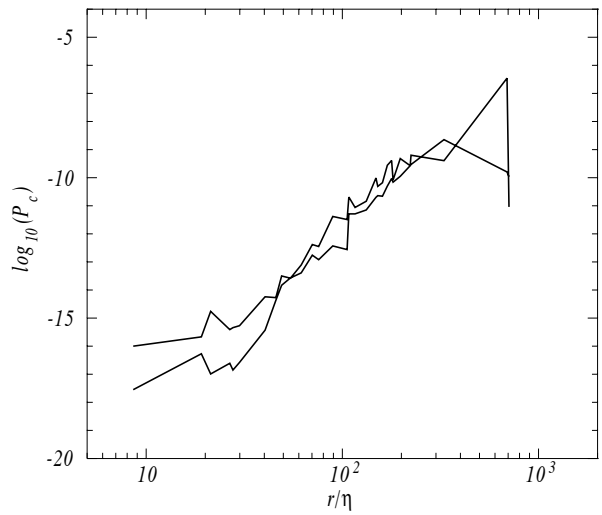

Fig. 3.9: *Probability where the velocity increment at separation r will cross the one at L with $L/\eta = 2 \times 10^3$. The two lines are for the left and right tails of the PDF.*

with the result $\mathcal{P}^d_{r=\infty}(\xi) = \mathcal{P}^s(2^{-1/2}\xi)$, so that the no-crossing condition becomes

$$\int_{|\xi|>x} \mathcal{P}^d(\xi)\,\mathrm{d}\xi \;\le\; 2\int_{|\xi|>2^{-1/2}x} \mathcal{P}^d_{r=\infty}(\xi)\,\mathrm{d}\xi \tag{3.14}$$

Instead of the precise non-crossing rule Eq.(3.14), we show in Fig. 3.9 the r-dependent probabilities for intersections of the positive and negative PDF tails

$$\mathcal{P}^+_c = \int_{\Delta u_s}^{\infty} \mathcal{P}_r(x)\,\mathrm{d}x\,, \mathcal{P}^-_c = \int_{-\infty}^{-\Delta u_s} \mathcal{P}_r(x)\,\mathrm{d}x$$

where Δu_s is the velocity increment where $\mathcal{P}_r$ and $\mathcal{P}_L$ intersect, $\mathcal{P}^{\pm}_r(\Delta u_s) = \mathcal{P}^{\pm}_L(\Delta u_s)$, with $L/\eta = 2 \times 10^3$. The probability was computed from stretched exponential fits; the noise in the curves is due to the uncertainty in the fitted parameters that determine the intersections.

We conclude that at small scales, the stretched exponential description becomes only untenable at integration times which are practically unreachable. Therefore, a stretched exponential description of the tails of the PDF remains a sound procedure, although it is strictly inconsistent.

Using the stretched exponential parametrization of the PDF it is straightforward to answer questions about the asymptotic properties of large events. For example, what is the probability $\mathcal{P}_p$ of the velocity increments $|\Delta u| > |\Delta u_m|$ that significantly contribute to the order p moment ? We take the answer to be

$$\mathcal{P}_p = \mathcal{P}^-_p + \mathcal{P}^+_p = \int_{-\infty}^{\Delta u^-_m} \mathcal{P}_r(x)\,\mathrm{d}x + \int_{\Delta u^+_m}^{\infty} \mathcal{P}_r(x)\,\mathrm{d}x, \tag{3.15}$$

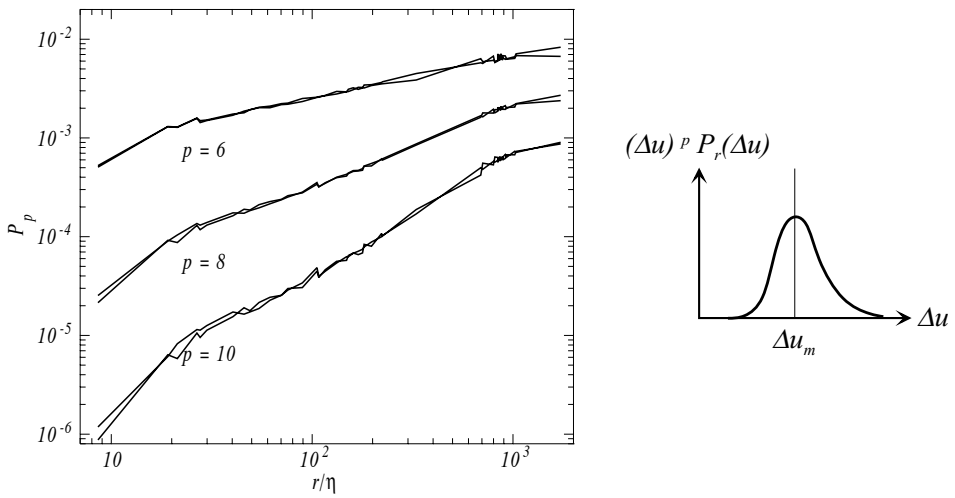

Fig. 3.10: *Probability $\mathcal{P}_p^{\pm}$ of velocity increments that contribute significantly to moments of order p.*

where $\Delta u_m^{\pm}$ are the velocity increments where $(\Delta u)^p \mathcal{P}_r(\Delta u)$ has a local maximum. Of course, this answer ignores the increments smaller than $|\Delta u_m^{\pm}|$ that also contribute to the moment, but we believe that Eq. (3.15) should be correct to within a factor 2.

The probabilities $\mathcal{P}_p^{\pm}$ are shown for various orders p in Fig. 3.10. They are rapidly increasing with the separation r, which signifies that the accuracy of the moments at the smallest separations is most problematic. An analogous conclusion was reached in [93], but in a completely different way. The stretched exponentials underlying Fig. 3.10 were determined from $N = 10^8$ velocity samples. At the smallest resolved distances, a mere $\mathcal{P}_p(r/\eta = 8)N = 2 \times 10^{-6}N = 200$ events contribute most significantly to the $p = 10$ moment.

The converse question is how a moment p is affected when the tails of the PDF are truncated at $-\Delta u_t$ and Δu_t, with the truncated moment $G_t = \int_{-\Delta u_t}^{\Delta u_t} x^p \mathcal{P}_r(x)\,\mathrm{d}x$. Roughly, the truncated events would have been missed at a total number of samples N given by $N \cdot \mathcal{P}_t = 1$, with $\mathcal{P}_t = 1 - \int_{-\Delta u_t}^{\Delta u_t} \mathcal{P}_r(x)\,\mathrm{d}x$.

These moments are shown in Fig. 3.11 for the untruncated case ($\mathcal{P}_t = 0$) and $\mathcal{P}_t$ ranging from 10^{-8} to 10^{-5}. All structure functions have scaling behavior. Their apparent scaling exponent increases when $\mathcal{P}_t$ increases. Thus, truncating the PDF leads to a reduction of the scaling anomaly. In the quest for structures that cause intermittency and induce anomalous values of the scaling exponents, strong vortical events (worms) have been associated with the velocity increments from the tails of the PDF (Belin et al. [9]). Here we conclude that the effect of truncation is more or less trivial. The question that will be addressed in the

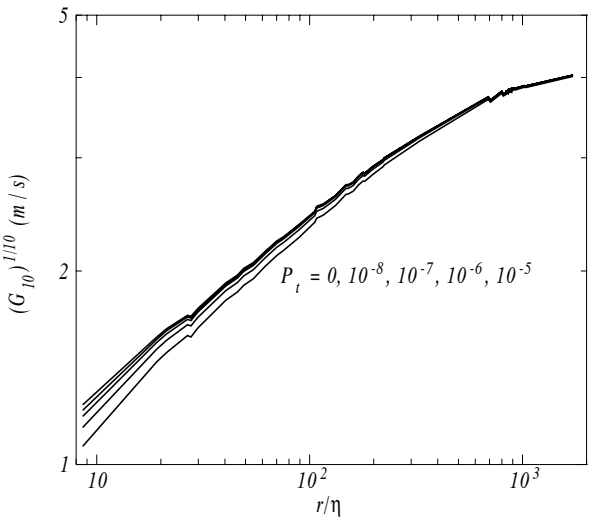

Fig. 3.11: *Structure function of order 10 computed over truncated PDFs. The total probability in the discarded tails is $\mathcal{P}_t$. $\mathcal{P}_t$ ranges from 0 (topmost curve) to 10^{-5} (lowest curve).*

following sections is how this picture changes if we seek for structures rather than just large velocity increments.

3.6 Conditional averaging

3.6.1 Introduction

The eduction of structures from either a numerical or experimental turbulent velocity field generally involves the following steps:

1. Devise a detection algorithm for small-scale vortical events. This proves to be the crucial part of the procedure, since its influence on the results is largest.

2. Select a threshold (criterion) on which the worms can be distinguished from "ordinary" or background field fluctuations.

3. Average the worm candidates in order to extract mean structure information. This step can sometimes be replaced or associated with statistical studies of distributions of worm characteristics, such as amplitude (or circulation), radius, shape, etc.

4. Evaluate the contribution of worms to anomalous scaling. This can be done by assessing changes of the scaling properties after surgically remov-

ing the worms from the velocity fields, or computing structure functions of the worms themselves.

Direct numerical simulations of homogeneous and isotropic turbulence offer the entire velocity field information and therefore permit less ambiguous detection algorithms for identification of worms. However, the relative lack of separation between the forcing and dissipative scales makes it difficult to observe an inertial range and recover the well-established scaling properties of fully developed turbulence. Therefore, the conclusions reached through direct numerical simulations still leave open the question: what will happen in strong turbulence that has a clear inertial range?

In the case of numerical turbulence (Jiménez *et al.* [46]), the typical detection method consists of selecting from snapshots of the vorticity field $\boldsymbol{\omega}(\boldsymbol{r})$ the points which exceed a certain threshold value $|\boldsymbol{\omega}(\boldsymbol{r})| \geq \omega_0$. These points are isolated from the rest of the flow by iso-vorticity surfaces that bound regions of strong vorticity. These regions come in the form of blobs and sheets which may be associated with worms. An additional requirement may be that these regions occupy a small fraction of space. Accordingly, [46] divide the entire vorticity field in three regions: a *weak* part, with ω smaller than the r.m.s. level ω', a *worm* part, with ω above a threshold covering 1% of the total volume, and a *background* part with the vorticity above ω' but smaller than the threshold fixed by volume constraints. This method was extended further to define a rotation axis within the elongated regions, and therefore enabled calculation of statistical quantities, such as distributions of the worm radii.

In the case of turbulence experiments, much larger Reynolds numbers are possible, but worm detection algorithms have to be adapted to the typical one-point hot-wire measurement of one or, at most, two velocity components. For example, if a threshold technique is employed, one has to replace vorticity amplitude ω_0 with a minimal value of the velocity derivatives. Because the velocity field information is limited, not only the time evolution of individual structures is out of the question, but it is also unclear if the high velocity increments selected from the hot-wire response are truly the signatures of a well-defined flow structures with spatio-temporal extension. Additional conditions on the velocity signal are required to narrow down the quest for vortical structures. In the case of a single probe configuration, the instantaneous velocity difference between two moments separated by a time delay τ is compared to the chosen threshold $|u_{min}|$. The situation is sketched in Fig. 3.12. All events larger than this value, typically chosen to be $|u_{min}| = 3u_{rms}$, are collected as worms, together with their "past" and "future" over a time-scale comparable to the largest eddy turnover time (see Fig. 3.12(a)). The final step is to align the events on the position of the large velocity excursion and then average them. After averaging, a structure such as

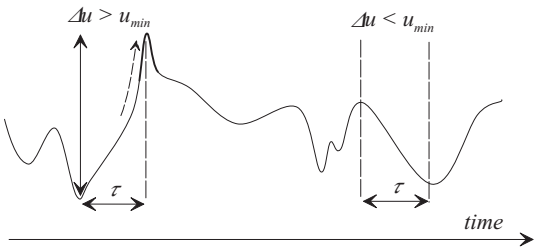

(a) Compare velocity differences with u_{min}

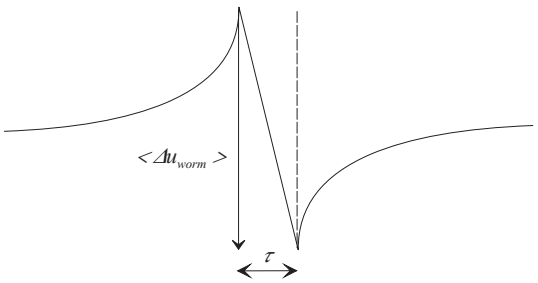

(b) Average all collected events for mean profile

Fig. 3.12: *Detection of worms using a velocity threshold. Individual worms are sign-flipped during the averaging, such that the total average is non-zero.*

shown in Fig. 3.12(b) may result, which resembles a cross-section of a vortical event. This type of studies has been done by Mouri *et al.* [58, 59] and Camussi *et al.* [15, 16].

An alternative method for finding strong events uses the *wavelet* decomposition technique [30]. This algorithm searches, at different scales, for similarities between the velocity signal and a set of probing wavelet functions, which match the profile of a certain type of filamentary vortex. The method seems to produce similar averaged worms ([64]), but assumes that turbulence is a collection of vortices of different radii and amplitudes.

Another category of experiments focuses on the relevance of the worms to anomalous scaling. Experiments of Belin *et al.* [9] show that a relatively large number of worms has to be removed from the initial time-series to observe a change in the longitudinal scaling anomaly. In their case, worms were defined as velocity increments that exceed a given threshold, such as in Fig. 3.12(a). From performing a Reynolds number dependence study, they conclude that worms undergo a structural change at $Re_\lambda \cong 700$, where it is believed that such objects are "dissolved" in the turbulent background. In the work of [64], it is argued that, despite the fact that removal of worms from the original time-series reduces the scaling anomaly of the high order structure functions, they might not be respon-

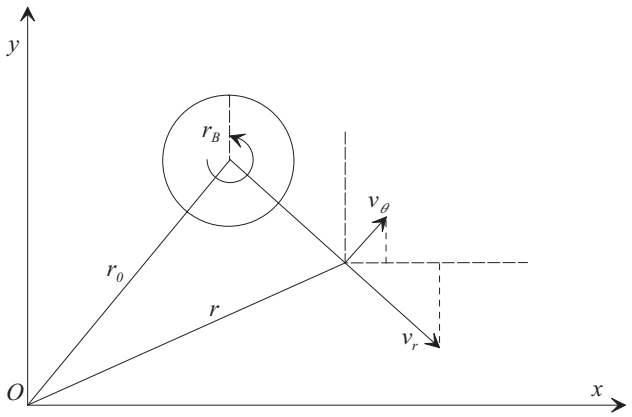

Fig. 3.13: *The contribution to the longitudinal velocity field from a single Burgers vortex situated at* $\mathbf{r_0}$ *at a point* r*. Since the axis of the vortex is perpendicular to the* xOy*-plane, there is no* z*-direction velocity contribution.*

sible for statistical intermittency. Worms are conditioned in [64] on the pressure drops recorded by an additional local pressure sensor and used to compute the structure functions of the "filament" phase of turbulence. Their scaling exponents show a much stronger anomaly than the original velocity signal. However, also their third order structure function has an exponent less than 1, such that the relative scaling exponents behave similarly to those of the original velocity signal. This observation spoils the idea that the extracted vortex filaments are responsible for the departures from the K41 description.

While all of the above experimental work was performed either with single-wire measurements or with a $\times$-probe (which can measure two orthogonal velocity components), in the situation of our multipoint measurement, we can compare the velocity signals from physically separated probes, rather than probing in the time direction. In this way we can investigate the space-time structure of the small-scale velocity field. In the next section we will describe a way to search for strong vortical events using this extended information. We will evaluate the efficiency of the method for a model turbulent velocity field made from vortices.

3.6.2 Eduction of vortices: a Burgers model

In this section we will discuss how to educt vortical events from a velocity field using information about the x-component of the velocity field in the xy-plane $u(x, y)$. This is also the information that can be obtained experimentally, but with the restriction that y takes only the discrete locations y_i of the individual velocity probes. As a test, we will apply this method to a model turbulent field

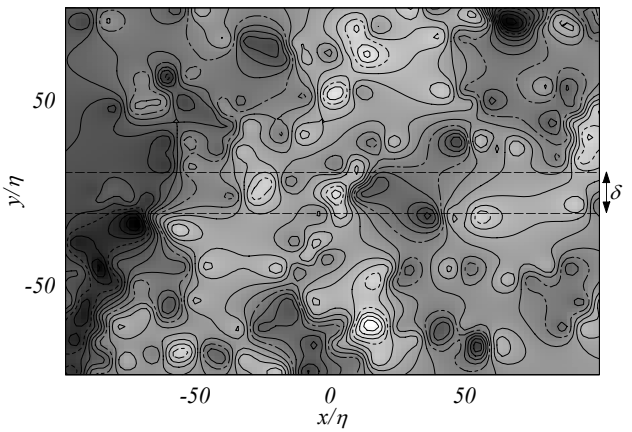

Fig. 3.14: *The longitudinal velocity fields generated by a random superposition of Burgers vortices with equal radii $r_B = 4\eta$ and Reynolds numbers $Re_\Gamma = 2000$. The fields from each of the $N_B = 100$ vortices are computed over a square surface with side $L = 100\eta$. Conditional averaging is applied in either the longitudinal x- or transverse y-direction for velocity increments over separations δ.*

which consists of a random collection of Burgers vortices. There are two ways to look for large velocity increments in the velocity field information that we have. The first manner is to look for large velocity increments

$$\Delta u_L^\delta(x,y) = u(x+\frac{1}{2}\delta, y) - u(x-\frac{1}{2}\delta, y) \tag{3.16}$$

that are local maxima in y. The second manner is to look for large transverse increments

$$\Delta u_T^\delta(x,y) = u(x, y+\frac{1}{2}\delta)) - u(x, y-\frac{1}{2}\delta)) \tag{3.17}$$

that are local maxima in x. The separation δ serves as our probing distance. We will argue that the second arrangement is more efficient to detect vortical events. The requirement of a local maximum distinguishes this method from other methods were velocity increments are compared to a threshold value. The idea is that a vortical structure has a single maximum Δu^δ, surrounded by many large values of Δu. Threshold methods will count all these large values as structures. To decrease the noise sensitivity of the local maximum, a finite-sized region around a found maximum can be set in which no further local maxima are sought. The proposed algorithm is so simple that it can easily be applied in a experiment. In order to test it, we apply it to a model turbulent velocity field that we make from a random collection of Burgers vortices.

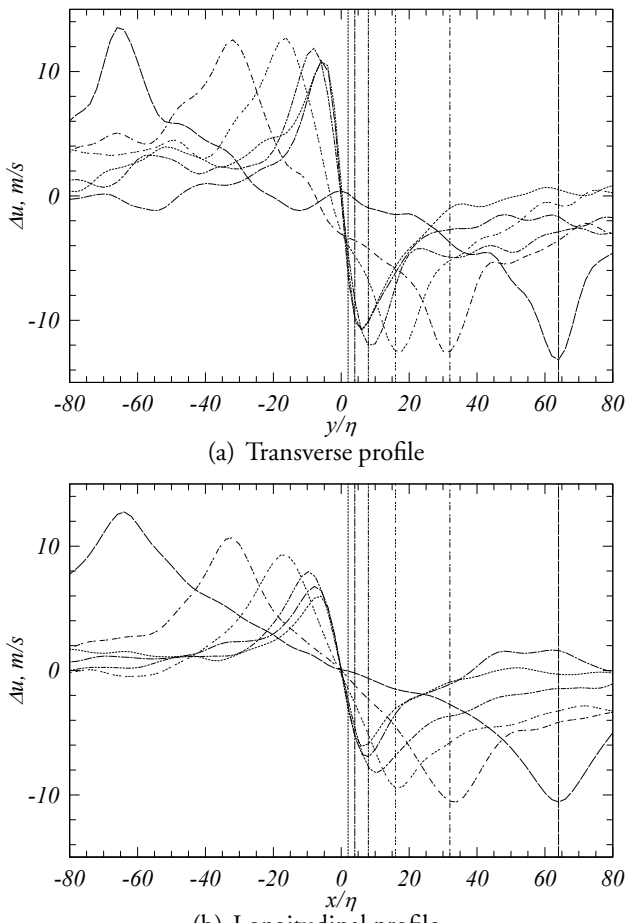

Fig. 3.15: *Average of the N=64 events from conditional averaging of 1000 different realizations of velocity fields as in Fig. 3.14. Several separations* $d/\eta = 4, 8, 16, 32, 64, 128$ *are probed in both longitudinal and transverse directions, while the total field is generated from vortices with constant radius* $r_B = 4\eta$ *and* $u_B = 50\nu/\eta$ *. They are indicated by dashed lines, matching the style of the mean profiles.*

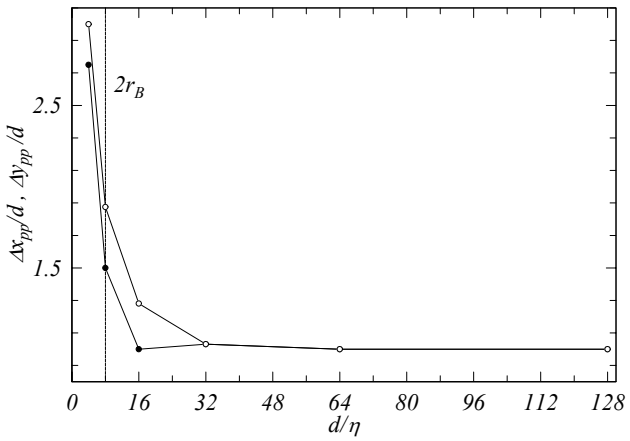

Fig. 3.16: *Separation between the positions of the velocity maxima observed in the mean longitudinal (○) and transverse (●) worm profiles in Fig. 3.15. The values are normalized by the expected separations d/η at which the conditional averaging is performed. Deviations from the trivial value 1 are observed when d/η is comparable to the diameter of the vortices used in the simulation (dashed-lines).*

The Burgers vortex is an exact solution of the Navier-Stokes equation. The velocity field is the sum of a vortical part $\mathbf{u}_v$ and a background strain field $\mathbf{u}_s$ that supplies the energy which the vortex loses to viscous dissipation

$$\mathbf{u}(r,\theta,z) \equiv (u_r, u_\theta, u_z) = \mathbf{u}_s + \mathbf{u}_v = \tag{3.18}$$

$$= (-ar, 0, 2az) + (0, u_\theta, 0), \tag{3.19}$$

with

$$u_\theta(r) = \frac{\Gamma}{2\pi}\frac{1-\exp(-r^2/r_B^2)}{r} \tag{3.20}$$

and $a = 2\nu/r_B^2$. This approach has been used before to model statistical properties of turbulence. Hatekeyama and Kambe [43] studied uniform spatial distributions of Burgers vortices which all had the same strength. They obtained convincing scaling behavior of the third order structure function, but it can be shown that this owed to the presence of the strain field $\mathbf{u}_s$ alone. For modeling turbulence, the strain field is problematic as it has an infinitely large velocity difference in infinite space. Hatekeyama and Kambe obtained a finite dissipation rate $\langle\epsilon\rangle$ by introducing a cutoff radius R_0 beyond which the velocity field was set to zero. The value of the R_0 was set to match the resulting $\langle\epsilon\rangle$ to the Kármán-Howarth equation for the third order structure function. Another exact solution of the Navier-Stokes equation is the Lundgren spiral vortex. Random collections

of these vortices, but now with a special strength distribution, were studied by Saffman and Pullin [78] and He *et al.* [44].

The advantage of such turbulence models over (necessarily) low Reynolds-number direct numerical simulations is that the Reynolds number can be selected at will, but the price is the absence of dynamical interactions between the vortices. Another type of turbulence model fields consists of random Fourier modes with a limited dynamical interaction. These so-called kinematic simulations (Fung *et al.* [36]) are often used to study dispersion of contaminants, but they lack structures. Vortex models are intermediate between kinematic simulations and direct numerical computations, but they lack the dynamical interaction between vortices.

The Burgers velocity field (Eq. 3.20) can be scaled by expressing length scales in terms of the Kolmogorov length and velocities in terms of the Kolmogorov velocity $v_K = \nu/\eta$. Indicating the dimensionless quantities with a $\tilde{}$, we have for the x-component of the velocity $u = u_r \cos\theta - u_\theta \sin\theta$,

$$\tilde{u} = -2\frac{\tilde{x}}{\tilde{r}_B^2} - \frac{\tilde{y}}{\tilde{x}^2+\tilde{y}^2}\tilde{u}_B\tilde{r}_B\left(1 - e^{-\tilde{r}^2/\tilde{r}_B^2}\right) \tag{3.21}$$

with u_B the Burgers velocity, $u_B = \Gamma/(2\pi r_B)$. In our simulation we arbitrarily take $\tilde{r}_B = 4$ and $\tilde{u}_B = 50$. From now on we will work with dimensionless quantities and accordingly drop the $\tilde{}$. We next sprinkle N of these vortices on planes with extent $x, y \in [-L/2, L/2]$, with $N = 10^2$ and $L = 10^2$. Longitudinal and transverse increments over separations δ were obtained as

$$\Delta u_L^\delta(y) = u(x = \frac{1}{2}\delta, y) - u(x = -\frac{1}{2}\delta, y) \tag{3.22}$$

and

$$\Delta u_T^\delta(x) = u(x, y = \frac{1}{2}\delta)) - u(x, y = -\frac{1}{2}\delta)). \tag{3.23}$$

By considering $M = 10^3$ of such planes, very long strips $x \in [0, M \cdot L]$ are obtained. This is equivalent to the experiment, where very long planar strips are obtained through very long sampling times and invocation of Taylor's frozen turbulence hypothesis.

On these intervals, the N_m largest of the local maxima in $|\Delta_T^\delta(x)|$ and $|\Delta_L^\delta(y)|$ are sought. Next, the locations x_i, $i = 1 \ldots N_m$ of these maxima are aligned and the "atmospheres" around them are averaged, such that if $\Delta_{T,L}^\delta u < 0$, the sign of the atmosphere is reversed (otherwise the average would be zero). The result of this procedure is shown in Fig. 3.15. While the transverse procedure reveals the typical transverse $\sim y/(x^2+y^2)$ profiles of the vortices, the surprise is that also the longitudinal conditioning gives profiles $x/(x^2+y^2)$, whereas the longitudinal profile of a vortex is the single-bumped $1/(x^2+y^2)$. Clearly, the conditional

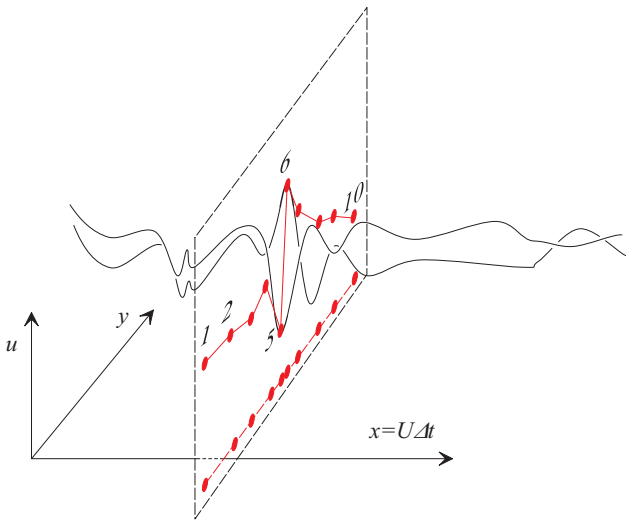

Fig. 3.17: *Detection of worms using a multipoint transverse setup. The velocity signals from two central individual probes are compared at equal time. The •-dashed-line represents the y-coordinates of all the sensors, while the •-solid-line the instantaneous velocity at each sensor, at the moment a worm is detected.*

averages of Fig. 3.15 are at least partly determined by the condition, which generates a longitudinal signature of non-existent vortices. Still, there are significant differences between the longitudinal and transverse averages. For probing separations $\delta \approx 2r_B$, the transverse vortices are almost a factor of 2 larger than the longitudinal ones. For large separations $\delta > 2r_B$, the distance between the velocity maxima in Fig. 3.15 is the same as the probing separation δ. However, when δ is close to r_B, the transverse arrangement reproduces more accurately the size of the vortices.

We conclude that the transverse probing is more sensitive to vortical events than longitudinal probing, but that the shape of the mean large event is for a large part determined by the chosen manner of conditional averaging.

After performing these conditional averages on the experimental signal in the next section, we will devise another test to assess the significance of the result on conditional averages.

3.6.3 Experimental results of conditional averaging

The realization of our algorithm in an experiment that provides time series of u-velocities in many discrete points is sketched in Fig. 3.17. In order to resolve small transverse separations, we focus on the time-signals of the pair of central

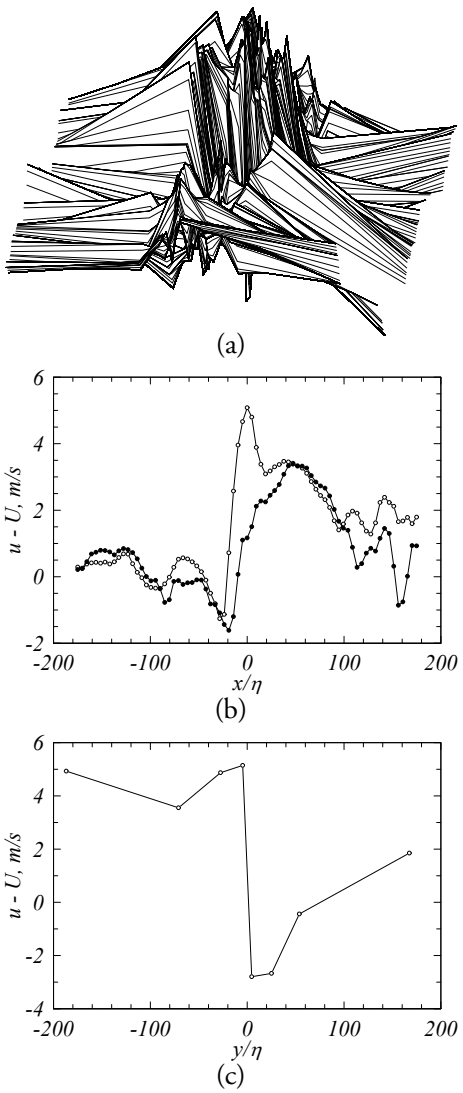

Fig. 3.18: *Single strong event isolated from the multipoint measurements and its neighborhood. The entire velocity field from the 10 sensors is shown in (a), with the event in the center of the approximately square region. The figure was created by representing the longitudinal velocity amplitude against the two available directions: longitudinal (from the time-series via the Taylor hypothesis) and transverse (from different sensors in the array). Separations are normalized on the Kolmogorov dissipation scale η, and the side of the region is $l \sim 400\eta$. In (b), a longitudinal section is made through this surface and only the velocity from the central probes 5 and 6 is shown. The occurrence of a very high velocity increment is clearly visible. The transverse profile of the event is shown in figure (c), by combining the velocity at the moment of the event from all probes.*

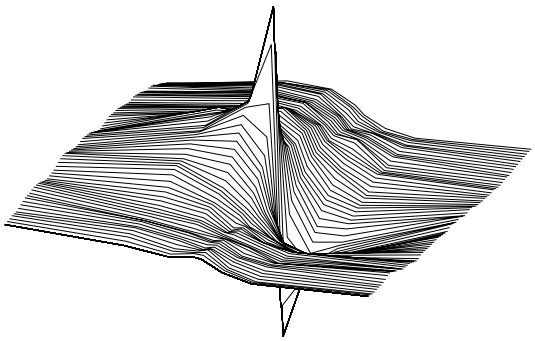

(a) Mean worm surface

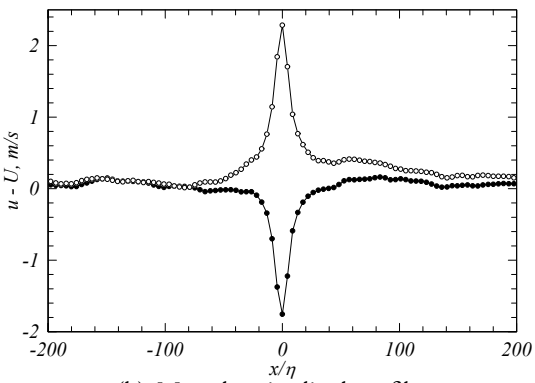

(b) Mean longitudinal profile

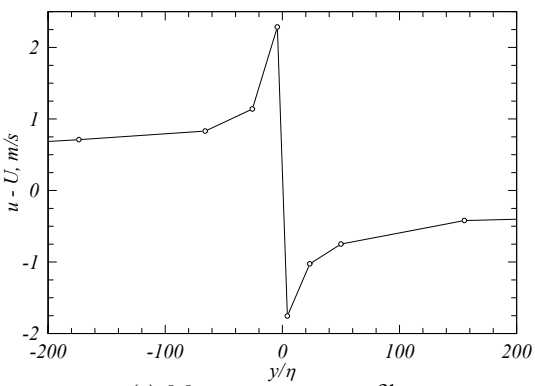

(c) Mean transverse profile

Fig. 3.19: *Average of N=256 events found from conditional averaging in the transverse direction.*

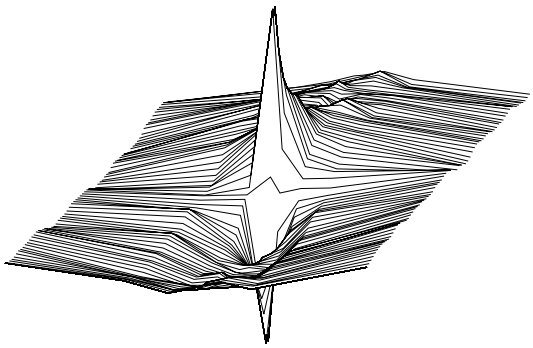

(a) Mean worm surface

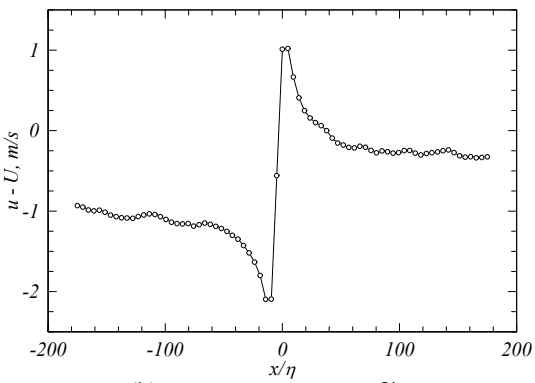

(b) Mean transverse profile

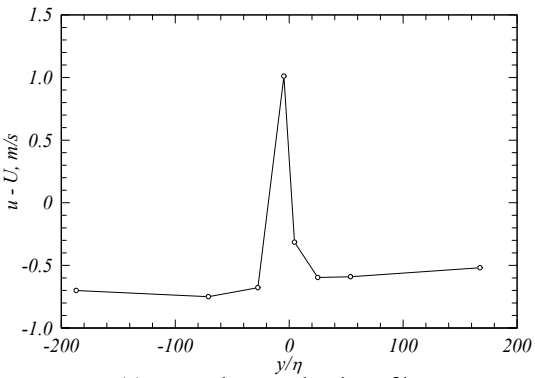

(c) Mean longitudinal profile

Fig. 3.20: *Average of N=256 events from conditional averaging in the longitudinal direction.*

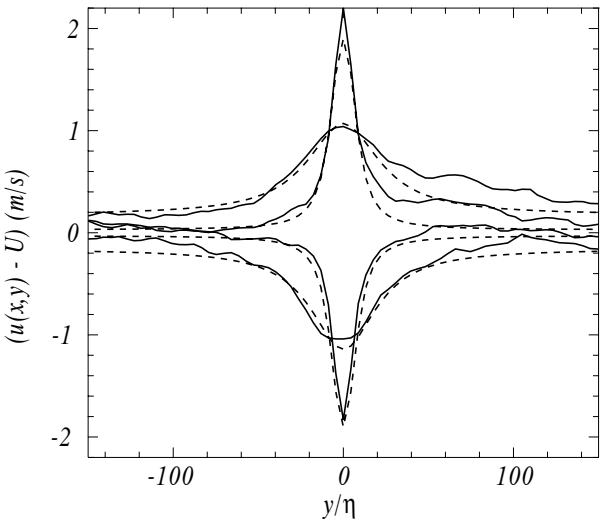

Fig. 3.21: *Fit of the mean velocity surface obtained from conditional averaging in the transverse direction (Fig. 3.19) to the velocity signature of a single Burgers vortex (equation 3.21). The curves (full-lines) correspond to several longitudinal slices through the mean worm surface in Fig. 3.19 and correspondingly through the fit surface (dashed lines).*

probes, whose separation is a mere $r/\eta \approx 6.1$. The velocity difference between these sensors (in positions 5 and 6 in the array) is monitored in time, and a list of the strongest increments is collected. An event is selected when the velocity difference reaches a maximum in time (x).

The additional spatial velocity information (from the other 8 probes) at the moment of the event is also stored and will be used for averaging the planar velocity information of the large events. The list of selected events is ordered decreasingly with respect to the absolute value of the velocity jump. This strength hierarchy is updated every time a new candidate is found, such that the large ones advance up the list and the weak ones are gradually removed. The length of the list stays constant and determines the total probability level of finding the selected events. The amplitude of the weakest event in our list is set by this fixed probability level. A natural question is what probability level determines an event as "rare"? To answer this question we turn back to the structure functions of order p. Moments of increasing p are increasingly influenced by intermittency. As a large moment is still accessible in the experiment, we arbitrarily set $p = 10$. Figure 3.6 demonstrates that the measured ζ_{10}^T is 30% smaller than the self-similar $p/3$. In section 3.5 it is estimated (Fig. 3.10) that the large velocity increments that contribute most to this order have probability $p \cong 2 \cdot 10^{-6}$. This number is

computed from the probability density function. Although the PDF deals with individual velocity increments and is blind to structures, we take this probability level as reference. Thus, in a time series of 10^8 samples, for each sensor there are $2 \cdot 10^{-6} \times 10^8 \cong 200$ large velocity increments that determine principally the $p = 10$ moment. Accordingly, we search for the N=256 strongest events in our measured time-series.

We give in Fig. 3.18 an example of one the most violent events extracted from the experimental run with $Re_\lambda \sim 840$. The size of the velocity excursion is $\Delta u_{max} = 7.94 m/s$, comparable to the mean velocity $U = 11.69 m/s$ and 5 times larger than $u_{rms} = 1.58 m/s$. The transverse separation over which this gradient is recorded is a mere $\delta_{56}/\eta \approx 9$.

We align all the 256 events and then average them, including in this procedure the velocity information from the neighboring sensors. This results in a mean worm profile $u(x,y)$, where the square x,y extends to the integral scale of the flow.

The result of the averaging is shown in Fig. 3.19. It resembles very closely the signature of a filamentary vortex. To be able to better quantify this observation, we shall compare the mean surface with the corresponding velocity signature of a Burgers vortex. We make the following simplifying assumption: given the geometry of the sensor array and the low probability threshold we use for extracting worms, it is very likely that only filaments along the z-axis would be selected. The model vortex (defined in Eq. 3.21) to which we fit the experimental outcome is oriented accordingly.

In Fig. 3.21 the outcome of the fitting procedure is shown; we obtain that the mean worm matches a Burgers vortex with radius $r_B \cong 7\eta$, but the background strain rate is a factor of 2 too large. Since the precise shape of the mean velocity profile is partly determined by the imposed condition, we do not wish to emphasize the discrepancies of the fit and the measured profile of Fig. 3.21. Still, it is a quite remarkable coincidence that our data actually resemble the Burgers vortex that was used to verify our conditional algorithm.

A conditional algorithm can also be done in the longitudinal direction in a similar fashion as in the transverse case. The difference is that we look for local maxima of Δu in the velocity signal of a single probe. We use the velocity readings of the other probes to obtain the structure of the velocity field near these maxima. As spatial separations are now obtained from time delays through the Taylor hypothesis, this may become a problem when large velocity excursions are sought. The longitudinal separation δ over which the largest velocity differences are pursued is set equal to that used in the transverse case through selecting the the time delay as $\Delta\tau = \delta/U$. The mean event from the longitudinal conditional average is shown in Fig. 3.20. In agreement with our findings from the random

Burgers vortices fields, we find that the longitudinal mean profile resembles a vortex, but oriented wrongly. It is clearly an artifact of the conditional average. Also in agreement with the random Burgers collection, we find that the magnitude of the transverse vortex is larger than that of the longitudinal one.

This leads to the preliminary conclusion that the transverse mean structure is genuine, whereas the longitudinal structure is an artifact of the conditional average. By devising yet another test in the next section, we will seek support for this conclusion.

3.6.4 Randomizing the velocity field

We will now test the significance of our experimental results by applying our algorithm to pseudo-turbulence: that is an experimental velocity signal that has the same characteristics as our turbulent flow, but whose phase coherence is completely destroyed. We have verified that the pseudo-turbulence data has the same energy spectra and the same second-order structure functions. Since both longitudinal and transverse velocity increments of the scrambled data are now Gaussian, the scaling exponents follow the self-similar $\zeta_p = \zeta_2 \cdot \frac{p}{2}$.

Let us now discuss in detail how this is done for our multi-probe velocity signal. Using an array of velocity sensors we measure the planar distribution of a single velocity component $u(x, y)$ in discrete and non-equidistant points y_i. The Fourier-transformed field is

$$u(\boldsymbol{k}) = \frac{1}{2\pi} \int_{-\infty}^{\infty} \mathrm{e}^{-i\boldsymbol{k}\cdot\boldsymbol{x}} u(\boldsymbol{x})\, \mathrm{d}\boldsymbol{x}, \tag{3.24}$$

with its inverse

$$u(\boldsymbol{x}) = \int_{-\infty}^{\infty} \mathrm{e}^{i\boldsymbol{k}\cdot\boldsymbol{x}} u(\boldsymbol{k})\, \mathrm{d}\boldsymbol{k}. \tag{3.25}$$

If a two-dimensional Fourier transform could be done, a randomized field with the desired property would be

$$\tilde{u}(\boldsymbol{x}) = \iint_{-\infty}^{\infty} |u(\boldsymbol{k})|\, \mathrm{e}^{i\theta(\boldsymbol{k})}\, \mathrm{d}\boldsymbol{k}, \tag{3.26}$$

with $\theta(\boldsymbol{k})$ a uniform random function. We can define Eq. 3.26 with or without the absolute value.

Reality of the signal $u(\boldsymbol{x})$ requires that the complex conjugate $u^*(\boldsymbol{k}) = u(-\boldsymbol{k})$, so that

$$\left(u(\boldsymbol{k})\, \mathrm{e}^{i\theta(\boldsymbol{k})}\right)^* = u^*(\boldsymbol{k})\, \mathrm{e}^{-i\theta(\boldsymbol{k})} = u(-\boldsymbol{k})\, \mathrm{e}^{-i\theta(\boldsymbol{k})},$$

and the random phase must satisfy $\theta(\boldsymbol{k}) = -\theta(-\boldsymbol{k})$. As already announced above, the randomization Eq. 3.26 leaves all second-order correlations invariant.

$$\langle \tilde{u}(\boldsymbol{x}+\boldsymbol{r})\, \tilde{u}(\boldsymbol{x}) \rangle = \left\langle \iint \mathrm{e}^{i(\boldsymbol{k}\cdot\boldsymbol{x}+\boldsymbol{k}'\cdot(\boldsymbol{x}+\boldsymbol{r}))}\, u(\boldsymbol{k}) u(\boldsymbol{k}')\, \mathrm{e}^{i(\theta(\boldsymbol{k})+\theta(\boldsymbol{k}'))}\, \mathrm{d}\boldsymbol{k}\, \mathrm{d}\boldsymbol{k}' \right\rangle. \tag{3.27}$$

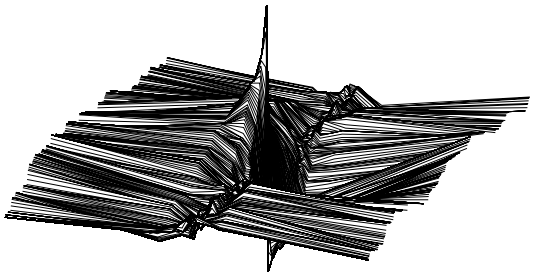

(a) Mean worm surface

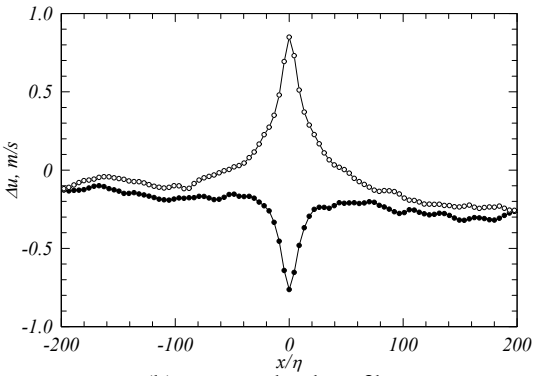

(b) Longitudinal profile

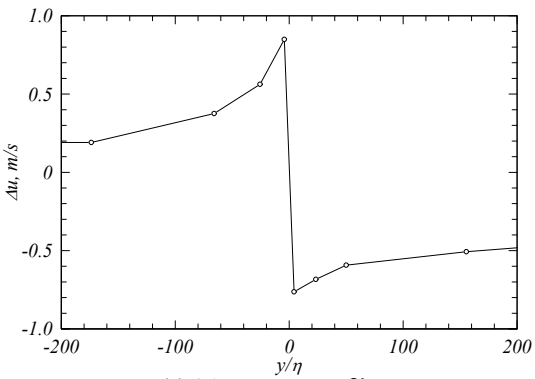

(c) Transverse profile

Fig. 3.22: *Average of N=256 the events from conditional averaging of the phase-randomized velocities in the transverse direction.*

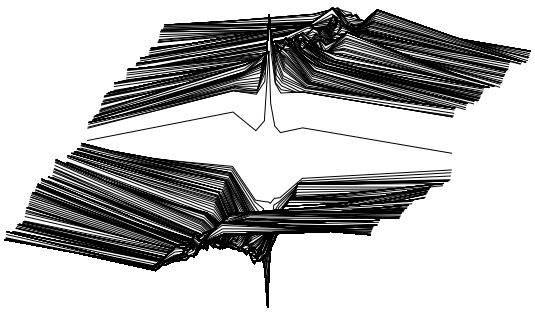

(a) Mean worm surface

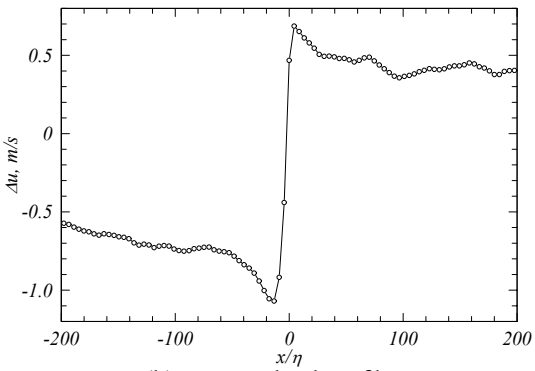

(b) Longitudinal profile

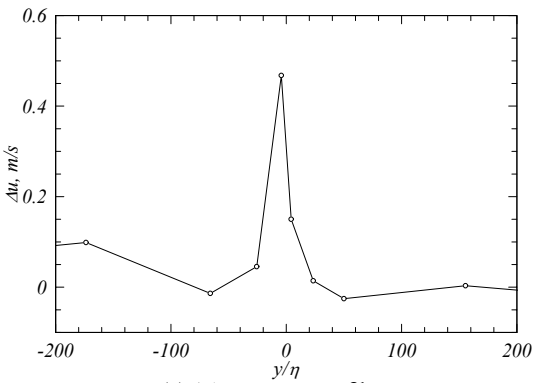

(c) Transverse profile

Fig. 3.23: *Average of N=256 events from conditional averaging the phase-randomized velocities in the longitudinal direction.*

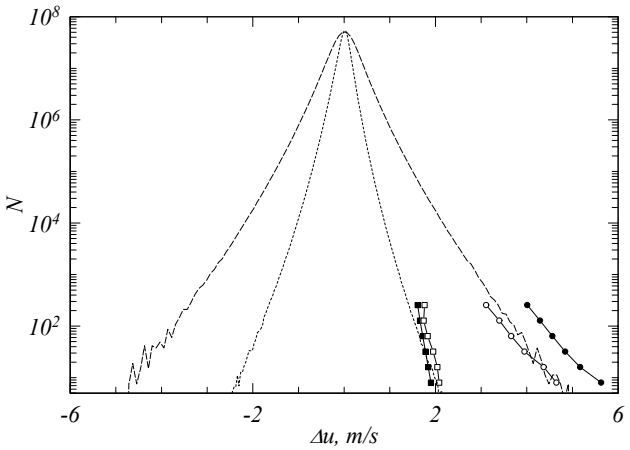

Fig. 3.24: *Dependence of the amplitude of mean worms, found at separations $r/\eta \sim 9$, on the length of the search list N. The results (•, ∘ original data, ■, □ scrambled data; filled, empty markers: transverse, respectively longitudinal worms) are compared to the corresponding probability distribution functions of velocity increments $\mathcal{P}^{T,L}_{r/\eta}(\Delta u)$ (long-, respectively short-dash lines).*

Homogeneity (independence on $\boldsymbol{x}$) introduces the delta function $\delta(\boldsymbol{k}+\boldsymbol{k}')$, so that the random phases cancel, while

$$\left\langle \iint \mathrm{e}^{-i\boldsymbol{k}\cdot\boldsymbol{r}} |u^2(\boldsymbol{k})|\, \mathrm{d}\boldsymbol{k} \right\rangle = \langle u(\boldsymbol{x})u(\boldsymbol{x}+\boldsymbol{r})\rangle\,. \tag{3.28}$$

The sensor array that we use has highly unevenly spaced probes in the $y-$direction, which precludes a (discrete) Fourier transform in this direction. Instead, we perform a randomization only in the time-like ($x-$) direction. Equation 3.26 now reads explicitly in the x, y plane

$$\tilde{u}(x,y) = \iint_{-\infty}^{\infty} \mathrm{e}^{i(xk_x+yk_y)}\, u(k_x,k_y)\, \mathrm{e}^{i\theta(k_x,k_y)}\, \mathrm{d}k_x\, \mathrm{d}k_y.$$

With randomization in x only, this becomes

$$\tilde{u}(x,y) = \int_{-\infty}^{\infty} \mathrm{e}^{i(xk_x+\theta(k_x))}\, \mathrm{d}k_x \int_{-\infty}^{\infty} \mathrm{e}^{iyk_y}\, u(k_x,k_y)\, \mathrm{d}k_y = \int_{-\infty}^{\infty} \mathrm{e}^{i(xk_x+\theta(k_x))}\, u(k_x,y)\, \mathrm{d}k_x. \tag{3.29}$$

Trivially, this procedure leaves correlations in the $y-$direction invariant

$$\begin{aligned} \langle \tilde{u}(\boldsymbol{x}+\boldsymbol{r})\tilde{u}(\boldsymbol{x})\rangle &= \left\langle \iint \mathrm{d}k_x \mathrm{d}k'_x \mathrm{e}^{i[xk_x+\theta(k_x)+xk'_x+\theta(k'_x)]} u(k_x,y)u(k'_x,y+r) \right\rangle \\ &= \int \mathrm{d}k_x \left\langle u(k_x,y)\, u(-k_x,y+r)\right\rangle = \langle u(x,y)u(x,y+r)\rangle\,. \end{aligned} \tag{3.30}$$

Although Eq. 3.29 treats the two spatial directions undemocratically, it is a true randomization which does affect all higher order correlations. This is because higher order moments of the undemocratically randomized field $\tilde{u}(x,y)$

$$\langle \tilde{u}^p(x,y)\, \tilde{u}^q(x,y+r)\rangle$$

cannot be expressed in those involving the original field $u(x,y)$.

Following closely the analysis of section 3.6.3, we apply the worm selection procedure to the scrambled fields, extracting as usual the strongest N=256 longitudinal and transverse events. It doesn't come as a surprise that the mean large events extracted from the scrambled data, shown in figures 3.22 and 3.23 again have a vortical signature. However, the amplitudes of the events are significantly different in this case.

Let us indicate by $\Delta u_W^{T,L}$ the largest velocity increments of a mean transverse and longitudinal event, respectively, and by $\Delta u_{WR}^{T,L}$ the corresponding quantities for the randomized signal. Quantitatively, the amplitude of the scrambled worms is smaller than in the real case. In the case of transverse mean events, their ratio is $\langle \Delta u_W^T\rangle / \langle \Delta u_{WR}^T\rangle \sim 2.5$, higher then the ratio of the longitudinal worms $\langle \Delta u_W^T\rangle / \langle \Delta u_{WR}^T\rangle \sim 1.9$. In contrast to the original worms, the scrambled transverse and longitudinal mean profiles have similar amplitudes, $\langle \Delta u_{WR}^T\rangle = 1.61 ms^{-1}$ and $\langle \Delta u_{WR}^L\rangle \sim 1.75 ms^{-1}$.

Let Δu be the size of the largest event found among the N largest. The function $N(\Delta u)$ can be compared to the probability density functions of indiscriminate large velocity increments from which we can form

$$N_t \left(\int_{-\infty}^{-\Delta u} (P) dx + \int_{\Delta u}^{\infty} (P) dx \right),$$

with N_t the total number of velocity samples. Such a comparison has been done in Fig. 3.24, which allows a clear discrimination between the longitudinal and transverse conditions, a distinction which disappears for the pseudo-turbulence field.

In view of the results of the phase-randomization tests, we can conclude that the transverse arrangement of probes is more efficient in capturing large vortical events of the turbulent flow. Before we proceed, we would like to draw attention to some additional interesting observations.

3.7 Worm contributions to anomalous scaling of structure functions

Intermittency is the occurence of strong events in turbulence which gives rise to strongly non-Gaussian PDFs. As we have now identified these events in an ex-

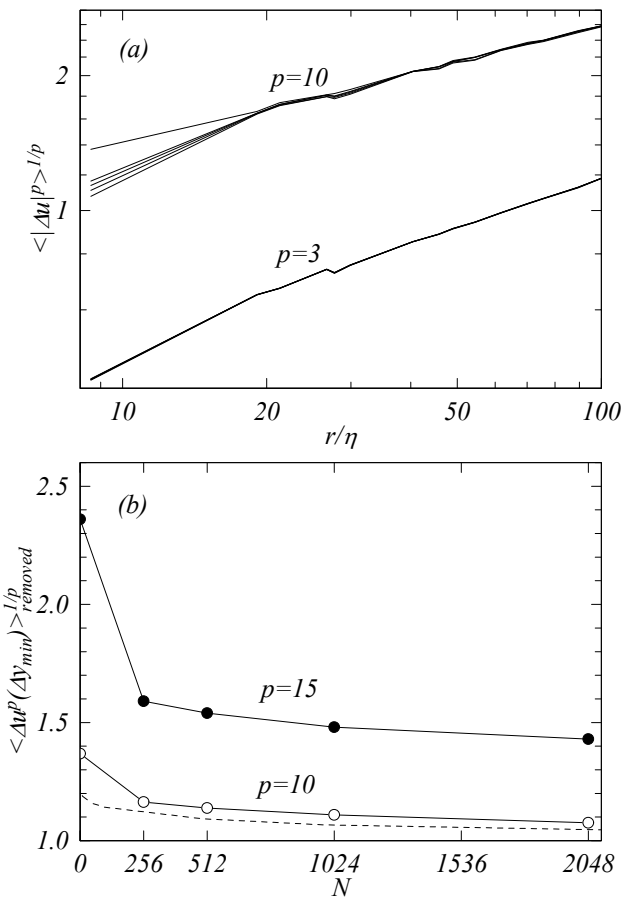

Fig. 3.25: *Effect of worm removal from a* single *pair of hot-wires on the transverse structure function S_p^T. (a) When N=256 worms that are found at separation Δy (here $\sim 9\eta$) are removed, the structure function at other separations is not influenced. The effect on a small order ($p = 3$) is nearly absent. (b) Full lines: dependence of the structure function at $r/\eta = 9$ on the number of removed large events. Dashed line: dependence of $(\Delta u^{10})^{1/10}$ on the number of removed large velocity increments.*

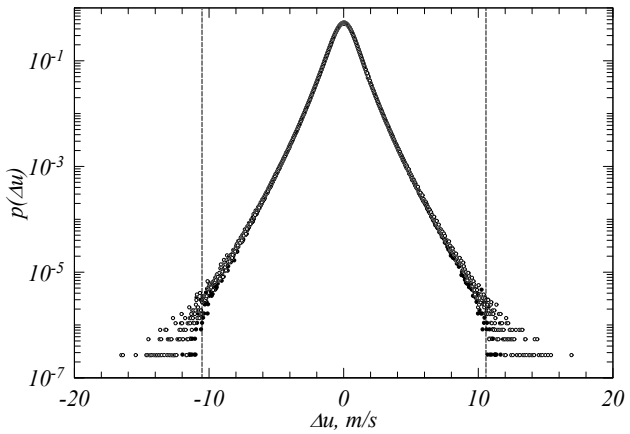

Fig. 3.26: *Probability distribution functions of transverse velocity differences over $\Delta y \sim 9\eta$, total contribution ($\circ$) and after the removal of N=256 worms($\bullet$). The dashed lines indicate the probability level corresponding to this value.*

perimental signal, the question is if the anomalous scaling of structure functions will be reduced if we delete these events from the turbulence signal. Since our identification was successful for the transverse arrangements, we will pose this question for the transverse structure functions.

In section 3.3 we have already concluded that the scaling anomaly of the transverse exponents exceeds that of the longitudinal ones. The result of the previous sections already suggests that a possible explanation may be that the transverse arrangement is more efficient in capturing large events. The influence of the deletion of large velocity increments on scaling properties of the measured velocity field was studied earlier in Belin *et al.* [9] and Chinais *et al.* [64], who removed worms using velocity thresholds from single-wire experiments, and observed that their absence from the time-series decreases the scaling anomaly of high-order longitudinal structure functions. A closer inspection of these experiments reveals that, generally, a relatively large percentage of the turbulent signal has to be removed in order to significantly reduce the scaling anomaly.

Typically, we select from a single pair of probes $N = 256$ events together with their neighborhood which is approximately 400 samples wide. For an experimental run with $\sim 10^8$ samples, this amounts to removing from the time series only a fraction 10^{-3} of the data per sensor. This number is considerably smaller than that of previous studies.

First, we will investigate if worms collected at dissipative scales are significant for the anomalous scaling observed at the larger scales in the inertial range. To that purpose, we repeatedly apply the conditional averaging procedure over the

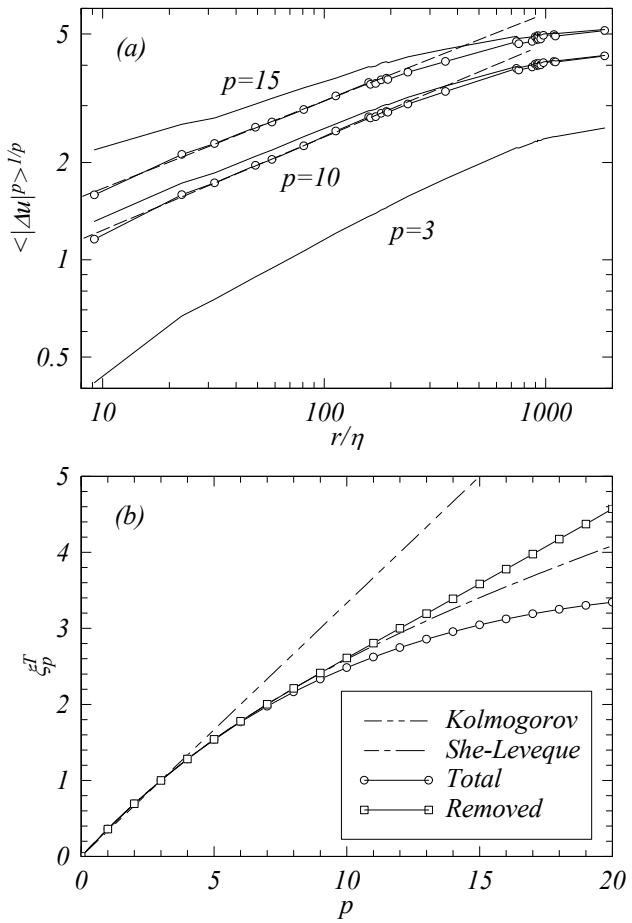

Fig. 3.27: *The removal of N=256 worms from* each *separation r/η in the transverse structure functions modifies their apparent scaling (a) for high orders p. In (b) the effect of the removal is compared to the initial scaling and the Kolmogorov and She-Leveque predictions, via the dependence of the transverse scaling exponents ζ_p^T on the order p of the structure function.*

same smallest transverse separation, $y_0/\eta \sim 9$, and collect increasing numbers of worms. The transverse structure functions of various orders are then computed without the worms and their "atmospheres". As Fig. 3.26 illustrates, this procedure removes the large velocity increments from the tails of the probability density function, but it is not a sharp cutoff. From these PDFs we compute the structure functions ${G'}_p^{T,L}(y)$.

The dependence of the transverse ${G'}_p^T(y)$ on the number of the removed worms is shown in Fig. 3.25(a), for two orders $p = 3,\ 10$ and inertial range scales close to y_0/η. A relatively small number of events (256) decreases significantly the original $G_p^T(y)$, as shown in Fig. 3.25(b). Removing more worms continues to change the value of ${G'}_p^T(y)$, but in a much slower manner. The structure functions are affected by worm depletion only at high orders, and only at the corresponding scale where the conditional averaging was applied. The longitudinal ${G'}_p^L(y)$ are not shown, but they are completely unaffected by the removal of transverse worms. Additionally, it is shown in Fig. 3.25(b) that worm removal is slightly more effective than indiscriminate removal of a similar number of large velocity differences. The latter was evaluated by truncating the the tails of the PDFs as described in section 3.5.

It is not possible to remove worms that are conditioned at scales larger than the lower bound of the inertial range ($r/\eta \cong 30$) and retain algebraic inertial range structure functions. Instead, it is necessary to remove worms at each separation δ separately, by conditioning on the same separation. In this way, the removed events depend on the scale. The resulting structure functions ${G''}_p^T(y)$ have scaling behaviour and enable to determine the scaling exponents. Our deletion procedure very efficiently influences anomalous scaling. Removing a mere 0.1 % of the data significantly reduces the transverse anomalous scaling in the high orders. While the transverse scaling exponent of the original data indicated a stronger intermittency, $\zeta_p^T < \zeta_p^L$ (Fig. 3.6), this trend has now been reversed for the data with the large events removed.

3.8 Conclusions

We performed an extensive study on the extraction of small-scale vortex filaments (worms) from high Reynolds number near-isotropic turbulence.

The key question was wether a measurement of transverse velocity increments is perhaps more sensitive to intermittency than a measurement of longitudinal increments. A multipoint hot-wire anemometry setup was used to extract planar velocity fields, from which we computed longitudinal and transverse structure functions. We found that their scaling exponents are anomalous, but

different from each other $\zeta_p^T < \zeta_p^L$.

A possible connection between the scaling anomaly and worms was assessed in several steps. First, a structure oriented conditional averaging method was devised to select worm candidates from large velocity increments, either in the longitudinal or transverse directions.

Then, we tested the conditional averaging on a toy-model of turbulence which consisted of a random superposition of Burgers vortices of fixed radii and strengths. Average worms extracted from the synthetic velocity fields have profiles reminiscent of the velocity signatures of the original vortices. Closer inspection revealed that the velocity profiles of average worms are influenced by the conditioning procedure, such that longitudinal worms cannot be associated with a vortical structure. The conditional averaging procedure is more efficient at detecting vortical structures from the simulation when performed in the transverse direction. A similar behavior was found in the experiment, as was corroborated by a test in which we applied our procedures to pseudo-turbulence.

The overall picture emerging from this study is that large events have primarily a vortical character and should be detected through transverse velocity increments. Only these events can be discriminated from the random background events. Although this may not come as a surprise, we must also realize that the major part of intermittent velocity fluctuations is unstructured. This was illustrated by the effect of removing large events from a measured signal before computing its scaling exponents. When a small number of them are removed from the total velocity fields, they reduce by a significant factor the deviations of the scaling exponents from the Kolmogorov predictions, but the procedure holds only when worms are removed from all scales in the inertial range. Removal of worms extracted from dissipative scales has only local effect on the value of the structure functions, and therefore destroys the scaling behavior. In fact, this is easy to understand: conditioning on a single scale allows to write the measured turbulent velocity fields as the sum of two parts, one containing the large events and a background part. The separation of the two parts is not scale dependent. Then, if the total signal has scaling properties, the part with the large events removed either has the same scaling or has no scaling.

Chapter 4

TURBULENCE ANISOTROPY AND THE SO(3) DESCRIPTION

Abstract

We study strongly turbulent windtunnel flows with controlled anisotropy. Using a recent formalism based on angular momentum and the irreducible representations (SO(3)) of the rotation group, we attempt to extract this anisotropy from the angular dependence of second–order structure functions. In axisymmetric turbulence which has a weak anisotropy, the results are ambiguous. In more strongly anisotropic shear turbulence, the SO(3) description enables to find the anisotropy scaling exponent. The key quality of the SO(3) description is that structure functions are a mixture of algebraic functions of the scale. However, instead of a hierarchical ordering of anisotropies we find that in third–order structure functions of homogeneous shear turbulence the anisotropic contribution is of the same order of magnitude as the isotropic part. We conclude that the SO(3) description *perhaps* is a good way to quantify anisotropy, but our experiments raise many questions.

4.1 Introduction

The application of angular momentum theory to describe anisotropic turbulence is a new and exciting development [55, 5]. Although the idea was proposed earlier [14] and expansion of tensorial quantities using the irreducible representations of the rotation group is well known [47], the current interest is in scaling properties of anisotropic turbulence quantities. These phenomena become accessible in experiments which go beyond the traditional measurement of a single velocity component at a single point in strongly turbulent flows [4, 50].

The idea is that the Navier-Stokes equation is invariant under rotations of space, and, therefore, that statistical turbulence quantities should be expanded preferably in terms of the irreducible representations of the rotation group. In angular momentum theory there is a relation between the value of the angular momentum and the irreducible representation of the rotation group, such that

a higher angular momentum signifies less symmetry. This provides a way to describe the influence of anisotropy on turbulence by the gradual loss of symmetry of turbulence statistical quantities at increasing length scales, and accordingly, an increasing influence of high angular momentum contributions.

As most turbulent flows in the laboratory are anisotropic, and as it recently has become clear that this anisotropy remains, even at the smallest scales, [81] this new description of anisotropy is a very significant development which deserves a careful experimental test. The goal of this paper is to provide such a test by devising experimental techniques in turbulent flows which have a controlled anisotropy.

In order to illustrate this idea, we consider the structure functions

$$G_{\alpha\beta}(\boldsymbol{r}) = \left\langle \left(u_\alpha(\boldsymbol{x}+\boldsymbol{r}) - u_\alpha(\boldsymbol{x})\right)\left(u_\beta(\boldsymbol{x}+\boldsymbol{r}) - u_\beta(\boldsymbol{x})\right)\right\rangle, \tag{4.1}$$

which involve increments of the velocity components u_α and u_β over the separation vector $\boldsymbol{r}$. The ensemble average is denoted by $\langle \ldots \rangle$; homogeneity of the flow implies independence on $\boldsymbol{x}$. Adopting a coordinate system in which we measure the $x-$component of the velocity and where the vector $\boldsymbol{r}$ is represented by (r,θ,ϕ) with respect to the $x-$axis, the angular momentum decomposition of the tensor Eq. 4.1 takes on the following form

$$G_{xx}(r,\theta,\phi) = g_{l=0}(\theta)\, r^{\zeta_2^{(0)}} + g_{l=2}(\theta,\phi)\, r^{\zeta_2^{(2)}} + \ldots, \tag{4.2}$$

where the first term is the isotropic contribution and the term involving g_2 is the first anisotropic part, possibly followed by terms representing higher-order anisotropies. The angle-dependent functions g_l are subject to the incompressibility constraint which completely fixes $g_0(\theta)$. Parity invariance prevents a contribution with $l = 1$. As is implied by Eq. 4.2, each irreducible part may have its own scaling exponent, so that $\zeta_2^{(0)}, \zeta_2^{(2)}, \ldots$ may all be different. Of course, any tensorial quantity can be expanded in irreducible components of the rotation group, [47], but the separation of G_{xx} into angle-dependent factors which multiply algebraic (scaling) functions of r is new. Whilst the $g_l(\theta,\phi)$ coincide with the orthogonal spherical harmonics for a scalar field and for the longitudinal correlations of the velocity field (where the measured velocity component and r point in the same direction), they have a more complicated form in the general case. However, this form can be readily derived using the well-known tools from angular momentum theory in quantum mechanics.

Unlike the non-relativistic Schrödinger equation which is linear, the Navier Stokes equation is nonlinear and the expansion Eq. 4.2 is only appropriate if the anisotropic contributions take the form of small perturbations whose size rapidly decreases with increasing l. Accordingly, the exponents associated with

increasing angular momentum are ordered hierarchically, $\zeta_2^{(0)} < \zeta_2^{(2)} < \ldots$, such that the highest angular momentum contribution decays quickest at decreasing scale r.

Two special forms of $G_{\alpha\beta}(\boldsymbol{r})$ are the transverse structure function $G_2^T(r) \equiv G_{\alpha\alpha}(r\boldsymbol{e}_\beta)$, with $\alpha \neq \beta$, and with $\boldsymbol{e}_\alpha$ the unit vector in the α direction, and the longitudinal structure function $G^L(r) \equiv G_{\alpha\alpha}(r\boldsymbol{e}_\alpha)$. With $\alpha = x$ and $\beta = y$ we were the first to point out that the high–order longitudinal and transverse structure functions may have different scaling exponents [92, 93]. This was also found in other experiments [24] and direct numerical simulations [12, 19]. However, [82] has suggested that this difference disappears at large Reynolds numbers. It must be realized that a dependence of the scaling exponent on the relative orientation of $\boldsymbol{r}$ and the direction of the measured velocity component is *incompatible* with the description Eq. 4.2 in terms of irreducible components. In this description, it is neither the longitudinal nor the transverse structure functions that carry the pure scaling, but rather the different terms of the angular momentum decomposition Eq. 4.2.

In the SO(3) picture, all structure functions $G_{\alpha\beta}(\boldsymbol{r})$ embody a mixture of scalings, with the pure algebraic behavior carried by the irreducible components. In other words, if it is possible to single out these components, a much improved scaling behavior of measured structure functions would be the result in cases where the large-scale anisotropies invade the inertial-range scales, that is at small Reynolds numbers. Such an approach can only be followed in numerical simulations where the full vector information about the velocity field is available.

In case of the longitudinal structure functions $G_2^L(r)$, the SO(3) representations $g_l(\theta,\phi)$ coincide with the spherical harmonics, where its arguments θ,ϕ are the angles of the vector $\boldsymbol{r}$ in $G_2^L(r) = \langle(\hat{\boldsymbol{r}}\cdot(\boldsymbol{u}(\boldsymbol{x}+\boldsymbol{r}) - \boldsymbol{u}(\boldsymbol{x}))^2\rangle$. By projecting onto the spherical harmonics Biferale and Toschi [11] have singled out the isotropic component of longitudinal structure functions of a numerically computed velocity field and demonstrated its superior scaling behavior compared to the ordinary, unfiltered second-order structure function. However, the computed flow was driven strongly inhomogeneously with homogeneity recovered only in a statistical sense. Further, [11] do not report scaling behavior of the ordinary third-order longitudinal structure function, and the Reynolds number was not known, possibly because of the used hyper-viscosity.

Experiments can reach much larger Reynolds numbers than numerical simulations and can average over many large-eddy turnover times. At large Reynolds numbers, there is a clear separation between the inertial-range scales and the scales which are invaded by anisotropies, which may facilitate the analysis. Also, experiments allow a precise control over homogeneity and anisotropy using active [81] or passive grids to stir the flow. However, experiments have limited access to

the velocity field: hot-wire velocimetry provides only a few velocity components in a few spatial points. In the context of experiments, therefore, the question is if the mixture of scaling exponents of Eq. 4.2 gives a better description of measured structure functions than a pure algebraic behavior.

The functional form of the irreducible components $g_l(\theta,\phi), l \geq 2$ depends on the symmetry of the experiment and is determined by parameters that are specific for the kind of flow. With decreasing symmetry, the number of parameters increases. However, the value of the *exponents* $\zeta_2^{(l)}$ is universal. For example, a simple dimensional argument [53] predicts $\zeta_2^{(2)} = 4/3$ for the first anisotropy exponent.

In an experiment one must try to determine both the universal exponents and the non-universal constants that parametrize the angle-dependent $g_2(\theta,\phi)$. The large number of adjustable parameters is a problem: with so much freedom it is often not difficult to obtain a better fit of the data and it becomes unclear if an improved fit is the consequence of the specific anisotropy description Eq. 4.2, or of the large number of adjustable constants. In this paper we will design experiments such as to actually *minimize* the number of constants, and simultaneously maximize the experimental information.

Clearly, experiments must now measure both the $r-$ and the angle (θ,ϕ) dependence of the structure functions, which calls for more sophisticated setups than the common single point, single velocity component experiments that give access to the longitudinal structure function only. Using multiple velocity probes that measure a singe velocity component, Fig. 4.1 sketches two ways to measure both r and θ dependence of the structure function. The idea is to combine true spatial separations with temporal delays, which in turn translate into spatial separations using the Taylor frozen turbulence hypothesis. In the first manner (method i), exploited by [5, 50], both r and θ dependencies are measured simultaneously by time-delaying the signal of one of the two probes used. If the frozen turbulence hypothesis holds, the angle θ is given by $\theta(r) = \sin^{-1}(r_0/r)$, with $r^2 = r_0^2 + (U\tau)^2$, where U is the mean velocity and τ is the time delay.

By using arrays of many probes (method ii) , Fig. 4.1b illustrates that it is possible to measure the $r-$ and $\theta-$dependence of structure functions separately. Obviously, method (i) provides quite limited information about the structure function. The information gained about the anisotropic velocity field in method (ii) is one of the key points of this paper.

Using straightforward angular momentum theory (Clebsch-Gordan algebra), it is possible to arrive at explicit expressions for the irreducible components $g_l(\theta,\phi)$ of the second-order structure function. Here, it suffices to list the result for flows with decreasing symmetry. We will specialize the formulas for our case, in which we measure the $x-$component of the fluctuating velocity in ax-

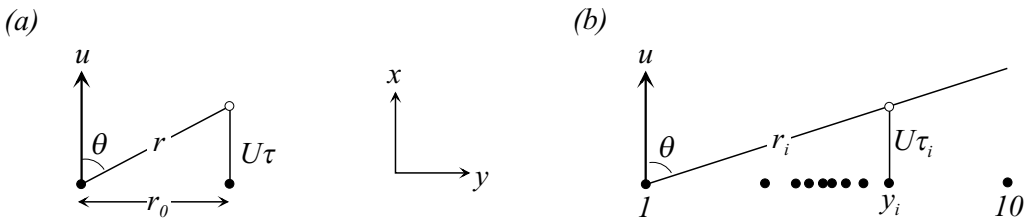

Fig. 4.1: *Probe geometries for measuring both $r-$ and $\theta-$dependence of structure functions. (a) With two probes, r and θ are related through the time delay τ, $\theta = \tan^{-1}(r_0/U\tau)$, $r^2 = r_0^2 + (U\tau)^2$. (b) With 10 probes, r spans 45 discrete values, and θ can be varied independently by selecting time delays $\tau_i = y_i/(U\tan\theta)$.*

isymmetric and shear turbulence. The used coordinate system is sketched in Fig. 4.2.

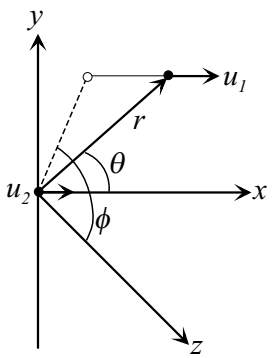

Fig. 4.2: *Coordinate system: velocity increments $u_1 - u_2$ are measured over a vector $\mathbf{r}$ with the measured velocity component pointing in the $\mathbf{e}_x-$direction.*

In the case of *axisymmetric* turbulence, all statistical quantities are invariant under rotations around the $x-$axis, that is, $G_{xx}(r,\theta,\phi)$ becomes independent of ϕ.

$$\begin{aligned} G_{xx}(r,\theta) &= g_0(\theta)\, r^{\zeta_2^{(0)}} + g_2(\theta)\, r^{\zeta_2^{(2)}} \\ &= c_0 \left\{ 2 + \zeta_2^{(0)} \sin^2\theta \right\} r^{\zeta_2^{(0)}} + \\ &\quad \left\{ d_1 + d_2\cos(2\theta) + \kappa(d_1, d_2, \zeta_2^{(2)})\cos(4\theta) \right\} r^{\zeta_2^{(2)}}, \end{aligned} \tag{4.3}$$

with the function κ determined by axisymmetry

$$\kappa(d_1, d_2, \zeta_2^{(2)}) = \frac{\left[2 - \zeta_2^{(2)}\right]\left[\zeta_2^{(2)} d_1 + \left(4 + \zeta_2^{(2)}\right) d_2\right]}{\left[\zeta_2^{(2)} + 7 + \sqrt{17}\right]\left[\zeta_2^{(2)} + 7 - \sqrt{17}\right]}.$$

In the case of shear turbulence, the velocity gradient points in the $y-$direction. In this case we have the reflection symmetry $G_{xx}(r, \theta, \phi) = G_{xx}(r, \theta, \pi - \phi)$. At $\phi = 0$ the special symmetry $G_{xx}(r, \theta, \phi = 0) = G_{xx}(r, \pi - \theta, \phi = 0)$ leads the following expression for the anisotropic contribution

$$g_2(\theta) = d_1 + d_2 \cos(2\theta) + d_3 \cos(4\theta), \tag{4.4}$$

where the parameters $d_{1,2}$ are different from the parameters with the same name in Eq. 4.3. The loss of axisymmetry results in an extra free parameter d_3. At azimuthal angles away from $\phi = 0$, the anisotropic contribution acquires another free parameter and becomes

$$\begin{aligned} g_2(\theta) &= d_1 + d_2 \cos(2\theta) + d_3 \cos(4\theta) \\ &+ d_4 \left[\left(12 + 2\zeta_2^{(2)}\right) \sin(2\theta) + \left(2 - \zeta_2^{(2)}\right) \sin(4\theta)\right], \end{aligned} \tag{4.5}$$

whereas the $\phi-$ dependence is given by

$$g_2(\phi) = d_5 + d_6 \cos(2\phi), \tag{4.6}$$

where in Eqs. 4.5,4.6 the parameters $d_{1,2,3}$ are different from the parameters with the same name in earlier expressions. Because Eqs. 4.5 and 4.6 involve disjunct sets of parameters, it is not possible to reconstruct the $\phi-$dependence of g_2 at a given angle θ from its θ dependence at a given ϕ. The expressions Eqs. 4.4 and 4.5 are completely equivalent to those in [50], but we point out that Eq. 13 of [50] is in error because it contains a redundant fit parameter.

Summarizing, in case of axisymmetric turbulence there are 5 adjustable parameters: two exponents $\zeta_2^{(0)}$ and $\zeta_2^{(2)}$ and 3 constants c_0, d_1, d_2. For shear turbulence there is an extra constant at $\phi = 0$ and a total of 7 adjustable parameters for other azimuthal angles. The art is to determine these parameters by fitting one of the equations to an experimentally measured structure function.

Rather than finding the best (in a least squares sense) set of parameters, which is a daunting task in 7-dimensional parameter space, we looked for the set of non-universal parameters $c_0, d_1, \ldots$ that gave a best fit for given values of the universal exponents $\zeta_2^{(0)}$ and $\zeta_2^{(2)}$. First, the value of the isotropic exponent $\zeta_2^{(0)}$ was guessed, for example from the transverse structure function G_2^T. Next, the anisotropy exponent $\zeta_2^{(2)}$ was scanned over a range of values. At each $\zeta_2^{(2)}$ we then

sought for the non-universal constants $c_0, d_1, \ldots$ which minimized the sum of squared differences χ^2 between measurement and fit. The value of this minimum depends on $\zeta_2^{(2)}$, and at some $\zeta_2^{(2)}$ it will be smallest. This distinction between universal and non-universal parameters was inspired by [5, 50] who followed the same procedure.

The key question then is if the anisotropy description of measured structure functions enables to detect the influence of large-scale anisotropy on the shape of the structure function, as characterized by its scaling exponent $\zeta_2^{(2)}$. From dimensional arguments [54] we expect $\zeta_2^{(2)} = 4/3$, but the precise value may be influenced by intermittency. Finding $\zeta_2^{(2)}$ is a highly non-trivial problem, as the influence of anisotropy is embodied in a mixture of isotropic and anisotropic contributions in Eq. 4.2 and it may be very difficult to unravel these contributions.

An alternative approach to detect large-scale anisotropy is to measure correlations of the velocity field that vanish exactly in the isotropic case; these correlations are then determined by anisotropy alone. For second-order correlations this is the mixed structure function $G_{\alpha\beta}$, with $\alpha \neq \beta$. This property was used in the analysis of a turbulent boundary layer in [51]. Although such a flow is not only anisotropic but also highly non-homogeneous, [51] found an anisotropic scaling exponent $\zeta_2^{(2)} \approx 1.21$, which is close to the dimensional estimate $\zeta_2^{(2)} = 4/3$.

In this paper we will analyze experiments involving two turbulent flows with decreasing symmetry. In the first case the flow has axisymmetry, in the second case we consider homogeneous shear turbulence. In both cases turbulence was created in a windtunnel using special grids. These grids were designed to preserve the homogeneity of the flow: the SO(3) description deals with *homogeneous* anisotropic flows. This severe constraint limited the Reynolds number to $R_\lambda \approx 600$. The flow parameters are listed in Table 4.1.

In the next two sections we will describe the two experiments and the analysis of second–order structure functions using the SO(3) formulas Eq. 4.3,4.4,4.5,4.6. We will then consider the angle dependence of order 3 and 7 structure functions in homogeneous shear turbulence. Finally we will discuss in Appendix 4.6 other second–order quantities that may be used to quantify anisotropy.

4.2 Axisymmetric turbulence

In view of te SO(3) picture, it is attractive to study axisymmetric turbulence as it involves the simplest expression for the angle-dependent structure functions with the smallest number of adjustable parameters. The experimental setup is sketched in Fig. 4.3 and the flow characteristics are summarized in Table 4.1. Axisymmetric turbulence is generated in the wake of a circularly symmetric target-

Configuration	U (m/s)	$u_{\rm rms}$ (m/s)	Re_λ	η (m)	L (m)
1	10.6	1.14	560	1.6×10^{-4}	0.17
2	11.4	1.15	600	1.6×10^{-4}	0.19

Tab. 4.1: *Characteristic parameters of the used turbulent flows, (1): axisymmetric turbulence, (2) homogeneous shear turbulence. The mean velocity is U with $u_{\rm rms} = \langle u^2 \rangle^{1/2}$ the r.m.s. size of the fluctuations. For the definition of the other characteristic quantities the r.m.s. derivative velocity $\dot{u}_{\rm rms} \equiv \langle (\mathrm{d}u/\mathrm{d}t)^2 \rangle^{1/2}$ is used. For the mean energy dissipation ϵ the isotropic value is taken $\epsilon = 15\,\nu \dot{u}_{\rm rms}^2\, U^{-2}$ with ν the kinematic viscosity. The Kolmogorov scale is $\eta = (\nu^3/\epsilon)^{1/4}$ and the Taylor microscale is $\lambda = U u_{\rm rms}/\dot{u}_{\rm rms}$ with the associated Reynolds number $Re_\lambda = \lambda u_{\rm rms}/\nu$. The integral length scale is defined in terms of the correlation function of velocity fluctuations $L = \int_0^\infty \langle u(x)u(x+r)\rangle_x \mathrm{d}r / \langle u^2 \rangle$.*

shaped grid placed in a recirculating windtunnel. Velocity fluctuations $u(y)$ were measured 2 m downstream using an array of hot-wire sensors. By time-delaying the signals from the wires, the $\theta-$ dependence of structure functions can be measured. By rotating the entire array along the $x-$axis, the angle ϕ was changed. It was verified that all results were independent of ϕ, thus proving the axisymmetry of the flow.

Figure 4.4 shows the second-order transverse and longitudinal structure functions which exhibit clear scaling behavior. Let us recall that the transverse structure function G_2^T is measured using the discrete distances between probe pairs in the array. The position of the 10 probes (sensitive length 200 μm), was chosen such as to space the 45 distances between them as close as possible to exponential. Each point of the transverse structure function in Fig. 4.4, therefore, corresponds to a distance $r = y_i - y_j$ between different probe pairs that are at different locations y_i, y_j. It is seen that the curves are smooth, with the scaling genuinely in the separation r, which proves the homogeneity of the flow. Further evidence of this homogeneity is provided by the frequency spectra $E(f, y_i)$ at each probe position y_i shown in Fig. 4.5, which are observed to be virtually independent of y. We conclude that our flow is axisymmetric and homogeneous, so that the simplest SO(3) decomposition formula Eq. 4.3 applies which has only 3 adjustable non-universal constants.

An idea of the anisotropy of our flow can be gathered from the measured longitudinal and transverse structure functions. In the isotropic case the function

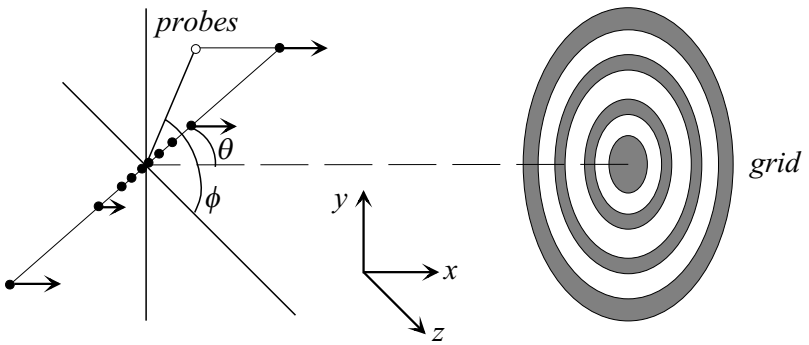

Fig. 4.3: *Axisymmetric turbulence is generated with a target-shaped grid. The orientation of the vector r over which velocity increments are measured is determined by the angles θ and ϕ. The azimuthal angle ϕ is varied by physically rotating the probe array; the polar angle θ is adjusted by varying the time delay between samples as is illustrated in Fig. 4.1. The mean velocity of the flow is $U = 10.6\ \mathrm{ms}^{-1}$, the r.m.s. fluctuating velocity $u = 1.14\ \mathrm{ms}^{-1}$, the Reynolds number $Re_\lambda = 560$, and the Kolmogorov scale $\eta = 1.6 \times 10^{-4}\ \mathrm{m}$. The grid is not drawn to scale.*

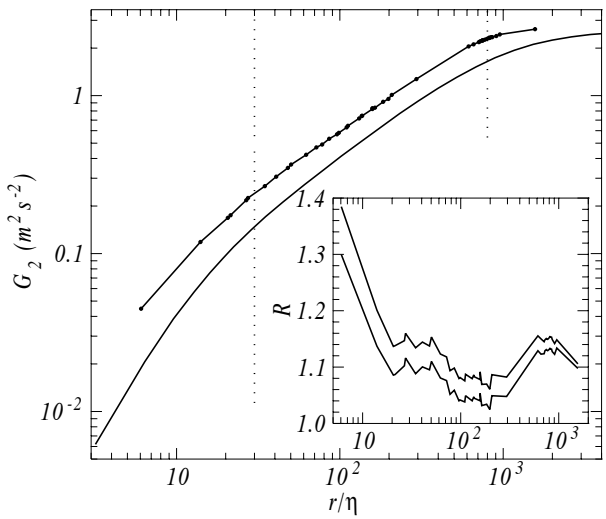

Fig. 4.4: *Longitudinal and transverse structure functions in axisymmetric turbulence. Dots connected by lines: transverse $G_2^T(r)$, line: longitudinal $G_2^L(r)$. The dotted lines indicate the extent of the inertial range. Inset: anisotropy ratio $R(r)$ computed from the longitudinal and transverse structure functions according to Eq. 4.7. The lower curves assumed the mean velocity as the convection velocity in the Taylor frozen turbulence hypothesis; the upper curve follows the definition of [50].*

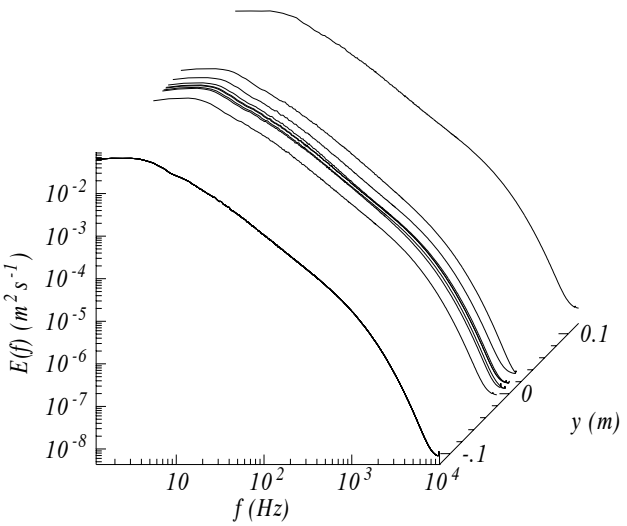

Fig. 4.5: *Energy spectra of all 10 probes of the probe array, which spans a separation of 0.24 m.*

$R(r)$,

$$R(r) \equiv G_2^T(r) / \left\{ G_2^L + \frac{r}{2} \frac{\mathrm{d}G_2^L}{\mathrm{d}r} \right\} \tag{4.7}$$

should be identically equal to 1. It can also be accidentally 1 in the anisotropic axisymmetric case, but only if a very special relation exists between the parameters $\zeta_2^{(0)}, \zeta_2^{(2)}, c_0, d_1$, and d_2 of Eq. 4.3, which we deem highly improbable. In our experimental setup $R(r)$ becomes trivially 1 at integral scales since both $G_2^T(r \to \infty) = G_2^L(r \to \infty) = 2\langle u^2 \rangle$. Therefore, $R(r)$ is only sensitive to anisotropy at inertial-range scales. As shown in the inset of Fig. 4.4, the anisotropy of our flow increases towards larger scales. The question now is if we can detect the influence of anisotropy at large scales with help of the SO(3) machinery Eq. 4.2, in particular whether we can recover the anisotropy scaling exponent $\zeta_2^{(2)} = 4/3$ from the behavior of $G_2(r, \theta)$ at large r. The inset of Fig. 4.4 shows that the anisotropy also increases at *small* scales. Clearly, an anisotropy description based on a hierarchy of scaling exponents cannot deal with this.

A point of discusion raised in [50] is whether the true spatial separations r in the transverse structure function G^T should be related to time-delayed separations $r = U\tau$ of the longitudinal G_2^L using the mean velocity U as the frozen turbulence convection velocity. For their atmospheric boundary layer flow they instead proposed to take $(U^2 + (3u)^2)^{1/2}$ as convection velocity. Because their fluctuation velocity was large ($u/U \approx 0.25$), it raised the convection velocity by 25%. In our case $u/U \approx 0.1$, and as the inset of Fig. 4.4 shows, the effect on the

measured anisotropy is small.

First, we measured the angle dependence of G_2 using only 2 probes spaced at $r_0/\eta = 100$, which is centered in the inertial range $r/\eta \in [30, 800]$. The experiment and fit of Eq. 4.3 are shown in Fig. 4.6a. For the fit, we fixed $\zeta_2^{(0)}$ and determined the constants c_0, d_1, d_2 and the exponent $\zeta_2^{(2)}$ in a least squares procedure. The exponent $\zeta_2^{(0)}$ varies from $\zeta_2^{(0)} = 0.70$ to $\zeta_2^{(0)} \approx 0.74$ for the transverse and longitudinal case, respectively. We select $\zeta_2^{(0)} = 0.72$, and discuss the influence of this particular choice below. Strikingly, the isotropic contribution $r^{\zeta_2^{(0)}} g_0(\theta)$ alone does not provide a satisfying fit, and it is necessary to include the anisotropic contribution. We find that the best fit is reached if $\zeta_2^{(2)} = 1.5$, which is close to the value $4/3$ following from dimensional arguments. The almost perfect fit corresponds to a well-defined minimum of the sum of squared differences χ^2 as shown in Fig. 4.6b where we detemined the minimum squared error over a range of $\zeta_2^{(2)}$. As we do not have an independent estimate of the error of measured structure functions, we normalize the minimum χ^2 to 1 by multiplication with an appropriate factor.

These findings completely agree with those of [5, 50] who followed a similar procedure in the atmospheric boundary layer and concluded $\zeta_2^{(2)} = 1.39$. However, repeating the experiment with different probe separations r_0 confuses the issue. As Fig. 4.6b illustrates, the value of $\zeta_2^{(2)}$ that optimizes the fit depends strongly on r_0; it is unphysically large at small r_0 and small for large r_0, with both values of r_0 in the inertial range. However, the value $r_0/\eta = 100$ is preferred as it provides the best defined minimum. Such a preference can perhaps be justified by the observation that the angle θ varies most rapidly near $r = r_0$, so that r_0 needs to be chosen well inside the inertial range. On the other hand, the dependence of the result on r_0 gravely complicates the application of the SO(3) machinery.

The information obtained on the θ dependence of the structure function is greatly enhanced if the number of velocity probes is made large enough such that structure functions at $\theta = 90^\circ$ can be made of pure spatial separations. Measured structure functions $G_2(r, \theta)$ for the pure longitudinal arrangement $\theta = 0$, using time delays only, for $\theta = 15^\circ, 35^\circ, 55^\circ$, using a combination of space- and time delays, and for the transverse arrangement are shown in Fig. 4.7. To more clearly expose the quality of the fits, we plot the structure functions compensated by the expected self–similar behavior $G_2(r, \theta)/r^{2/3}$. This procedure amplifies the noise in the $\theta > 0$ multiprobe structure functions which is caused by slight differences in probe characteristics. Because the longitudinal structure function at $\theta = 0$ is made from time delays only, this curve is smooth. However, the consistency between the single–probe and multiprobe measurements shows in the closeness of the curves at $\theta = 0$ and $\theta = 15^\circ$.

We have attempted to simultaneously fit the measured structure functions at

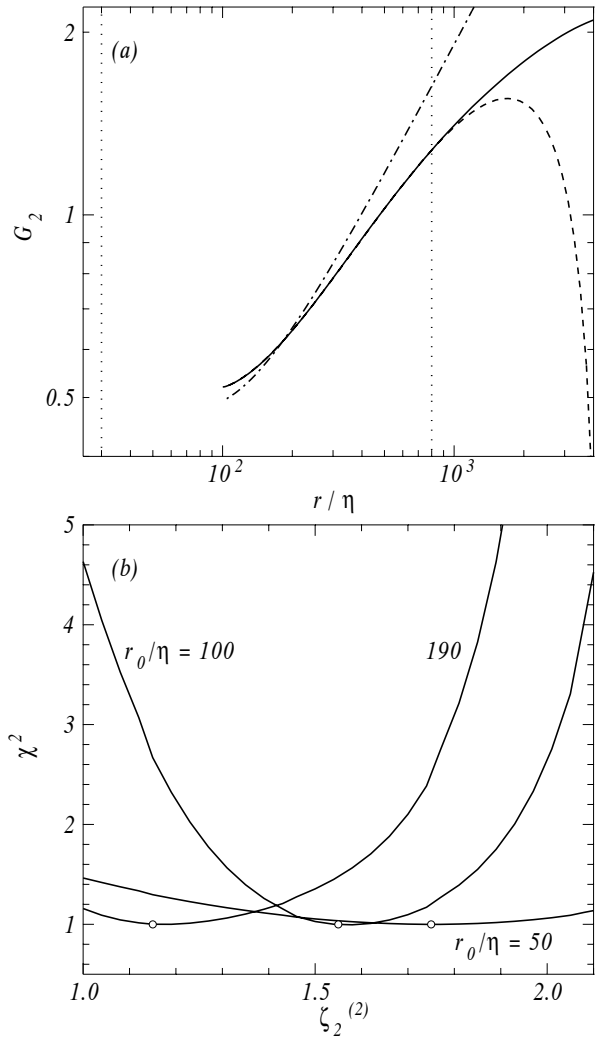

Fig. 4.6: *(a) Full line measured $G_2(r,\theta)$ using two probes separated at $r_0/\eta = 100$, so that $\theta(r) = \sin^{-1}(r_0/r)$. Dash-dotted line: fit that only includes isotropic part involving $g_0(\theta)$ (Eq. 4.3). Dashed line: fit including both isotropic and anisotropic part. Dotted lines: extent of inertial range. (b) Mimimum of sum of squared differences between measurement and fit for variation of the non-universal parameters c_0, d_1 and d_2 at $r_0/\eta = 50, 100$, and 190. The values of $\zeta_2^{(2)}$ that give the best fit are indicated by the open balls. The sum of squared diffences is normalized such that its minimum is always at $\chi^2 = 1$.*

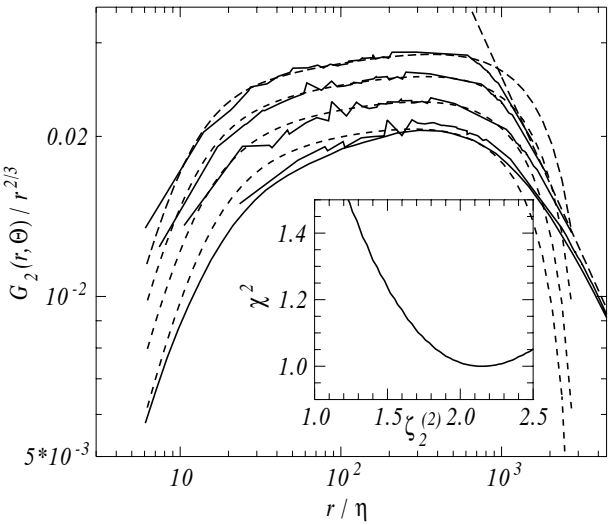

Fig. 4.7: *Full lines measured $r^{-2/3}\,G_2(r,\theta)$ at $\theta = 0, 15°, 35°, 55°$, and $90°$. Dashed lines: simultaneous fit of Eq. 4.3 to the data at $\theta = 0°, 35°, 55°$, and $90°$. The asymptote of the structure functions $2\langle u^2\rangle$ is indicated. Inset: mimimum of sum of squared differences between measurement and fit for variation of the non-universal parameters c_0, d_1 and d_2. A minimum is reached at $\zeta_2^{(2)} \approx 2.1$. The sum of squared differences is normalized such that its minimum is always at $\chi^2 = 1$.*

$\theta = 0°, 35°, 55°$, and $90°$ using Eq. 4.3 with a single set of parameters; the result is shown in Fig. 4.7. In correspondence with Fig. 4.6, the scales included in the fit ranged from $r/\eta = 100$ to values r where $G_2(r,\theta)$ have reached nearly their asymptotic value $\xi\, 2\langle u^2\rangle$, with $\xi = 0.9$. The small-r dissipative range behavior was modelled by replacing the isotropic part in Eq. 4.3 by

$$c_0 \left\{ h(r) + \sin^2(\theta)\, \frac{r}{2}\, \frac{\mathrm{d}h}{\mathrm{d}r} \right\}, \quad \text{with} \quad h(r) = r^2 \left(1 + (r/r_1)^2\right)^{(\zeta_2^{(0)}-2)/2}, \tag{4.8}$$

and $r_1/\eta = 12.6$. The function $h(r)$ [85] models the transition from dissipative scales, $h(r) \sim r^2$ to inertial range scales $h(r) \sim r^{\zeta_2^{(0)}}$. This choice improves the appearance of the fit, but it is completely inconsequental for our conclusions.

Also in this case, we find a poorly defined minimum of the sum of squared differences χ^2 at a value of the anisotropy exponent $\zeta_2^{(2)} \approx 2.1$ which is much larger than the dimensional prediction $\zeta_2^{(2)} = 4/3$. Another grave problem is that the position of the minimum strongly depends on the assumed value of $\zeta_2^{(0)}$, it varies from $\zeta_2^{(2)} = 2.5$ at $\zeta_2^{(0)} = 0.70$ to $\zeta_2^{(2)} = 2.0$ at $\zeta_2^{(0)} = 0.74$.

Naturally, the SO(3) description cannot deal with the small-scale anisotropy (shown in Fig. 4.4), but what is more troublesome, it also fails to represent the

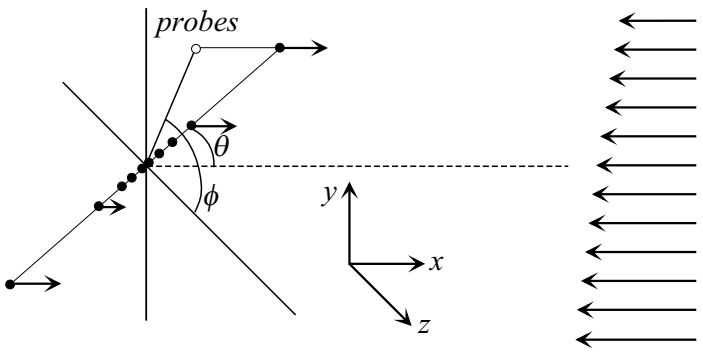

Fig. 4.8: *Homogeneous shear is generated using a grid with variable solidity. The mean velocity increases in the $y-$direction, but is does not vary with z. The (effective) orientation of the probe array is determined by the angles θ and ϕ.*

large-r behavior of the longitudinal structure function at $\theta = 0$. Trivially, all second–order structure functions reach at large r the asymptote $G_2(r,\theta) \to 2\langle u^2 \rangle$; this asymptote is also shown in Fig. 4.7. The SO(3) description applies to the $r-$dependence of the structure function *before* this asymptote is reached, a dependence which may depend on the angle. This is a subtle point because we always find $g_2(\theta) < 0$, which may also represent the trivial rise to saturation of the structure function. We conclude that more experimental information confuses the application of the SO(3) description. Contrary to Fig. 4.6, it is not longer obvious that the anisotropy of the structure function is described by the anisotropy value of $\zeta_2^{(2)}$.

4.3 Shear turbulence

While the anisotropy of the axisymmetric turbulence of Sec. 4.2 may be modest, a much stronger angle dependence was created in homogeneous shear turbulence. Homogeneous shear turbulence has a linear variation of the mean flow velocity U in the shear direction, a constant fluctuation velocity u, and an energy spectrum that does not depend on y. It is the simplest possible anisotropic turbulent flow, whose large-scale anisotropy is characterized by a single number: the shear rate $S = \mathrm{d}U/\mathrm{d}y$. Whilst the anisotropy is stronger, the SO(3) description now also has more adjustable parameters due to the loss of symmetry.

We produce homogeneous shear turbulence in a 0.9×0.7 m^2 cross section recirculating windtunnel with a maximal Reynolds number $Re_\lambda = 630$. To generate a uniform mean velocity gradient we use a novel grid whose $y-$dependent solidity is tuned to preserve a constant turbulence intensity u throughout most

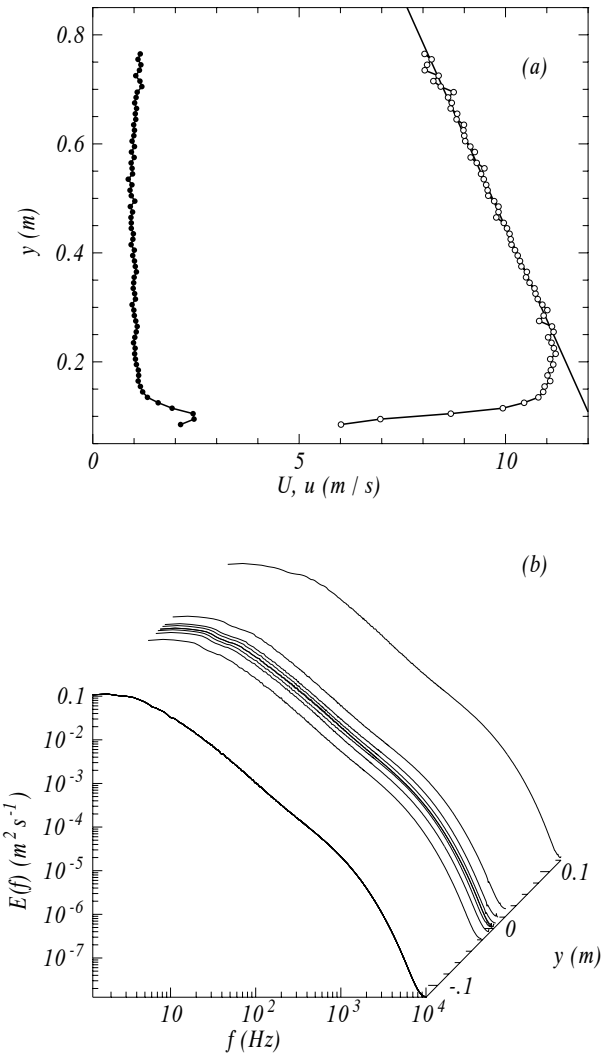

Fig. 4.9: *Homogeneous shear turbulence. (a) Open circles: mean velocity U, closed dots: rms fluctuations u at $x/H = 5.1$ behind the shear generating grid, where $H = 0.9$ m is the height of the tunnel. Near the lower wall the turbulent boundary layer marks the end of the homogeneous shear region. The Reynolds number is $Re_\lambda = 600$, and the shear strength $\mathrm{d}U/\mathrm{d}y = 5.95\ \mathrm{s}^{-1}$. (b) Variation of the spectra over the extent (0.24 m) of the probe array.*

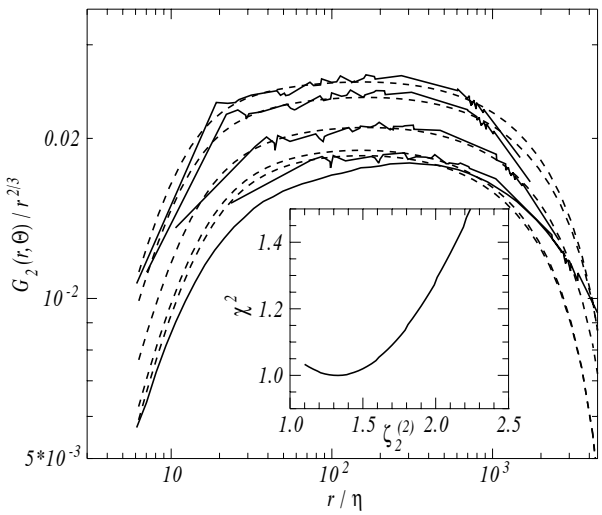

Fig. 4.10: *Full lines measured* $r^{-2/3}\, G_2(r,\theta)$ *at* $\theta = 0, 15°, 35°, 50°,$ *and* $90°$. *Dashed lines: simultaneaous fit of Eq. 4.5 to the data at* $\theta = 0°, 15°, 35°, 50°,$ *and* $90°$. *The asymptote of the structure functions* $2\langle u^2\rangle$ *is indicated. Inset: mimimum of sum of squared differences between measurement and fit for variation of the non-universal parameters* c_0, d_1 *and* d_2. *A minimum is reached at* $\zeta_2^{(2)} \approx 1.3$. *The sum of squared differences is normalized such that its minimum is always at* $\chi^2 = 1$.

of the windtunnel height. The experimental arrangement is sketched in Fig. 4.8. With the mean flow $U(y)$ in the $x-$direction, the shear points in the transverse y direction. The challenge of the experiment is to maintain the homogeneity of the flow: the SO(3) theory Eq. 4.2 describes anisotropy but presupposes homogeneity. That this challenge is met in our experiments is illustrated in Fig. 4.9a which shows the variation of the mean flow and the turbulence intensity with y. It is seen that the mean velocity profile is linear, with a small variation of the turbulence intensity over the probe array. Further evidence of homogeneity is provided by Fig. 4.9b which shows that the energy spectra, and thus all second-order quantities, such as the integral scale L, do not vary significantly with y. In this flow, the structure function depends both on θ and ϕ, and we measured first the θ dependence at $\phi = \pi/2$. Due to the absence of both axisymmetry and the special $\theta-$symmetry at $\phi = 0$, the general expression Eq. 4.5 has to be used with 5 non-universal parameters. The result of a fit of this formula to the measured structure function, using a single set of parameters, is shown in Fig. 4.10. In comparison to the case of axisymmetric turbulence, (Fig. 4.7), the larger num-

ber of parameters gives a better fit at angles θ close to the transverse $\pi/2$, but in both cases angles close to the longitudinal ones $\theta = 0$ are not represented well by the fit. Surprisingly, the best fit now occurs at $\zeta_2^{(2)} \approx 1.3$ which is very close to the dimensional prediction $\zeta_2^{(2)} = 4/3$. Contrary to the axisymmetric flow, the assumed value of $\zeta_2^{(0)}$ now hardly affects the mimimum $\zeta_2^{(2)}$.

At this point it is useful to evaluate the $\theta-$ measurements in the two flow configurations. We do that by plotting in Fig. 4.11 the anisotropic contribution $|g_2(\theta)|\, r^{\zeta_2^{(2)}-2/3}$ in the two cases. We see that for the axisymmetric experiment the anisotropic part has almost no angular dependence which makes it hard to find the exponent $\zeta_2^{(2)}$ from angle-dependent structure functions. For shear turbulence, the anisotropic contribution is larger and shows a significant variation with the angle θ.

In the axisymmetric case we have verified that there is no $\phi-$dependence, as it may be expected. For shear turbulence, instead, a clear $\phi-$dependence is expected given the strong asymmetry of the flow. We therefore measured the structure function $G_2(r, \theta = \pi/2, \phi)$ as a function of ϕ by rotating the probe array. According to Eq. 4.6, the variation would be largest if the azimuthal angle is rotated from $\phi = 0$ (perpendicular to the shear) to $\phi = \pi/2$ (along the shear). Compensated structure functions $r^{-2/3}\, G_2(r, \theta = \pi/2, \phi)$ for these two angles are shown in Fig. 4.12.

Clearly, the variation of the structure functions with ϕ is very small. However, at large separations they differ significantly: at $\phi = \pi/2$, $G_2(r, \theta = \pi/2)$ seems to have a contribution with a different scaling exponent (and a negative sign). Although we cannot strictly compare the scale of the variation with θ in Fig. 4.11 with the scale of the variation with ϕ as the two experiments involve disjunct sets of parameters, the variation with ϕ seen in Fig. 4.12 is consistent with the variation of the anisotropic part seen in Fig. 4.11. Future experiments must verify that the ϕ variation is really as $\cos(2\phi)$.

Our attempt to describe the angle–dependent structure functions with help of the SO(3) machinery Eq. 4.2 has mixed success. In axisymmetric turbulence, which has the smallest number of adjustable parameters, it is not possible to unambiguously arrive at values of the anisotropy exponent $\zeta_2^{(2)}$ that are close to the dimensional prediction $\zeta_2^{(2)} = 4/3$. In shear turbulence we succeeded in finding a value close to $4/3$, however, the number of free parameters is rather large in this case.

4.4 Higher order structure functions

As was realized earlier [51], a better approach to quantify anisotropy may be to measure structure functions which have a zero isotropic contribution. Since we

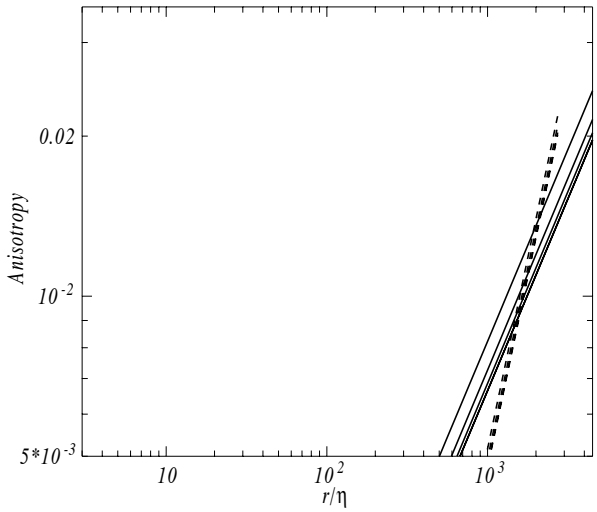

Fig. 4.11: *Full lines: anisotropic contribution $|g_2(\theta)|\, r^{\zeta_2^{(2)}-2/3}$ to the fits Fig. 4.10 which involves an experiment in shear turbulence. Dashed lines: the same but now for the fits of Fig. 4.7 that involves axisymmetric turbulence. The angles θ for the various lines are the same as in Figs. 4.10 and 4.7, respectively.*

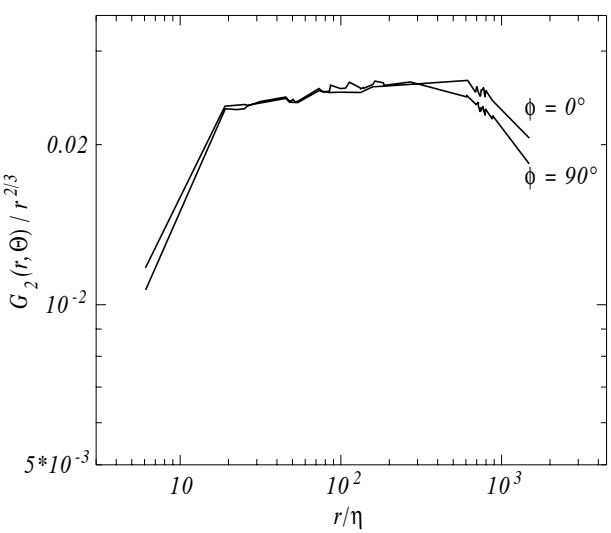

Fig. 4.12: *Azimuthal dependence of structure functions in shear turbulence. Full lines measured $r^{-2/3}\, G_2(r,\theta,\phi)$ at $\theta = \pi/2$ and $\phi = 0°$, and $90°$.*

measure a single velocity component, the lowest order tensorial quantity that does so is the third order structure function

$$G_{\alpha\alpha\alpha}(\boldsymbol{r}) \equiv \left\langle (u_\alpha(\boldsymbol{x}+\boldsymbol{r}) - u_\alpha(\boldsymbol{x}))^3 \right\rangle, \tag{4.9}$$

with $\alpha = x$ in our case. This tensor quantity can also be expanded in irreducible components.

$$G_{\alpha\alpha\alpha} = g_0^3(\theta)\, r + g_2^3(\theta,\phi)\, r^{\zeta_3^{(2)}} + \ldots, \tag{4.10}$$

where the superscript ^{3} on $g_{0,2}$ now indicates the order. However, whilst incompressibility of the velocity field reduces the number of unknown parameters of the anisotropic part of the *second order* structure function g_2^2 to just a few, no such reduction for g_2^3 is possible, unless the statistical properties of the driving force (the velocity-pressure correlations) are known. The well-known Kármán Howart-Kolmogorov equation fixes the isotropic component

$$g_0^3(\theta) = -\frac{4}{5}\,\epsilon\,\cos(\theta) \tag{4.11}$$

In the case of isotropic turbulence, a relation similar to Eq. 4.7 exists for the third-order angle dependent structure function $G_{xxx}(r,\theta)$ in terms of the longitudinal structure function $G_3^L(r) \equiv G_{xxx}(r,\theta=0)$,

$$G_{xxx}(r,\theta) = \tfrac{1}{2}\,\cos\theta\,\left\{\left(1+\cos^2(\theta)\right) G_3^L(r) + \sin^2(\theta)\, r\frac{\mathrm{d}}{\mathrm{d}r} G_3^L(r)\right\}. \tag{4.12}$$

In axisymmetric turbulence it follows from reflection symmetry that $G_{xxx} = 0$ at $\theta = \pi/2$, which trivially applies to the isotropic part Eq. 4.11, but also to the anisotropic part. Using multiprobe arrays, it is possible to measure G_{xxx} at small angles θ, but it poses extreme requirements on probe calibration as pairs of probes must now be sensitive to slight asymmetries between positive and negative velocity increments.

Figure 4.13 shows the longitudinal $G_3^L(r)$ which was measured using time delays and $G_{xxx}(r,\theta)$ at $\theta = 35^\circ$, together with the isotropic prediction Eq. 4.12. Clearly, it is not possible in axisymmetric turbulence to distinguish the measured curve at $\theta = 35^\circ$ from the isotropic prediction and it is therefore not possible to deduce information about an anisotropic contribution. Third-order transverse structure functions were also measured in [51] in (inhomogeneous) boundary layer turbulence. However, in this case the structure function was computed from the absolute values of the velocity increments $\langle|\Delta u|^3\rangle$, for which a decomposition Eq. 4.10 is very troublesome as it can never involve the proper isotropic part.

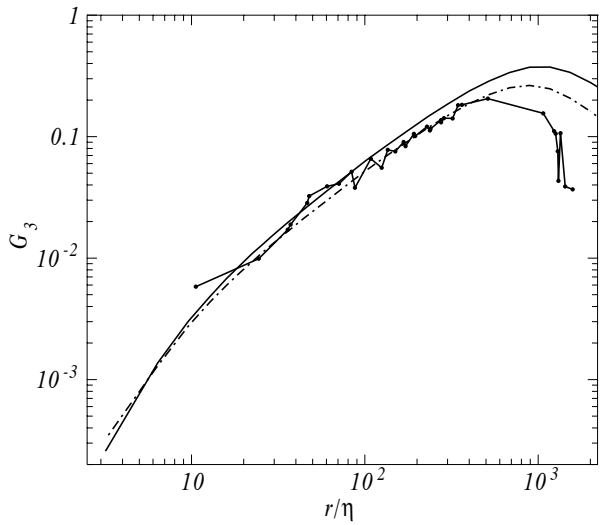

Fig. 4.13: *Third order structure function measured in axisymmetric turbulence. Full line: longitudinal structure function G_3^L at $\theta = 0$. Dots connected by lines, $G_{xxx}(r,\theta)$ at $\theta = 35°$, dash-dotted line: $G_{xxx}(r,\theta)$ computed from G_3^L using the isotropy relation Eq. 4.12.*

In shear turbulence, the reflection symmetry $\theta \leftrightarrow \pi - \theta$ is broken at $\phi \neq 0$ and the anisotropic part is not longer bound to vanish at $\theta = \pi/2$. Angle-dependent third–order structure functions are shown in Fig. 4.14a for angles $\phi = \pi/2$ and $\theta = 0$ (longitudinal), $\theta = 15°, \theta = 35°$, and $\theta = 60°$. In this case the isotropic contribution vanishes at $\theta = \pi/2$, and only the anisotropic contributions remain. If higher–order anisotropies with $l > 2$ are absent, the scaling at $\theta = \pi/2$ would be pure and the scaling at smaller angles would be a mixture. The scaling exponent at $\theta = \pi/2$ can then be identified with $\zeta_3^{(2)}$; we find $\zeta_3^{(2)} \approx 1.4$, which is significantly larger than the isotropic exponent $\zeta_3^{(0)} = 1$, and is rather close to the dimensional prediction $\zeta_3^{(2)} = 5/3$. If the SO(3) description applies, the scaling of the longitudinal structure function would be a mixture of both exponents

$$G_3^L = -\tfrac{4}{5}\epsilon\, r + b\, r^{\zeta_3^{(2)}}, \tag{4.13}$$

with $\zeta_3^{(2)} \approx 1.4$. Figure 4.14b illustrates that it is possible to find a constant $b > 0$ to describe the behavior of the longitudinal structure function at large scales. The dissipation rate ϵ in Eq. 4.13 was estimated from the longitudinal derivative, $\epsilon = 15\nu\langle(\partial u/\partial x)^2\rangle$, with ν the kinematic viscosity. The admixture of the anisotropic scaling in the longitudinal structure function G_3^L may explain why its apparent scaling exponent is smaller than 1, and why the apparent inertial

range of G_3^L is smaller than that of the transverse structure function at $\theta = \pi/2$. The anisotropic contribution to G_3^L is small and Eq. 4.13 can be used to obtain an impression of how the isotropic part decreases with increasing θ.

The parameter b in Eq. 4.13 is an unknown function of θ and ϕ which cannot be further specified using the SO(3) description. It can, however, in any case be concluded that $b(\theta, \phi = 0)$ must change sign between $\theta = 0$ and $\theta = \pi/2$. This implies that there is an intermediate angle where the scaling is pure isotropic, with scaling exponent 1. From Fig. 4.14a we estimate this *magic angle* θ_m to be $\theta_m \approx 15^\circ$.

The magnitude of the anisotropic contribution is much larger than what could have been anticipated on basis of the second-order structure function; it has, in fact, the same size as the isotropic part. This is quite disturbing as, within the framework of the SO(3) desciption, we expect the anisotropic contributions to be smaller than the isotropic ones.

In principle, low-order structure functions are affected by intermittency. This was already observed in the value of the scaling exponent $\zeta_2^{(2)}$ which in both flows significantly exceeds the self-similar value $2/3$. As intermittency effects are stronger for high orders, we show the angle dependence of $G_{7(x)}(r, \theta)$ in Fig. 4.15. Clear scaling can be observed at all angles with quite similar scaling exponents, that is, we are unable to distinguish a separate anisotropy exponent. The angle-dependent structure functions can be described well by the form $G_{7(x)}(r, \theta) \sim (0.9 + 5.2 \sin^2(\theta))\, r^{2.1}$. Although its order is higher, the noise in the 7th order structure function is smaller than that in the 3rd order one of Fig. 4.14. This allowed a fit of the functional form, where we emphasize the dependence on the *double* angle through $\sin^2(\theta)$. Elsewhere we will argue that high-order structure functions in homogeneous shear are determined strongly by intermittency. The relation between intermittency and anisotropy is an exciting and timely problem.

4.5 Summary and conclusion

The key idea of the SO(3) description is that the observed imprint of anisotropy due to stirring at large scales is dependent on the geometric arrangement of the measurement. At some angles, the effects of anisotropy are larger than at others. The expected angular dependence can be worked out in detail using the formalism of angular momentum theory.

In this paper we have described several experimental procedures to unfold structure functions using the irreducible representations of the rotation group. The conclusion of this work is that it is difficult to extract the anisotropic contribution from angle-dependent second–order structure functions. In the case of axisymmetric turbulence, the apparent success of a simple two–probe arrange-

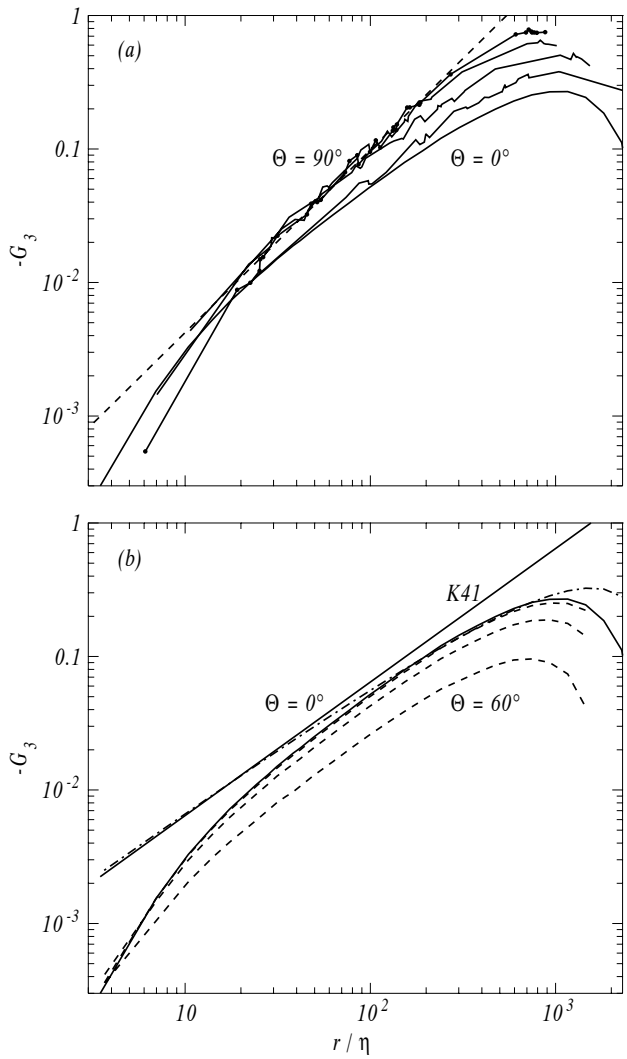

Fig. 4.14: *Third-order structure function measured in homogeneous shear turbulence. (a) Full lines:* $G_{xxx}(r,\theta)$ *at* $\theta = 0°$ *(longitudinal),* $\theta = 15°, \theta = 35°, \theta = 60°$*, and* $\theta = 90°$*. Dashed line, fit of* $G_{xxx}(r, \theta = 90°) \sim r^{\zeta_3^{(2)}}$*, with* $\zeta_3^{(2)} \approx 1.4$*. (b) Full line: third–order longitudinal structure function, dashed lines:* $G_{xxx}(r,\theta)$ *at* $\theta = 15°, \theta = 35°$*, and* $\theta = 60°$ *computed from the longitudinal one using Eq. 4.12. The Kolmogorov prediction* $G_{xxx}(r, \theta = 0) = \frac{4}{5}\epsilon\, r$ *is indicated by K41. Dash-dotted line: fit of Eq. 4.13.*

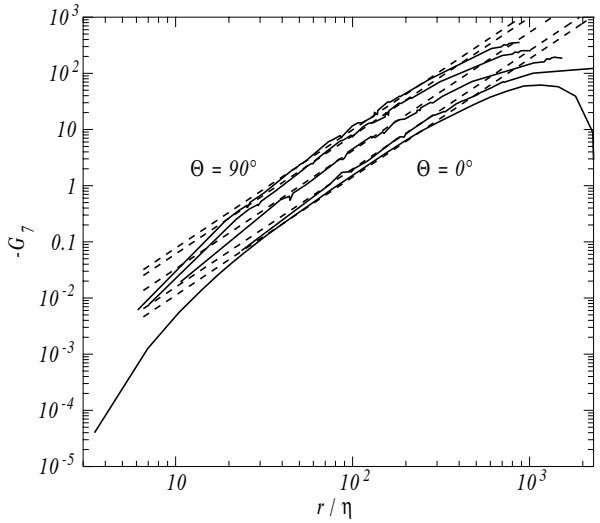

Fig. 4.15: *Order 7 structure function measured in homogeneous shear turbulence. Full lines:* $G_{7(x)}(r,\theta)$ *at* $\theta = 0°$ *(longitudinal),* $\theta = 15°, \theta = 35°, \theta = 60°$, *and* $\theta = 90°$. *Dashed lines fit of* $G_{7(x)}(r,\theta) \sim (0.9 + 5.2\,\sin^2(\theta))\, r^{2.1}$.

ment could not be reproduced when considering the information present in a multi–probe configuration; the SO(3) description simply does not work. On the other hand, this flow has a marked anisotropy as is shown in Fig. 4.4. At this point we disagree with the conclusions of [4, 50], who analyzed boundary-layer turbulence. The discrepancy may be explained by noticing that, while [4, 50] apply the axisymmetric formulae, boundary layer turbulence is not axisymmetric.

For the more strongly anisotropic shear turbulence the SO(3) machinery to analyze second-order structure functions seems to work, at least our data are consistent with the dimensional value of the anisotropic scaling exponent $\zeta_2^{(2)}$. However, the quality of the fit is poor and we do not exclude the possibility that the value found for the exponent is fortuitous. For example, we cannot completely rule out a small large-scale inhomogeneity. For this flow it was possible to isolate the anisotropic contribution in the third-order structure function, which turned out to be of the same order of magnitude as the isotropic part.

One could object that the anisotropy of the flows that are considered in this paper is small, and that consequently the anisotropy content of the structure functions is too small to be able to detect the anisotropy scaling exponent. While this may be so for the axisymmetric flow, this is definitely not the case for the homogeneous shear experiment where turbulence properties strongly depend on

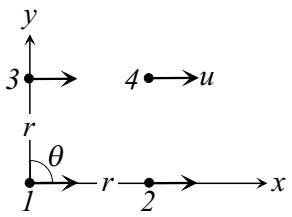

Fig. 4.16: *Setup for measuring mixed structure functions involving a single velocity component. True spatial separations in the $y-$dirction are combined with temporal delays in the $x-$direction to create a structure function that correlates velocity increments in the $x-$ and $y-$directions.*

the direction. In both experiments we strived for homogeneity of the flow, which compromised the achieved anisotropy. Better control of the turbulence, for example through active grids may help to create homogeneous flows that are more strongly anisotropic [81].

Aother objection may be that our Reynolds numbers are too small so that there is not a clear separation between inertial–range and integral scales. However, it is generally believed that precisely these moderate Reynolds numbers would benefit most of the SO(3) description. We emphasize that success of this approach was concluded in the case of direct numerical simulations which had a very small Reynold number [11].

We conclude that *perhaps* the SO(3) description is a way to quantify anisotropy in experiments on strong turbulence. Before we can decide the same success as in numerical simulations, more experiments are needed. These experiments must involve arrays of probes that can also measure several velocity components.

Acknowledgments

We gratefully acknowledge financial support by the "Nederlandse Organisatie voor Wetenschappelijk Onderzoek (NWO)" and "Stichting Fundamenteel Onderzoek der Materie (FOM)". We are indebted to Gerard Trines, Ad Holten and Gerald Oerlemans for technical assistance.

4.6 Appendix

4.6.1 Other anisotropy quantities

In our experimental setup we measure the $x-$component of the turbulent velocity. Using arrays of velocity sensors, the transverse structure functions $\langle(\Delta u)^p\rangle$

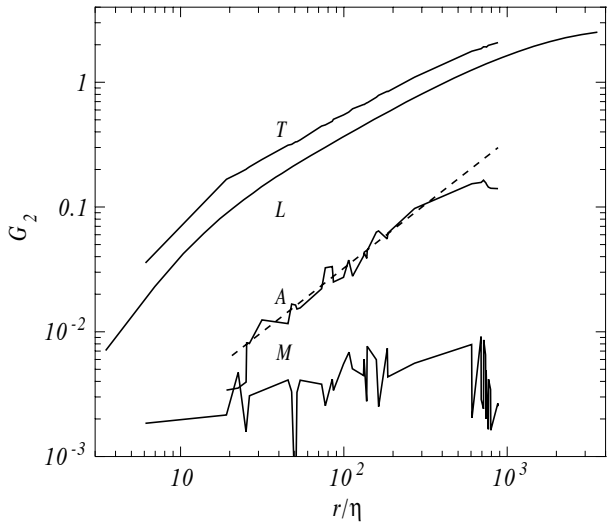

Fig. 4.17: *Second order structure functions in homogeneous shear turbulence. T: transverse, L: longitudinal, A: asymmetric according to Eq. 4.16, M: mixed, according to Eq. 4.19. Dashed line: fit of asymmetric structure function* $G_2^a(r) \sim r^{\zeta_2^a}$*, with* $\zeta_2^a \approx 1.02$.

are accessible. In homogeneous turbulence the lowest vanishing order is $p = 3$, which is therefore the lowest order that is exclusively determined by anisotropies. The question is if order-2 inertial-range quantities exist that vanish in the isotropic case and that are proportional to the shear rate S, and scale as $r^{4/3}$. Is so, we would be particularly interested in the SO(3) decomposition of these quantities.

Let us first recapitulate the simple symmetry arguments which apply to second-order structure functions. To that aim we consider

$$G_{\alpha\beta,\gamma}(r) \equiv \left\langle \left(u_\alpha(\boldsymbol{x}+r\boldsymbol{e}_\gamma) - u_\alpha(\boldsymbol{x})\right)\left(u_\beta(\boldsymbol{x}+r\boldsymbol{e}_\gamma) - u_\beta(\boldsymbol{x})\right)\right\rangle \tag{4.14}$$

If the turbulence is reflection symmetric, that is invariant under the operation $\mathcal{T}_\gamma : x_\gamma \to -x_\gamma$, it follows that

$$\mathcal{T}_\gamma\left[G_{\alpha\beta,\gamma}\right] = G_{\alpha\beta,\gamma}, \text{ while } \mathcal{T}_\alpha\left[G_{\alpha\beta,\gamma}\right] = -G_{\alpha\beta,\gamma}, \tag{4.15}$$

if $\alpha \neq \beta$. Therefore, in reflection symmetric turbulence, $G_{\alpha\beta,\gamma} = 0$ if $\alpha \neq \beta$, no matter γ.

A natural modification of Eq. 4.14 is the structure function

$$G_2^a(r) \equiv \left\langle \left|\left(u_\alpha(\boldsymbol{x}+r\boldsymbol{e}_\gamma) - u_\alpha(\boldsymbol{x})\right)\right|\left(u_\alpha(\boldsymbol{x}+r\boldsymbol{e}_\gamma) - u_\alpha(\boldsymbol{x})\right)\right\rangle, \tag{4.16}$$

which vanishes in isotropic turbulence for $\alpha \neq \gamma$ as it changes sign under the operation $\mathcal{T}_\gamma : x_\gamma \to -x_\gamma$. Another possibility is a second–order structure function

involving the *same* velocity component.

$$G^{\alpha\beta,\gamma}(r) \equiv \left\langle \left(u_\gamma(\boldsymbol{x}+r\boldsymbol{e}_\alpha) - u_\gamma(\boldsymbol{x})\right)\left(u_\gamma(\boldsymbol{x}+r\boldsymbol{e}_\beta) - u_\gamma(\boldsymbol{x})\right)\right\rangle \tag{4.17}$$

It is immediately obvious that

$$\mathcal{T}_\alpha\left[G^{\alpha\beta,\gamma}\right] = -G^{\alpha\beta,\gamma}, \tag{4.18}$$

unless $\alpha = \beta$. In our experiment we can make spatial separations in the $y-$direction and create spatial separations in the $x-$direction through time delays. When implementing Eq. 4.18, it is important to use velocity information in *four* points, as is sketched in Fig. 4.16

In particular, the implementation chosen here is

$$G^{xy,x}(r) = \langle((u_2-u_1)+(u_4-u_3))\,((u_3-u_1)+(u_4-u_2))\rangle\,. \tag{4.19}$$

We have verified that $G^{xy,x} = 0$ in turbulence which has $y-$reflection symmetry.

All these second-order structure functions have been measured in shear turbulence with the result shown in Fig. 4.17. The asymmetric structure function has the largest scaling exponent $\zeta_2^a \approx 1.02$, which falls significantly short of the dimensional prediction $4/3$, whereas the mixed structure function according to Eq. 4.19 has no scaling behavior at all. Clearly, more insight is needed to systematically construct low-order quantities that can capture anisotropy.

Chapter 5

SATURATION OF TRANSVERSE SCALING IN HOMOGENEOUS SHEAR TURBULENCE

Abstract

High Reynolds number homogeneous shear turbulence is created in a windtunnel using a novel design variable solidity grid. Transverse structure functions are measured using multiple hot-wire anemometry, both parallel and perpendicular to the shear direction. The scaling exponents of high order structure functions are found to saturate to an asymptotic value for very large moments. This novel property, analogous to the similar phenomenon in passive scalar turbulence, is shown to be caused by anisotropic flow structures at small scales. We find that the intermittent structures carrying the shear signature are mostly concentrated in the negative tail of the PDFs. In contrast to that, positive small-scale structures are similar to those encountered in homogeneous and isotropic turbulence. Finally, we focus on small-scale anisotropy investigations, either via the evolution of transverse skewness with Reynolds-number or by comparing the relative longitudinal versus transverse scaling properties of high-order structure functions.

5.1 Introduction

The central paradigm of Kolmogorov's turbulence is that local isotropy will be restored in the limit of very high Reynolds numbers. In the context of laboratory flows, where it is possible to create well-defined turbulence which has a mean shear, the belief is, therefore, that the large scale mean shear will be forgotten at the smallest scales.

The concept of homogeneous shear turbulence was first introduced by von Kármán (1937). The flow is characterized by a constant turbulence intensity $\langle u^2 \rangle^{1/2}$ and a constant mean flow gradient. This type of flow, despite its relatively simple form, proves to be very difficult to achieve experimentally. Serious efforts of generating homogeneous shear flows seem to begin with the experiment of Rose (1965 [76]) in the laboratory of Prof. Stanley Corrsin, stimulated by the assistance of Genevieve Comte-Bellot, and was initially meant to provide a quick

look at properties of turbulence associated with a uniform shear. He succeeded in generating a linear mean velocity profile and could draw a few important conclusions: the flow, despite a very moderate Reynolds number, was characterized by a uniform turbulence intensity and a shear stress approaching an asymptotic value. Rose was not completely satisfied with the presence of wall boundary layer growth and additional grid generated inhomogeneities, which manifested, for example, in variations of the integral scale profiles with in both spanwise and streamwise direction. This kind of effects frustrated his efforts in deriving additional conclusions, which was left to be solved by future investigations.

In 1969, Champagne *et al.* [28] continued the work of Rose and performed experiments that had as purpose the generation of a better approximation to homogeneous shear turbulence in the windtunnel. In their flow, the streamwise integral scale varied more slowly with the distance to the shear generator, while the Reynolds number was larger ($Re_\lambda = 130$). The anisotropy of the flow was studied for a wider range of scales by analyzing the cross-correlation spectrum. The local isotropy, despite of the small value of the Reynolds number, was found to be satisfactory and measured via the statistics of the streamwise derivative, through the quantity

$$\frac{\langle(\partial u/\partial x)(\partial u/\partial y)\rangle}{\langle(\partial u/\partial x)^2\rangle^{1/2}\langle(\partial u/\partial y)^2\rangle^{1/2}}, \tag{5.1}$$

which is nominally zero in the case of reflection symmetry in the y- (shear) direction. Instead, Champagne *et al.* found it to be 0.21. From now on we use a coordinate system in which x is pointing in the streamwise direction and y in the shear direction.

Pursuing this work, similar experiments were performed at higher mean shear rates by Harris *et al.* (1977 [42]), confirming the asymptotic state found previously, in which characteristic scales and turbulent energy grow monotonically further away from the stirrer. The increase in shear was accompanied by an increase in the turbulence intensities (up to 5%) and the Reynolds number was slightly improved, but the profiles of turbulence intensity showed an unavoidable growth of the spanwise inhomogeneity. Finally, Tavoularis and Karnik (1989 [88]) extended even further the shear rate and showed that given a sufficiently large shear constant $k_s = (1/U_c)(dU/dy)$, where U_c is the streamwise mean velocity in the center of the shear region and dU/dy is the slope of the linear mean velocity profile, the developed flows have a constant dissipation ϵ to production $\mathcal{P}$ ratio (smaller than 1), and exponentially growing shear stresses. The rate of growth of integral scales with downstream separation was related to the value of the parameter k_s, and it appeared that the regions where $\epsilon/\mathcal{P}$ approaches 1 have smaller k_s. Attempts to decrease its value by varying the structure

of the shear generator resulted in loss of homogeneity.

We can see at this point that for the experiments performed in this period, more attention has been paid to determination of the self-similar properties of homogeneous shear turbulence, rather than assessing the small-scale anisotropy of the flow. This issue was probably not addressed mainly because of the small Re_λ, however, it is important to mention that the generated sheared turbulence was remarkably homogeneous.

The quantity of choice for evaluating the anisotropy of the small scales is the skewness of the velocity derivative, taken in the direction of the shear, which is identically 0 in the case of an isotropic field. The skewness is defined as

$$K = \frac{\langle (\partial u/\partial y)^3 \rangle}{\langle (\partial u/\partial y)^2 \rangle^{3/2}}. \tag{5.2}$$

It takes a non-zero value for finite Reynolds number homogeneous shear flows, but it is expected to disappear for very large Re_λ. From simple dimensional arguments [53], the skewness should decrease like $K \simeq Re_\lambda^{-1}$. Tavoularis and Corrsin (1981) measured a skewness of 0.62 for a Reynolds number flow $Re_\lambda \sim 266$. Using essentially a similar setup, Garg and Warhaft (GW [37]) studied more recently the variation of skewness for a range of near-homogeneous shear flows with $156 \leq Re_\lambda \leq 390$ and found that the derivative skewness decreases with the Reynolds number, but slower than expected. Their efforts were continued by the improvement of the shear generator by means of an active stirrer, by Shen and Warhaft [81], who obtained a maximal Reynolds number ~ 1000. A characteristic of the actively stirred flows is the persistence of very large streamwise integral scales, which makes it difficult to compare this type of turbulence with the previous results. Their results, however, not only confirm the GW results, but show that the higher order derivative statistics, like hyper-skewness and generalizations thereof, seem to stop decreasing with the further increase of the Reynolds number.

A parallel experiment developed by Ferchichi and Tavoularis [31] confirms the decreasing trend of the derivative skewness, but this feature persists in the next order of the statistics, though the Reynolds numbers in these experiments are slightly lower.

These quite different results make the issue of anisotropy at dissipative scales an open question, although the parallel problem of scalar fields passively advected by the turbulent velocity field has been settled by numerical simulations in favor of violation of the local isotropy principle. The difference in the results by Shen and Warhaft [81] and Ferchichi and Tavoularis [31] has been blamed on the departure of the flow from homogeneous shear turbulence.

A simple dimensional argument predicts for the odd-order $p = 3, 5, 7, \ldots$

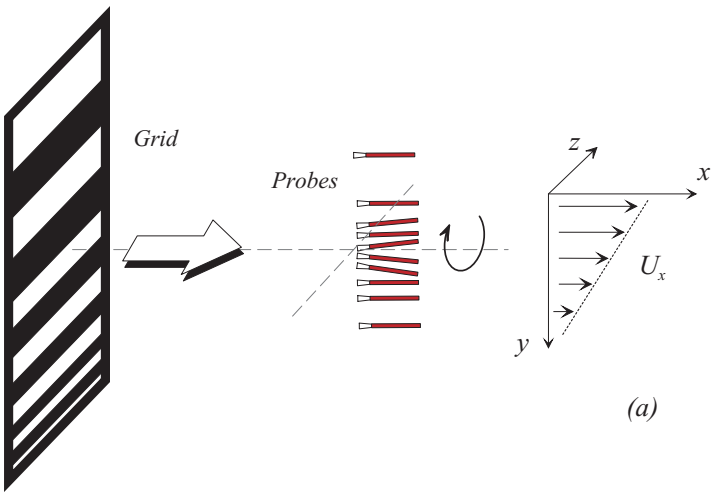

Fig. 5.1: *Sketch of the experimental setup: the variable solidity grid is a two-dimensional multiscale grid constructed such that both the filled and empty spaces gradually increase, but at different rates.*

structure functions the scaling exponents [53]

$$\zeta_p = \frac{p+2}{3}. \tag{5.3}$$

High-order structure functions in shear turbulence have recently been measured by Shen and Warhaft (2002) [82]. They find instead the same exponents as in isotropic turbulence.

In this chapter, we perform multiple hot-wire measurements of homogeneous shear flow in a windtunnel, in an attempt to thoroughly compare differences with respect to the already well-documented properties of near-isotropic and homogeneous high Reynolds number turbulence. Special attention is given to the quality of the flow, in order to strictly fulfill the requirements of homogeneous shear.

5.2 Experimental setup

Creating windtunnel homogeneous shear turbulence with high Reynolds number is a difficult task, especially when both a strong shear and good homogeneity are desired. Recent windtunnel setups achieved either a high Reynolds number combined with a moderate shear strength [81] or smaller Reynolds numbers with a stronger shear [31]. The typical deficiency in this type of flows is that instead of generating homogeneous shear, where the strength of the fluctuations $\langle u^2 \rangle$ is constant along the shear direction (or, ideally, independent of orientation), one

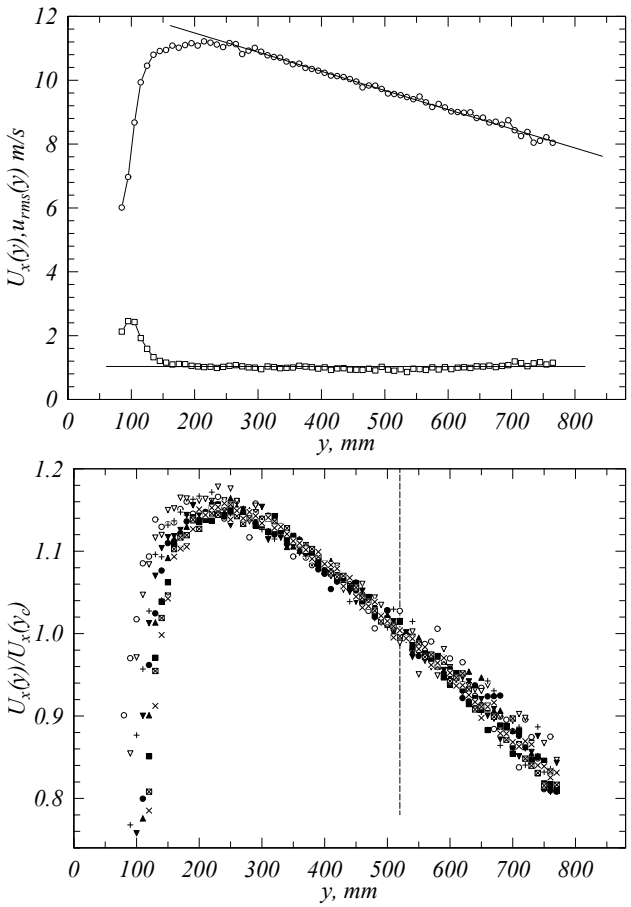

Fig. 5.2: *(a) Mean velocity profile along the vertical direction of the shear, measured in the center of the windtunnel. (b) Mean velocity profile of the shear for a set of 9 runs with Reynolds numbers between 150 and 600, normalized by the mean velocity in the center of the shear region U_c. For all the runs, the position which determines U_c is indicated by the dashed line.*

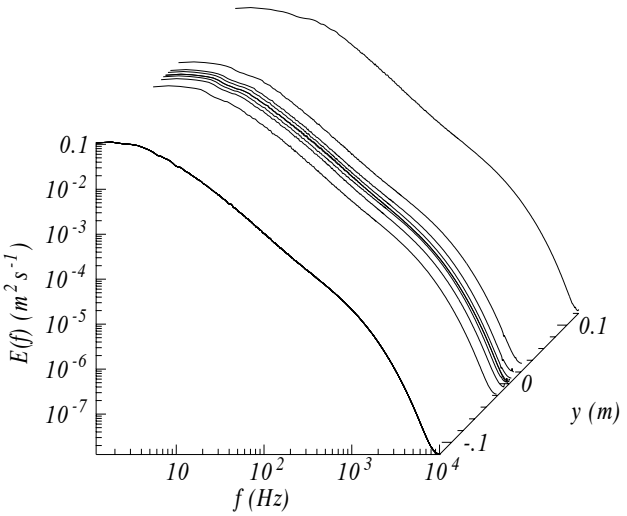

Fig. 5.3: *Longitudinal spectra obtained simultaneously at $Re_\lambda \approx 600$ with the probe array oriented in the shear direction (vertical). A similar figure is obtained when the array is perpendicular to the shear (horizontal). The homogeneity of the shear is reflected in identical spectra, we find thus identical integral scales over large span-wise areas of the flow.*

favors a regime called "uniformly sheared turbulence", with linear variation of $u_{\rm rms}$. We expect that this situation will affect the scaling properties of the flow such that it will be different from the ideal case where the shear rate is homogeneous.

In our experiments we generate shear that is very nearly homogeneous, but the shear rate is relatively small. Traditionally, shear turbulence is generated (far from walls) using progressive solidity screens that create different mean velocity layers, combined with means of increasing the turbulence intensity that use a passive or active grids. An active grid can almost double the Reynolds number in homogeneous and isotropic turbulence [81, 60]. Variable solidity passive grids originate in the pioneering work done more than 30 years ago by Champagne *et al.* [28]. A somewhat similar technique was used even earlier by Rose [76], who ingeniously used a succession of parallel rods of equal thickness at variable separation to create a highly homogeneous shear flow, but possessing a small Reynolds number.

We adapted this method and achieved a much higher Reynolds number by varying simultaneously the width of the solid areas and that of the transparent regions. A sketch of the grid is given in figure 5.1. Despite its simplicity, this type of grid provides a Taylor micro-scale-based Reynolds number ~ 600 on the cen-

terline, comparable to more sophisticated setups. The homogeneity of the shear is excellent, as can be seen from figure 5.2(a), which shows the mean and r.m.s. profiles of the longitudinal velocity component. By varying the mean velocity in the wind-tunnel, Re_λ could be varied from 150 to 600. The shear constant $k_s = (1/U_c)dU_x/dy$ (see [88]), where U_c is the longitudinal mean velocity in the center of the shear region, is remarkably uniform over the entire range, as can be inferred from figure 5.2(b). Since all the profiles have been recorded at a fixed separation $x/H = 5.1$ downstream from the grid, we can safely assume that the flow is also well-behaved in the streamwise x-direction. As further evidence for the homogeneity of the flow, we show in figure 5.3 the longitudinal spectra obtained from individual probes during a typical measurement. Although each probe sees a different mean velocity of the flow, the local energy spectra are identical.

Turbulent velocity fields and their increments were measured using multiple hot-wire anemometry. A single probe suffices to measure longitudinal velocity increments $\Delta u(\Delta\tau)$ by registering a time-dependent signal. By invoking Taylor's frozen turbulence hypothesis, temporal delays $\Delta\tau$ can be interpreted as spatial separations $\Delta x = U\Delta\tau$, with U the mean flow velocity.

Although a measurement at a single point can establish the scaling properties of the velocity field, more extended information is needed for characterizing anisotropy. In these experiments we use an array of probes oriented perpendicularly to the mean flow direction which samples the velocity field in many points simultaneously. It gives access to the transverse increments $\Delta u(y_i)$ of the fluctuating u-component at discrete separations $y_i - y_j$ ([93]). The advantage of this arrangement is that no recourse to Taylor's frozen turbulence theory is needed. If the turbulence intensity is small with respect to the mean velocity U, the probes are mainly sensitive to the $u-$component of the velocity, the admixture of the other transverse $v-$component being of order $u_{\rm rms}/U$.

The experiments were performed in the 0.7×0.9 m^2 experiment section of a recirculating windtunnel, 4.6 m downstream from the grid, where the turbulence intensity does not exceed 10% of the mean velocity. Each of the locally manufactured hot wires had a sensitive length of 200 μm, which is comparable to the smallest length scale of the flow (the measured Kolmogorov scale is $\eta = 180$ μm). They were operated at constant temperature using computerized anemometers that were also developed locally. The signals of the sensors were sampled exactly simultaneously at 20 kHz, after being low–pass filtered at 10 kHz. Whenever high-order statistics were desired, the total length of the recorded time-series per uninterrupted experimental run varied between 10^9 and 3×10^9 samples. A final measurement was performed with the sensor array oriented perpendicularly to the shear direction in order to verify the spanwise homogeneity of the flow at the

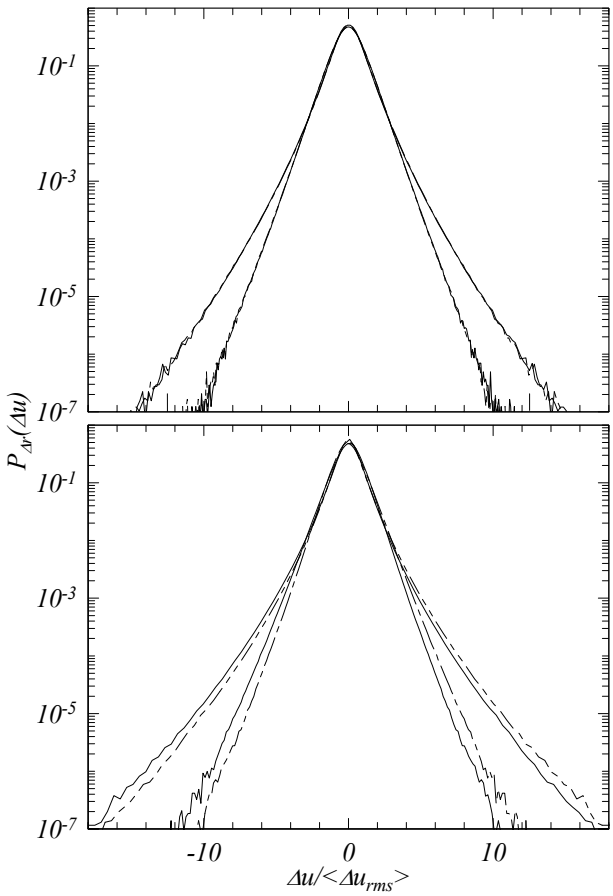

Fig. 5.4: *Probability densities of transverse increments of the longitudinal velocity component for $r/\eta \sim 6$ and $r/\eta \sim 45$ in (a) homogeneous and near-isotropic turbulence and (b) homogeneous shear turbulence. The full lines are $P(\Delta u)$, the dashed lines are $P(-\Delta u)$.*

highest Reynolds number.

5.3 Structure functions and saturation of transverse scaling exponents

The transverse structure functions of order p are defined as

$$S_p^T(r) =< (\Delta u^T(r))^p >= \langle [u(\boldsymbol{x} + r\boldsymbol{e}_y) - u(\boldsymbol{x})]^p \rangle, \tag{5.4}$$

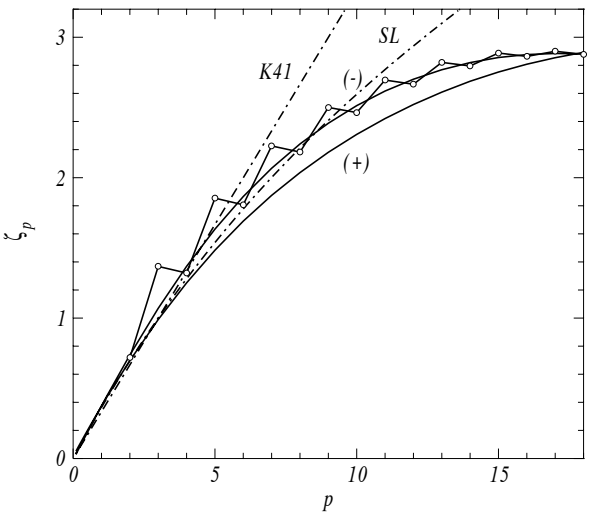

Fig. 5.5: *Dependence of the scaling exponents of the transverse structure functions on the order p; solid line, open circles: scaling exponents determined from the full PDF. There is a large asymmetry between odd and even moments. The smoothness of the curve is gradually restored with the increase of the order p, where the larger negative lobe of the probability distribution functions dominates the contribution to the structure function. The solid lines without markers depict the scaling exponents fitted to the left and right transverse structure functions, defined in Eqs. 5.13 and 5.12, while the dash-dotted lines are the She-Leveque (SL) and Kolmogorov (K41) predictions.*

equivalently they can be expressed in terms of the probability density functions of transverse velocity increments $\Delta u^T(r)$

$$S_p^T(r) =< (\Delta u^T(r))^p >= \int_{-\infty}^{\infty} (\Delta u^T)^p \mathcal{P}_r(\Delta u^T)\, \mathrm{d}\Delta u^T. \tag{5.5}$$

In the case of homogeneous turbulence, the odd-order moments S_{2p+1}^T vanish identically because of the reflection symmetry of the corresponding PDFs $\mathcal{P}_r(\Delta u) = \mathcal{P}_r(-\Delta u)$. This is no longer the case in shear turbulence. This is illustrated in figure 5.4, which compares PDFs measured in shear turbulence to those measured in homogeneous turbulence. The asymmetry in the case of shear turbulence, which is indicated by overlaying $\mathcal{P}(\Delta u)$ with $\mathcal{P}(-\Delta u)$ increases for increasing Δu. It is also seen that the PDFs of transverse increments in homogeneous turbulence are perfectly symmetric. Assuming that all odd-order moments are proportional to the shear rate $\mathcal{S} = dU/dy$ and further only depend on the dis-

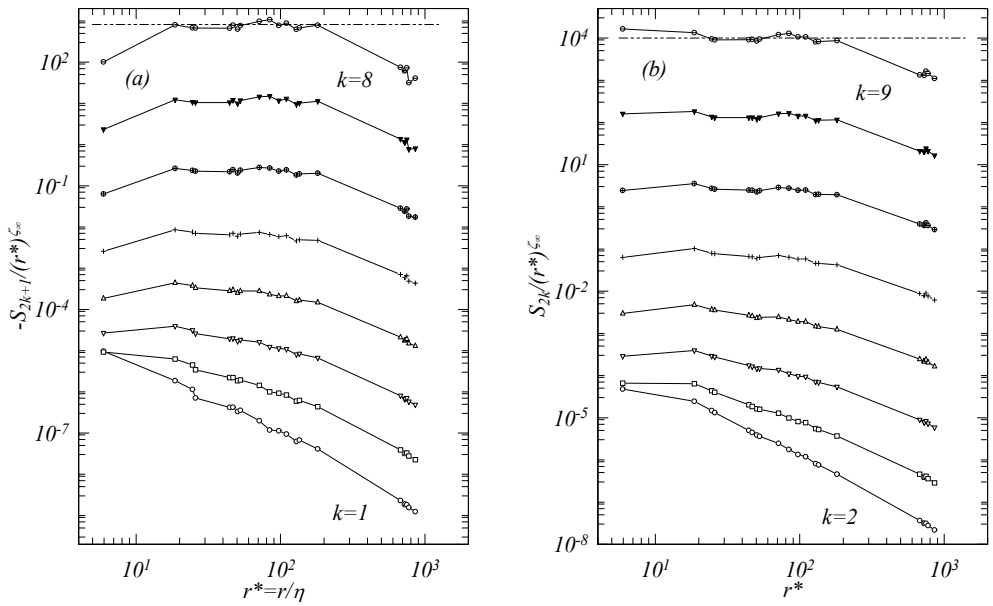

Fig. 5.6: *Transverse structure functions of (a) odd and (b) even orders. The normalization with the power law $(r/\eta)^{\zeta_\infty}$, with $\zeta_\infty = 3$, emphasizes the saturation tendency observed in the scaling exponents of the high-order structure functions.*

sipation rate $\langle\epsilon\rangle$ and the separation r, a dimensional argument predicts [53]

$$S_p(y) \sim \mathcal{S}\epsilon^{(p-1)/3} y^{(p+2)/3}. \tag{5.6}$$

We are interested to see if the odd moments will display a true scaling behaviour. Figure 5.6 shows the transverse structure functions of even orders and odd orders. Both of them show good scaling behaviour and have very little noise, although each separation $r = |y_i - y_j|$ involves a different pair of probes. They reflect a concentrated effort to calibrate for the static and dynamic anemometer response which may vary from one probe to another. All structure functions were computed from stretched-exponential representations of the PDFs. Given the high number of velocity samples for each PDF ($\sim 2 \times 10^8$), this implies that only very large orders ($p \gtrsim 12$) are influenced by this procedure. In this case, the only difference to the directly computed structure functions is that the noise level is reduced. A careful evaluation of this procedure is given in section 5.4. After fitting the curves to power laws over the inertial range, we extract their scaling exponents as a function of the order p.

Figures 5.5 and 5.6 suggest that above order $p = 15$, the scaling exponents saturate to a constant value ζ_∞. We believe we are the first to see this novel property of the velocity field in homogenous shear turbulence. It must be re-

alized, however, that large-order structure functions come with high statistical errors. Despite that, several independent experimental runs confirmed this property, and similar results were obtained from relative scaling exponents, where one structure function is plotted as function of another one (see section 3.3 of chapter 3). Another argument in favor of saturation of the scaling exponents that directly involves the PDFs will be presented in section 5.4.

Previously, a similar saturation property was found in passive scalar turbulence, either in experiments [29] or in numerical simulations [1], and related to the ramp-and-cliff characteristic shape of small-scale scalar increments. The scalar fronts are believed to be caused by underlying vorticity sheets (as predicted in [73]). The fluctuations of the scalar field are more intermittent than those of the velocity field. Therefore, the saturation of the scaling exponents of the scalar field occurs at smaller moments ($p \approx 10$) than for our velocity field, which facilitates its observation in an experiment.

Saturation of the scaling exponents can be readily understood in terms of the multifractal model by Frisch and Parisi [66]. The multifractal model provides a geometric explanation of the statistical properties of turbulent fluctuations. Briefly, it assumes that velocity increments scale *locally* as $\delta u(r) \sim r^h$, with local scaling exponents h that fluctuate throughout space. In turn, their fluctuations are also described by a scaling exponent such that the probability to encounter an exponent h at scale r depends on r as $r^{3-D(h)}$, where 3 is the dimension of the space and $D(h)$ is the fractal dimension of the set of exponents h. All averages, such as structure functions, can now be written as

$$S_p(r) = \int dh\, (r^h)^p\, r^{3-D(h)}. \tag{5.7}$$

Now assume that the velocity field consists of two types of events: regular events ("ramps") with $h = 1/3$, which fill the space $D(h) = 3$, and "cliffs", which are sharp at all (inertial) scales ($h = 0$) and have fractal dimension D_c. This simple bifractal field yields for the scaling exponent

$$S_p(r) \sim r_p^{\zeta}, \text{ with } \zeta_p = \min_h(p/3, 3 - D_c). \tag{5.8}$$

so that $\zeta_p = p/3,\ p < 3(3 - D_c)$ and $\zeta_p = 3 - D_c,\ p \geq 3(3 - D_c)$. If we assume that the "cliffs" of the velocity field have dimension 0, then we find a saturating dimension $\zeta_\infty = 3$, as we find experimentally.

Although this conclusion is tempting, it is also contradictory. The problem is that with a planar measurement (the probe array), it is not possible to capture point-like ($D_c = 0$) objects. Also, if the velocity jumps are the consequence of vortex sheets we expect $D_c = 1$ and $\zeta_\infty = 2$. We conclude that the multifractal model is ambiguous at this point. Within its realm, it is simply impossible to

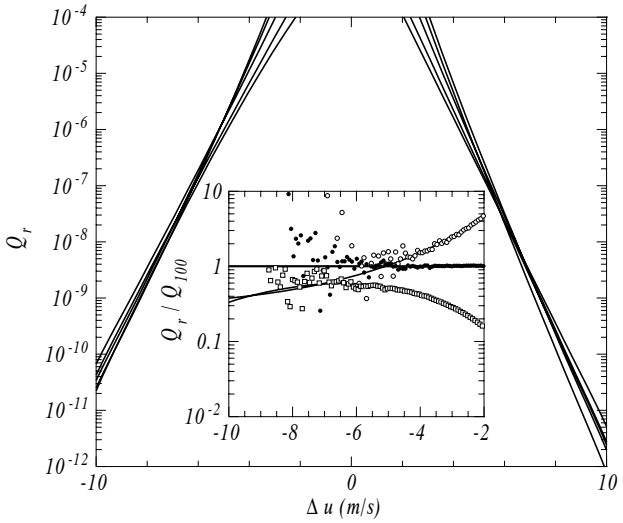

Fig. 5.7: *Full lines: the function* $Q_r(\Delta u) = (r/r_1)^{-\zeta_\infty} P_r(\Delta u)$*, with* r_1/η *= 30,* r/η *= 30, 50, 100, 190, 270, and* ζ_∞ *= 2.85. Inset: Full lines:* $Q_r(\Delta u)/Q_{r_0}(\Delta u)$*, with* r_0/η *= 100 with* r/η *taken in the inertial range,* r/η*= 30, 100, and 270, respectively. Symbols: experimental* $Q_r^e(\Delta u) = (r/r_0)^{-\zeta_\infty} P_r^e(\Delta u)/P_{r_0}(\Delta u)$*, for* r_0/η *= 100, and* r/η *= 30 (open circles),* r/η *= 100 (closed dots), and* r/η *= 270 (open squares), respectively.*

find $\zeta_\infty = 3$, unless we allow the occurrence of negative dimensions. Negative dimensions can be understood in the following naive example: the intersection in the 3-dimensional space of (random) lines with our planar ($D = 2$) measurements consists, generically, of points ($D_s = 0$). The intersection with objects "less than lines" ($D_c < 1$), therefore has dimension $D_s < 0$ [35].

Another theory that predicts saturation of the scaling behaviour is the instanton formalism, (*e.g.* described in [8]), which is used in the context of the Kraichnan passive scalar problem for dimensions $d \to \infty$. Similar predictions have been discussed for the three-dimensional scalar in [97, 20], which obtain saturation from instantonic bounds.

While the main concern of this chapter is in the behaviour of transverse properties of turbulence, it is interesting to mention that from our measurements of homogeneous shear turbulence, the directly available longitudinal structure functions do not indicate any deviation from the scaling exponents values measured in homogeneous and isotropic turbulence.

5.4 Convergence

We will now show that the saturation of high-order scaling exponents is consistent with the shape of the PDFs, thus corroborating our claim of saturation.

A sufficient but not necessary condition for saturation of the scaling exponents is that the function

$$Q_r(\Delta u) \equiv r^{-\zeta_\infty} P_r(\Delta u) \tag{5.9}$$

becomes independent of r for $|\Delta u| \to \infty$ [17] for $r-$values inside the inertial range.

The measured probability density functions $P_r(\Delta u)$ can be represented by stretched exponentials (see section 3.5 of chapter 3)

$$P_r(\Delta u) = a_r \mathrm{e}^{-\alpha_r |\Delta u|^{\beta_r}}. \tag{5.10}$$

Using the statistical tests devised in [93], we have found no significant differences between our measurements and Eq. (5.10), given the total number of velocity samples in our experiment. In terms of the stretched exponentials, Eqn. 5.9 becomes

$$Q_r(\Delta u) = a_r \, r^{-\zeta_\infty} \mathrm{e}^{-\alpha_r |\Delta u|^{\beta_r}}. \tag{5.11}$$

Because in shear turbulence the negative velocity (that go with the shear) increments are most relevant, we show in Fig. 5.7 the function $Q_r(\Delta u)$ of Eq. (5.11) for $\Delta u < 0$ and several distances r that span the inertial range $30 \leq r/\eta \leq 300$.

The figure illustrates that the more probable, negative tails of the probability density functions become independent of r when properly rescaled. This was of course already evident from the scaling exponents in Fig. 5.5 that were computed from precisely these tails. The inset of Fig. 5.7 shows, on a much expanded scale, that the function $Q_r(x)$ is completely consistent with our data. At very large Δu, the functions $Q_r(\Delta u)$ for different r start to deviate again, but this is already beyond the Δu needed to determine moments of order $p = 15$ (the maximum Δu_m needed is set roughly by the value where $\Delta u^{15} P_r(\Delta u)$ reaches a maximum, which is at $\Delta u_m = -3, -5$, and $-8\,\mathrm{ms}^{-1}$ for $r/\eta = 30, 100$ and 270, respectively).

5.5 Small-scale structures

Since we measure the turbulent velocity field with many probes simultaneously, it is possible to seek for strong events that extend in the shear ($y-$) direction; this is not possible in point measurements of the velocity field. In our quest for these events, we adopted the simple strategy to look for N velocity profiles

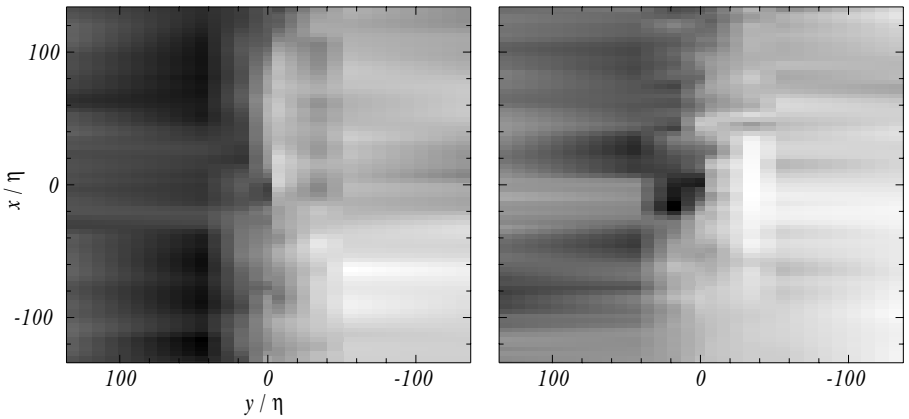

Fig. 5.8: *Snapshots of the turbulent velocity field (longitudinal component) illustrating that high negative increments occur at the interface of extended regions with uniform but different velocity. The magnitude of the velocity is represented by levels of grey from black to white, and the picture is obtained by displaying the interpolated sensor information (y-axis) against the longitudinal separation (x-axis), both normalized by the Kolmogorov scale η.*

$u(x,y)$ which have the largest transversal velocity difference $|\Delta u^T| = |u(x,y+\delta y) - u(x,y)|$ across two closely spaced probes (separation $\delta y/\eta = 6$), which is also a local maximum in the x-direction. An extensive description of our detection method is provided in section 3.6.2 of Chapter 3. The sign of strong events is favored by the shear, out of N events (e.g. $n = 200$ out of 10^8 line samples), $\approx 0.7N$ have the same (negative) sign as the shear. This is not a simple additive effect, the mean shear gives a mere $\Delta u_S = 0.1\,\mathrm{ms}^{-1}$ across the viscous-range separation δy, a factor of 4 smaller than the size fluctuation of the N largest events. A few snapshots of the measured velocity field in the neighborhood of large negative velocity increments are shown in Fig. 5.8. These (selected) snapshots reveal that the large event is in fact part of a "cliff": large velocity differences are also found across a line perpendicular to the shear. We will now demonstrate that this is also shown in conditional averages of the velocity field.

The separate averages of the positive and negative events were done by choosing the local maximum of Δu in the $x-$(streamwise) direction at $x = 0$. These average structures are shown in Fig. 5.9. Most remarkably, the average shape of the strongest events is very different for the negative and positive increments. Whilst the negative events clearly reveal a cliff-like structure of the velocity field, the average positive events are indistinguishable from those found in near-isotropic turbulence and do not carry the imprint of the large-scale shear. As high-order

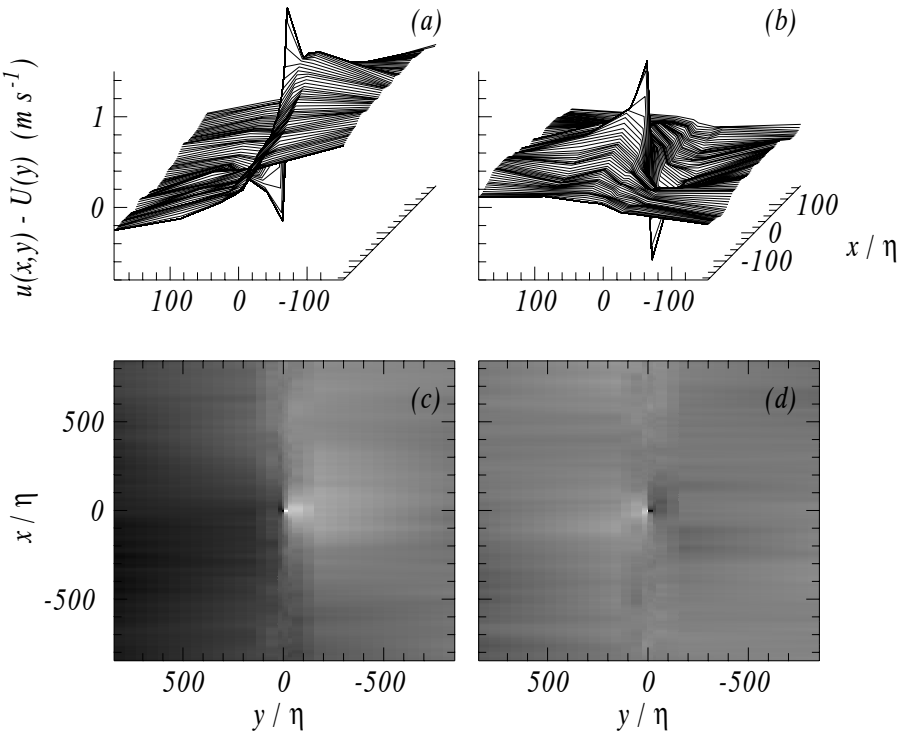

Fig. 5.9: *Mean velocity surfaces of the largest 256 events conditions over the separation $\Delta r = 6.1\eta$. The spatial transverse information from the 10 sensors is combined with the sample-resolution time information, to generate a square region.*

structure functions are determined by the negative events, it can now be understood why the behavior of the scaling exponents in shear turbulence differs from those in (near-) isotropic turbulence.

5.6 Scaling properties of left and right structure functions

The conclusion of the previous section indicated a large asymmetry between negative (with the shear) and positive velocity increments. This raises the interesting question wether structure functions of either negative or positive velocity increments have different scaling behaviour. These structure functions are defined as

$$S_p^+ = \int_0^\infty (\Delta u)^p P_r(\Delta u) \mathrm{d}\Delta u \tag{5.12}$$

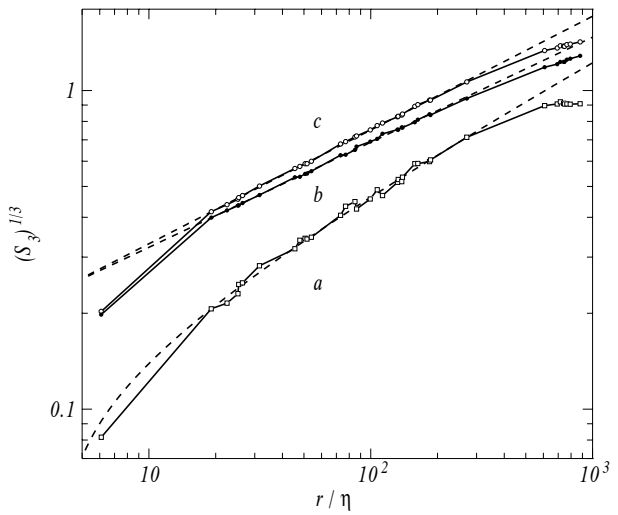

Fig. 5.10: *Third order transverse structure functions of homogeneous shear turbulence. Full lines: (a) the total structure function $S_p^T(r)$, (b) only from positive velocity increments $\Delta u > 0$ (S_3^{T+}) and (c) only from negative velocity increments $\Delta u < 0$ (S_3^{T-}). Dashed lines: (b) and (c), power laws $a_+ r^{\zeta_p^+}$ and $a_- r^{\zeta_p^-}$, respectively, fitted to the structure functions. The dashed line corresponding to (c) is the sum $a_- r^{\zeta_p^-} + a_+ r^{\zeta_p^+}$.*

for the positive $\Delta u > 0$ increments and

$$S_p^- = (-1)^p \int_{-\infty}^{0} (\Delta u)^p P_r(\Delta u) \mathrm{d}\Delta u \tag{5.13}$$

for the negative $\Delta u < 0$ increments. The even- and odd-order structure functions are the sum and difference of S_p^+ and S_p^-, respectively

$$S_{2p}(r) = S_{2p}^-(r) + S_{2p}^+ \tag{5.14}$$

$$S_{2p+1}(r) = S_{2p+1}^+ - S_{2p+1}^-(r). \tag{5.15}$$

Naturally, if the structure functions have scaling behaviour, $S_p \sim \zeta_p$, $S_p^+ \sim \zeta_p^+$, $S_p^- \sim \zeta_p^-$, then Eq. 5.15 dictates that $\zeta_p = \zeta_p^+ = \zeta_p^-$. However, if the negative velocity increments dominate the structure function, then we may have the situation that $\zeta_p^+ \neq \zeta_p^- = \zeta_p$. This, of course, would only be *apparently* so in the case of a finite inertial range. When contributions of positive and negative velocity increments are of the same order of magnitude, we must find all exponents ζ_p^+, ζ_p^-, ζ_p to be the same. That this can be difficult to see in the case of a relatively small inertial range is illustrated in Fig. 5.10, where we show S_3, S_3^+ and S_3^- which all apparently have different scaling exponents.

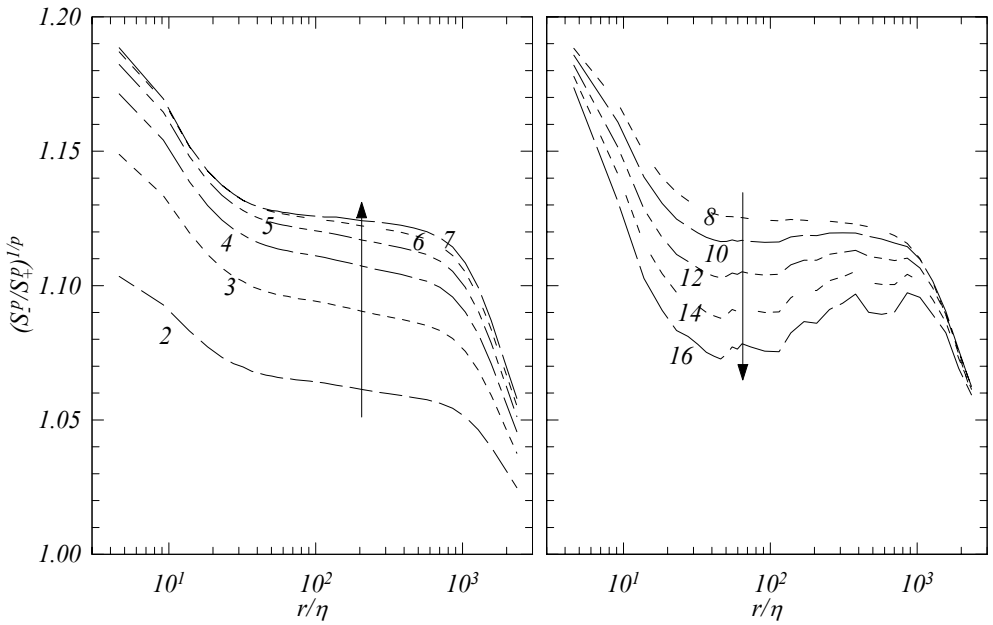

Fig. 5.11: *The ratio of left and right longitudinal structure functions S_-^p and S_+^p of equal orders in near-isotropic turbulence. For small orders $p \leq 7$ (a), S_p^- / S_p^+ is a decreasing function of r, above this order (b) S_p^- / S_p^+ is increasing with r.*

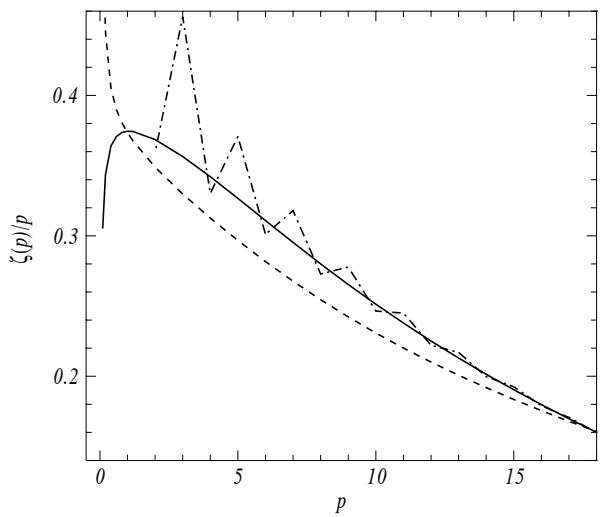

Fig. 5.12: *Differences between the left ζ_p^- (full line), right ζ_p^+ (dashed line) and total ζ_p (dash-dotted line) scaling exponents of transverse structure functions in homogeneous shear turbulence.*

The possibility that S_p^+ and S_p^- may scale differently with r has been extensively discussed in the literature [84]. Here we will critically evaluate this discussion. Sreenivasan *et al.* [84] considered the longitudinal structure function which results from a PDF which is asymmetric. This asymmetry is due to the energy cascade towards smaller scales, as is paraphrased by a non-zero third-order structure function

$$S_3(r) = -\frac{4}{5}\langle\epsilon\rangle r, \tag{5.16}$$

Negative longitudinal increments are more numerous than positive ones and it was suggested that large negative moments S_p^- scale differently than large positive moments S_p^+. The physical rationale is that fluid accelerations may be different than decelerations. We illustrate this by plotting in Fig. 5.11 the ratio S_p^-/S_p^+ that was computed from longitudinal increments in near-homogeneous and near-isotropic turbulence. While for a small p, the ratio S_p^-/S_p^+ is a decreasing function of r, it becomes an increasing function at $p \cong 7$. Therefore, for $p \geq 7$ apparently $\zeta_p^- \geq \zeta_p^+$, which is consistent with the circumstance that negative increments are more numerous than positive ones. This requirement can be appreciated by writing

$$S_p(r) = a_- r^{\zeta_p^-} + a_+ r^{\zeta_p^+}, \tag{5.17}$$

where the first term on the r.h.s. is dominating if $\zeta_p^- > \zeta_p^+$ and $a_- > a_+$. We also see that the large negative velocity increments are only a factor of 3 more numerous than the positive ones. Let us recall that such domination is required to simultaneously have (approximate) scaling of S_p and S_p^-.

Surprisingly, Sreenivasan *et al.* [84] also consider different scaling of the *small* $0 \leq p \leq 1$ order positive and negative moments. The problem is that (i) it is impossible to decide which of S_p, S_p^+, S_p^- has the algebraic behaviour in case of a finite inertial range, (ii) such different scaling (even an *apparent* scaling difference) is inconsistent because of the small difference between the number of negative and positive increments, (iii) a different scaling violates the exact relation (5.16) which singles out the true structure function as the scaling quantity. Further, Sreenivasan *et al.* [84] fail to notice that the different scaling of S_p, S_p^+, S_p^- is only apparent: in the case of infinite Reynolds number it will always be possible to decide which of the three has a true scaling behaviour.

Let us now return to the shear turbulence experiment, and see if large positive increments have a different scaling than the high order structure functions S_p and S_p^-. The result is shown in in both Fig. 5.5 and 5.12, where we have plotted all scaling exponents ζ_p^+, ζ_p^-, ζ_p as a function of the order (the latter figure emphasizes different scaling also at small orders). Self-similar Kolmogorov scaling would be the line $\zeta_p/p = 1/3$. It appears from Fig. 5.5 that only the ζ_p^- exponents tend to saturate towards higher orders p, an observation which

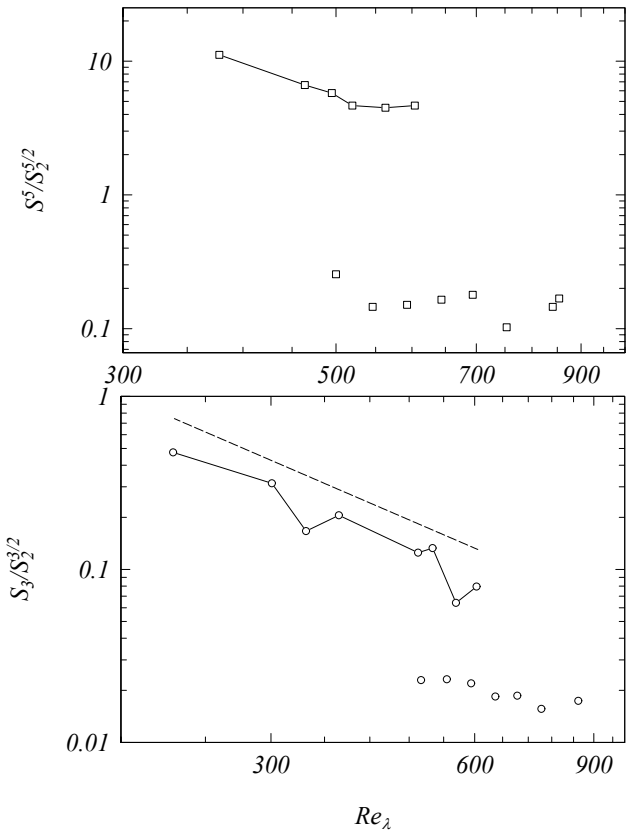

Fig. 5.13: *Variation of the transverse skewness over a range of Reynolds numbers varying from 150 to 600 for orders $p = 3, 5, 7$. The isolated symbols show the transverse noise measured by the array of probes in near-isotropic turbulence where odd-order transverse statistics should identically vanish. The dashed line is $Re_\lambda^{-1.69}$, which resulted from fitting the third order skewness with a power law.*

is in agreement with the result of section 5.5 (*i.e.* the asymmetric near-singular events can be identified only within the negative tail of the PDFs of velocity increments). The ζ_p^+ exponents show a different behaviour, but their anomaly is still stronger than, for example, the She-Leveque line . The conclusion is that the exponents ζ_p^+ are significantly different from ζ_p^- and both positive and negative velocity increments are strongly intermittent.

5.7 Variation of transverse skewness with Reynolds number

In the preceding section we have found that, at a single Reynolds number, the large-scale anisotropy persists down to the small scales. Conversely, if we concentrate at the anisotropy at the smallest scales, the question is if this will disappear at larger and larger Reynolds numbers. Increasing the Reynolds number moves the smallest scale further and further away from the injection scale and Kolmogorov's postulate of local isotropy (PLI) [48] predicts that the anisotropy should disappear.

To this aim we study the Reynolds number dependence of the derivative skewness

$$K_p = \frac{\langle (\partial u/\partial y)^p \rangle}{\langle (\partial u/\partial y)^2 \rangle^{p/2}}, \tag{5.18}$$

for $p = 3$ and 5. The derivatives in (5.18) were estimated from finite differences of velocities measured with probes separated by $\delta y = 1mm$. The result is shown in Fig. 5.13. As discussed in section 5.1, K_p should decrease with increasing Reynolds number as $K_p \sim {Re_\lambda}^{-1}$. As figure 5.13 illustrates, the observed decay for $p = 3$ is faster, while K_5 actually tends to a constant for large Re_λ.

A measurement of the skewness Eq. 5.18 is prone to noise. The noise was estimated by measuring $|K_p|$ in the case of isotropic turbulence where it should vanish exactly. These results are also shown in Fig. 5.13 and demonstrate that the measurements in shear turbulence are always safely above the instrumental noise level. Our results may be compared to those of Shen *et al.*, who have an inferior noise level.

In agreement with our finding that anisotropy persists at the small scales, we also find that a measure of small scale anisotropy persists for large Reynolds numbers.

5.8 The similarity of anisotropy in high Reynolds-number turbulence

In a recent paper [82], Shen and Warhaft advanced the idea that longitudinal and transverse structure functions possess identical scaling exponents in both sheared and non-sheared experiments, up to orders $p = 8$. This situation is compared to a set of small Re_λ experimental runs, where different scaling properties, transverse versus longitudinal, are indeed observed, with the conclusion that they are finite Reynolds number effects. It remained unclear why similar high-Reynolds number experiments [93] disclose a different anomalous scaling $\zeta_L(p) \neq \zeta_T(p)$.

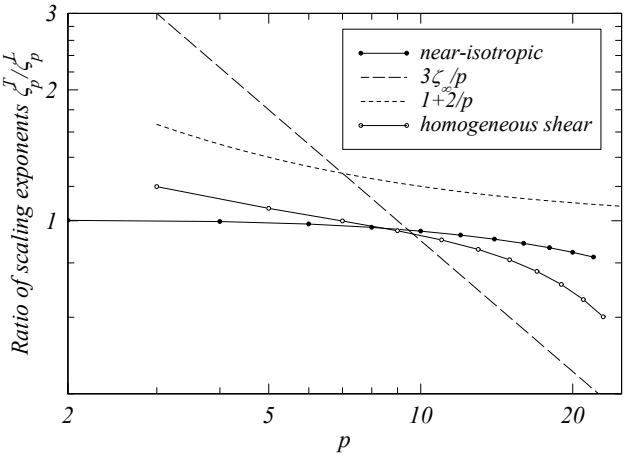

Fig. 5.14: *Relative scaling (transverse versus longitudinal) properties of near-isotropic turbulence ($Re_\lambda \approx 800$) and homogeneous shear flow ($Re_\lambda \approx 600$) is expressed through the ratio of the two kinds of measured scaling exponents. This is in turn compared to the dimensional predictions for the exponents' ratio: $\zeta_T(p)/\zeta_l(p) \sim 1 + 2/p$ for shear and $\zeta_T(p)/\zeta_l(p) \equiv 1$ in isotropic and homogeneous turbulence.*

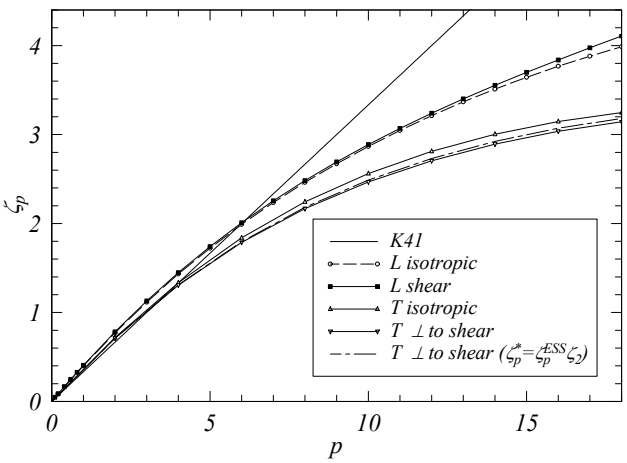

Fig. 5.15: *Transverse and longitudinal scaling exponents measured in the plane perpendicular to the shear direction and compared to their counterparts in near-isotropic and homogeneous turbulence. The dash-dotted line shows that the ESS method yields similar results to direct fits of the structure functions.*

In this chapter, an entirely different behaviour of transverse structure functions has been already discussed in the previous sections, with the note that we observe longitudinal structure functions that are almost identical to the near-isotropic case (Fig. 5.15). This observation dismisses the influence of small Reynolds-number effects, adding that the near-isotropic measurement is performed at a higher $Re_\lambda \sim 860$. We are apparently confronted with contradictory conclusions. This situation may be partially explained by the relatively small orders that could be measured in the transverse direction in [82], due to inhomogeneity effects, which have hidden the saturation behaviour at higher orders. However, small odd orders p of the transverse structure functions show a obvious deviation in the way they evolve with p, relative to their longitudinal counterparts, for example $\zeta_L(3) = 1.11 \neq 1.41 = \zeta_T(3)$. Similarly, our measured third order transverse exponent turns out to be much closer to the Lumley prediction [53] (see Eq. 5.6 of section 5.3) rather than to the Kolmogorov $S_p(y) \sim y^{p/3}$, again in contradiction with the findings of [82].

To further investigate this issue, we compare in figure 5.14 the ratio of the two dimensional predictions ($\zeta_T(p)/\zeta_l(p) \sim 1 + 2/p$ for shear and 1 for isotropic and homogeneous turbulence) with the ratio of the measured scaling exponents in homogeneous shear (odd orders) and near-isotropic turbulence. Despite the fact that individually the transverse and longitudinal scaling exponents are very different from each other and anomalous, their ratio clearly goes with p reproducing the functional form of the dimensional prediction of the same ratio, at least up to order 10. Naturally, this is not valid at higher orders, where saturation effects start to appear. In the case of near-isotropic turbulence the situation is similar, the measured ratio $\zeta_T(p)/\zeta_l(p)$ is close to one, but as early as order $p = 8$ starts to deviate from this value, in agreement with the different scaling of transverse and longitudinal increments.

It is very interesting to further investigate in higher Re_λ near-isotropic turbulent flows for the origins of this different scaling. A tempting explanation might be that in the case of homogeneous and isotropic turbulence, even in the limit of infinite Reynolds number, a distinct but universal scaling anomaly characterizes the two orientations (longitudinal and transverse). The starting point for this assumption is the observation that the longitudinal scaling exponents are identical in shear and in isotropic turbulence. For any other type of high-Reynolds number flows, observing this universal behaviour in the transverse exponents could be spoiled by the presence of large anisotropic scales. These anisotropies are felt throughout the inertial range and persist (as demonstrated in this study) down to dissipative scales. In this way, the structure functions measured in geometries that emphasize such an anisotropy, applied in a controlled manner at large scales (*e.g.* sheared turbulence), will result in non-universal scaling exponents. As we

will see next in this section, if the large scale anisotropies are not complex (as in homogenous shear), it is perhaps possible to find measurement geometries that are insensitive to these anisotropies, where universality is restored (in the sense previously announced).

We investigate if the shear effects are felt when measuring structure functions for separations r in the plane perpendicular to its direction. We saw that for the longitudinal structure functions (situated in this plane), we recover the scaling of isotropic turbulence. A measurement of the transverse structure functions perpendicular to the shear can be done through the 90° rotation of the sensing array (see figure 5.1(a)). The results are summarized in figure 5.15, which shows that not only the transverse scaling exponents are identical to those in isotropic turbulence, but that the saturation behaviour is also absent. This result also demonstrates that the intrinsic intermittency of shear turbulence can only be captured experimentally by using multi-point measurements.

5.9 Conclusions

Apart from presenting novel scaling properties of structure functions in homogeneous shear turbulence, this paper demonstrates the need for high-quality experiments and promotes the importance of high-order structure functions in sensing universal behaviour in turbulence. It is observed that the scaling of the low-orders ($p = 3$) obeys dimensional predictions, either for shear or near-isotropic turbulence. With the increase of the order, this property is increasingly obstructed by intermittency, leading to the two types of anomaly: one that quantifies the deviation from the K41, the other discriminating the two measurement directions, longitudinal and transverse. Since longitudinal scaling is observed not to be influenced by homogeneous shear, it is suspected that the nature of the first scaling anomaly is independent of the turbulence type. This claim is confirmed by the observation that, up to moderately high orders $p \leq 8$, the ratio of transverse to longitudinal scaling exponents in shear still reflects the dimensional predictions. Scaling of even higher-orders does not satisfy any of the considerations above, but instead reveals residual effects of the large-scale anisotropic forcing on the small-scale anisotropy. Explicitly, the small-scale survivors of the large-scale uniform shear are identified as strong events that are selected from the velocity fields. These structures correspond to distinctly isotropic and anisotropic vortical structures. Vortex filaments without a preferential orientation seem to determine the high-order scaling of the isotropic turbulence, while a mixture of these and shear-aligned vorticity sheets are causing saturation of scaling exponents in homogeneous shear. It is probable that the small-scale structure of inhomogeneous shear turbulence decomposes similarly and the way to disentangle its structure is

to resolve the high-order scaling of structure functions.

Chapter 6

REYNOLDS NUMBER DEPENDENCE OF LONGITUDINAL AND TRANSVERSE FLATNESS

Abstract

The flatness factor of velocity fluctuations in turbulent flows is a measure of intermittency. We study the dependence on the Reynolds number of both the longitudinal and transverse derivative flatness in windtunnel turbulence with $Re_\lambda \approx 450..800$. A suspected transition in the longitudinal derivative flatness around $Re_\lambda \sim 600$ is shown to be the consequence of limited hot-wire anemometry performance and can be amplified by improper filtering of the turbulence time-series. The transition effect is shown to be absent for the derivative flatness in the transverse direction, which is proven to be less sensitive to resolution problems.

6.1 Introduction

Fully developed turbulence describes the state of a turbulent fluid in which a well-developed inertial range is present. This requirement sets a lower limit on the Reynolds number, which was in Dimotakis [25] to be $Re_\lambda \approx 100 \ldots 140$. It is generally believed that for Reynolds numbers larger than this minimal value, the inertial range widens and no further transition to a turbulent state with a different character is encountered.

Surprisingly, a few years ago such a second transition (to "hard" turbulence) was discovered in turbulence driven by a temperature difference at very large values of the Rayleigh number (Procaccia *et al.* [72]). This has inspired a quest for an analogous transition in isothermal turbulence. Generally, the derivative flatness is chosen as the natural vehicle for such a quest. It is defined as

$$K_{ij} = \frac{\langle (\partial u_i / \partial x_j)^4 \rangle}{\langle (\partial u_i / \partial x_j)^2 \rangle^2} \tag{6.1}$$

If the derivatives have Gaussian statistics, then $K_{ij} = 3$, with deviations from 3 quantifying intermittency. The longitudinal flatness K_{11} is readily accessible in experiments where a time-series of streamwise velocities is measured in a single point. Invocation of Taylor's frozen turbulence hypothesis enables the translation of time derivatives into spatial derivatives. However, it must be noticed that problems with the Taylor hypothesis are gravest at the highest frequencies. This point will be worked out in detail in chapter 7.

The dependence of the longitudinal K_{11} on the Reynolds number has been documented extensively by van Atta and Antonia [7], who provide a compilation of $K_{11}(Re_\lambda)$ obtained in different flow geometries. Although Eq. (6.1) should be insensitive to many details (such as scale factors), it is still desirable to study the dependence of $K_{ij}(Re_\lambda)$ in a single experiment geometry. Such a study was performed by Tabeling *et al.* [87] in a turbulence experiment involving cold helium gas, which covered a wide Reynolds number interval $Re_\lambda \approx 150 \ldots 5040$. Tabeling *et al.* [87] discovered an apparent transition in $K_{11}(Re_\lambda)$ at $Re_\lambda \cong 700$, reminiscent of the transition to "hard turbulence" found in turbulent convection (Procaccia *et al.* [72]).

In a detailed theoretical study of possible experimental artifacts by Emsellem *et al.* [27], this transition was subsequently ascribed to probe resolution problems. Later studies by Pearson [67] in windtunnel turbulence over a range of Reynolds numbers $Re_\lambda \approx 400 \ldots 1200$ and new experiments by Tabeling and Willaime [86] both found evidence for a transition at $Re_\lambda \cong 700$. Both experiments of [87, 86] were done using the same flow configuration, but in [67] two windtunnels were used to span a large range in Reynolds numbers.

A possible transition to a new kind of fully developed turbulent flow is an extremely intriguing phenomenon which deserves very careful experiments. Such a study will be undertaken in this chapter.

As the Kolmogorov scale decreases with increasing Reynolds number and often drops below the size of the velocity sensor, probe resolution is a key problem. All probes that were used in the flatness studies were hot-wire probes. Emsellem *et al.* [27] identify various parasitic effects that may jeopardize hot-wire measurements of velocity derivatives and that may introduce a spurious transition.

Two main probe effects were identified: the increase in the probe response time due to thermal boundary layer effects, and secondly, the interference with the measured signal from vortex shedding off the probe. While both these effects were found to be responsible for changes in the value of the flatness close to the Reynolds number where the transition was observed, alternative tests, such as the dissipation rate test and the behaviour of dissipative length scales (such as the position of the peak in the dissipation spectra) with Reynolds number, showed that the probe response seemed to be constant over the entire range of measured

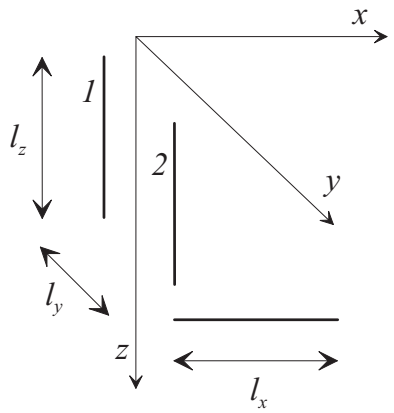

Fig. 6.1: *Probe configuration for measuring the derivative flatness K_{11} and K_{12}. The sensitive length of the probes is l_z and their separation is l_y. The mean flow points in the x-direction. Filtering of the time-dependent signal corresponds to a spatial filter length l_x.*

turbulent flows. The conclusion of the paper reconciliates the two contradictory observations: the transition in the flatness factor is still un unclear problem and should be better investigated in other experiments using closed flows, involving either larger scales or better instrumentation.

In the present experiments we focus on a Reynolds number interval close to where the transition was observed, namely from $Re_\lambda \cong 450$ to 800. In these experiments it is not possible to investigate the entire Reynolds-number interval achieved in the helium experiments, but the covered Re_λ interval contains the transition value.

The experiments are done in a windtunnel turbulent flow where the Kolmogorov scales remain large, which eases problems of probe resolution. In the next section, we will describe the used flow and ascertain its isotropy. Issues of probe resolution for the measurement of the turbulent dissipation are discussed in section 6.3. We will argue that it is advantageous to measure K_{12} in the case when small length scales remain unresolved in some directions of space. Finally, we discuss dependence of both K_{11}(section 6.4) and K_{12}(6.5) on the Reynolds number and conclude that the observed transition is most probably due to the limited probe resolution at the highest Reynolds numbers.

6.2 Experimental setup

To create large Reynolds number turbulence, the laminar flow of a recirculating windtunnel is passed through a grid, which induces a turbulent wake behind it.

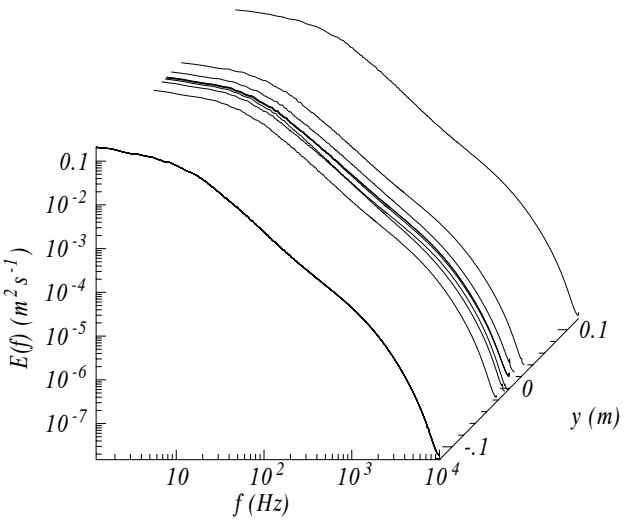

Fig. 6.2: *Longitudinal spectra of $Re_\lambda = 698$ turbulence, measured simultaneously at various transverse positions in the flow.*

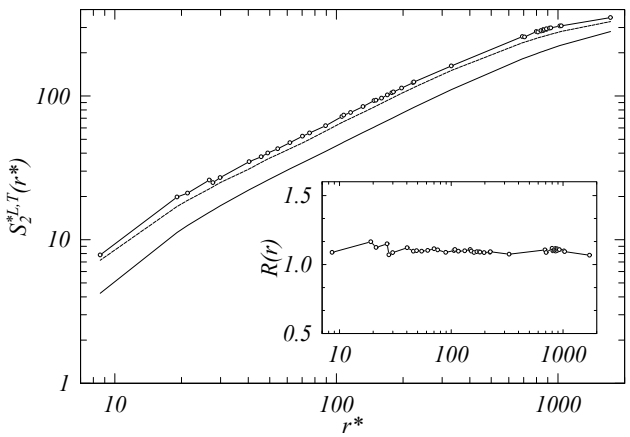

Fig. 6.3: *Longitudinal and transverse second order structure functions used for assessing the isotropy of the turbulent flow. The dashed line corresponds to the transverse structure function $\tilde{S}_2^T$ in the ideal case of homogeneous and isotropic turbulence, computed from the r.h.s. of Eq. (6.4). The inset shows the ratio $R(r) = S_2^T/\tilde{S}_2^T$. The $*$ denotes normalization on dissipative quantities $r^* = r/\eta$, $S_2^* = S_2/v_K^2$, where η, $v_k = \nu/\eta$ are the Kolmogorov length-scale and velocity, respectively.*

Re_λ	$\eta \times 10^4(m)$	$\epsilon_{\mathrm{VSR}}(m^2s^{-3})$	$\epsilon_{\mathrm{ISR}}(m^2s^{-3})$	$U(m/s)$	$u_{rms}(m/s)$	$f_{c2}(Hz)$
498	2.12	1.65	1.45	5.07	0.800	4600
546	1.86	2.82	2.35	6.11	0.958	6000
593	1.65	4.55	3.72	7.18	1.125	7300
644	1.49	6.81	5.52	8.29	1.297	8700
698	1.37	9.57	7.76	9.35	1.462	9400
754	1.27	12.7	10.8	10.41	1.639	10000

Tab. 6.1: *Longitudinal turbulence characteristics for one of the two identical experimental runs. In the column titles Re_λ is the Taylor-microscale Reynolds number, η the Kolmogorov length scale, ϵ_{VSR} and ϵ_{ISR} are the mean dissipation rates determined in the viscous, respectively inertial range, and f_{c2} is the cut-off frequency of the numerical post-filtering.*

The structure of the grid is derived from the classical symmetric square mesh, which has been used to generate isotropic moderate Reynolds-number turbulence throughout the 60's in the work of Comte-Bellot and Corrsin [21, 22]. The grid geometry, similar to that used by Pearson [68], does not obstruct the entire section of the windtunnel and has a multiscale structure which resembles a chessboard pattern. With turbulent intensity around 10%, the flow has a Reynolds number which is a factor of two higher than classical passive grids: for our windtunnel which has a measurement section of $8m$ and a cross-section of $0.7 \times 0.9m^2$, the maximal value of the Reynolds number achieved was $Re_\lambda \sim 900$.

For the measurement of the turbulent signals we used an array of 10 single hot-wire probes which is positioned perpendicularly to the direction of the mean flow in the windtunnel. The transverse spacing between the individual probes is chosen suitable for measurement of transverse turbulence quantities with separations both in the viscous sub-range (VSR) and the inertial sub-range (ISR), while the longitudinal quantities are extracted from individual probes, by reinterpreting the time lags as spatial increments via the Taylor frozen turbulence hypothesis. Although two closely spaced probes would suffice for measuring both longitudinal and transverse derivatives, the lateral information provided by the array was used for assessing the isotropy of the flow. We simultaneously sample the 10 time-signals for all runs at a frequency of 20 kHz and low-pass filter them at $f_c = 10kHz$, in accordance to the Nyquist rule. As noise can contaminate a measurement of the flatness, the acquired data was numerically filtered at a frequency f_{c2}, close to the Kolmogorov frequency $f_K = U/2\pi\eta$.

The homogeneity of the flow in the y-direction is illustrated in Fig. 6.2, where we show the spectra obtained at various positions in the probe array at Reynolds number $Re_\lambda = 698$. It is seen that the spectra do not depend on y

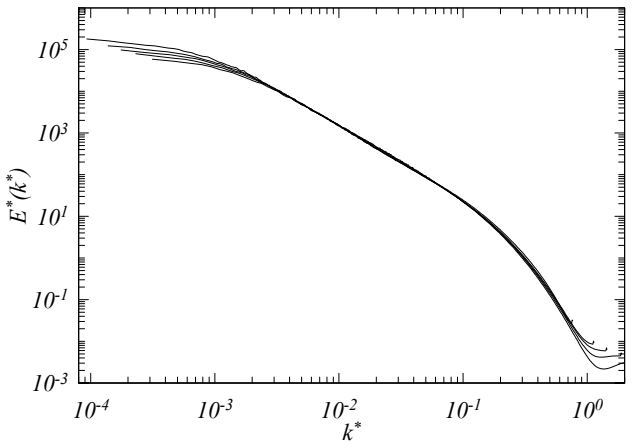

Fig. 6.4: *Normalized longitudinal spectra obtained from one of the sensors, for all measured Reynolds numbers. The normalization is done with respect to the dissipative scale quantities:* $k^* = k\eta/2\pi$, $E^* = E(f)(2\pi/U)\epsilon_{\mathrm{VSR}}^{-2/3}\eta^{-5/3}$, *where* η *is the Kolmogorov length scale,* ϵ_{VSR} *is the dissipation and* f *is the frequency.*

and display a well-defined inertial range. Isotropy was checked by measuring longitudinal and transverse structure functions

$$S_2^L(r) = \langle (u(\mathbf{x}+r\hat{\mathbf{e}}_x) - u(\mathbf{x}))^2 \rangle, \tag{6.2}$$

$$S_2^T(r) = \langle (u(\mathbf{x}+r\hat{\mathbf{e}}_y) - u(\mathbf{x}))^2 \rangle \tag{6.3}$$

and testing the satisfaction of the isotropy relation

$$\tilde{S}_2^T(r) = S_2^L(r) + \frac{r}{2}\frac{dS_2^L(r)}{dr} \tag{6.4}$$

Fig. 6.3 shows both the longitudinal and transverse structure functions; in the inset the anisotropy is estimated through the ratio $R(r)$ between the measured transverse structure function and the right-hand side of Eq. (6.4), computed from the measured longitudinal structure function. The ratio $R(r)$ is very close to one, as usually observed in turbulent wakes of symmetric grids [21]. It is necessary to mention that satisfaction of relation (6.4) provides only a limited isotropy check, since hot-wire anemometry used in this experiment measures only the longitudinal u_x velocity component.

6.3 Assessment of probe effects

For each Reynolds number in the range $Re_\lambda = 498 \ldots 754$ two sets of experiments were done. The turbulence characteristics of these experiments are listed in ta-

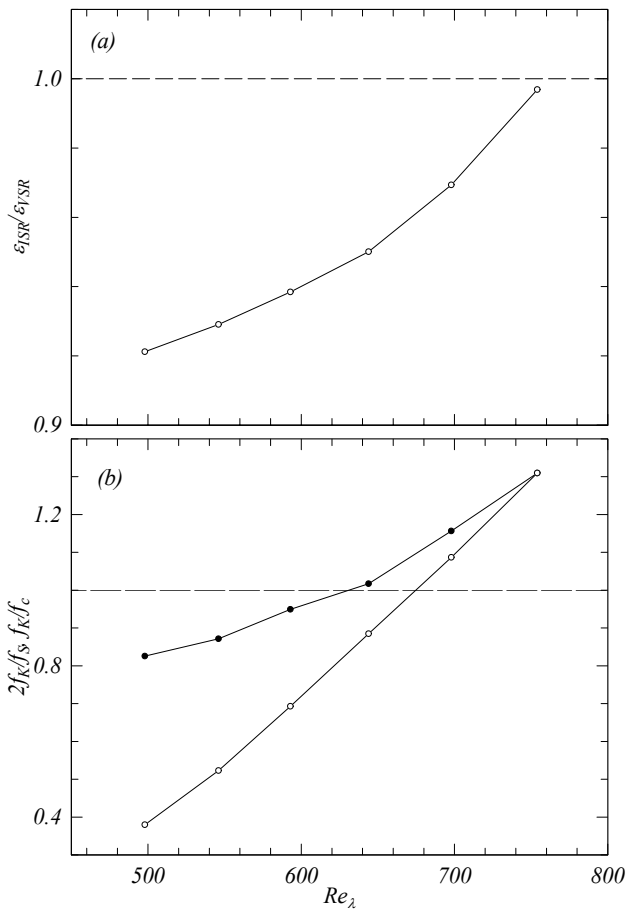

Fig. 6.5: *(a) Ratio of the mean dissipation rates against the Reynolds number, measured from dissipative range ϵ_{VSR} or inertial range ϵ_{ISR} quantities, using Eq. (6.5) and Eq. (6.7), respectively. (b) Variation of the Kolmogorov frequency $f_K = U/2\pi\eta$ with the Reynolds number (empty markers). For the higher Re_λ runs, its value exceeds the Shannon frequency $f_K \geq f_c$. Also shown is the ratio of f_K and the frequency f_{c2} that was used for the numerical post-filtering of the data (closed markers). When $f_K \geq f_c$, $f_{c2} \approx f_c$.*

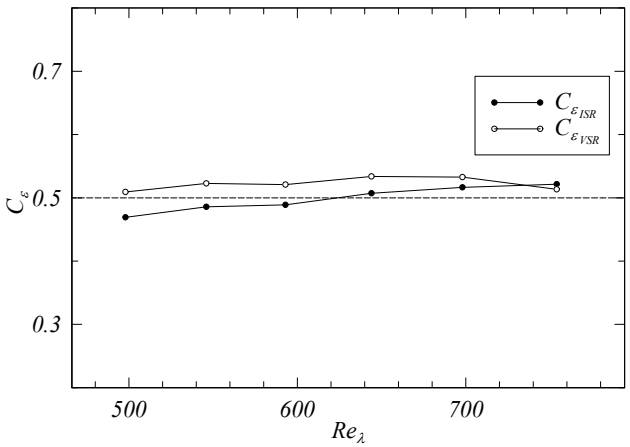

Fig. 6.6: *Dependence of the value of the Kolmogorov constant C_ϵ (see Eq. (6.8)) on the Reynolds number. The values are calculated either using ϵ_{VSR} (empty markers) or ϵ_{ISR} (full markers).*

ble 6.1. As vortex shedding off probes was extensively studied in Emsellem *et al.* [27], where it was suspected to be a cause for the a spurious Re_λ transition of the flatness, we will assess its importance here. Of relevance is the Reynolds number based on the diameter of the wire $d = 2.5 \cdot 10^{-6} m$, which for the range of velocities considered here is in the range $Re_d = 0.8 \ldots 1.6$. This is below the critical Reynolds number ($Re_d = 40$) for vortex shedding (Tritton [89]). Therefore, vortex shedding is irrelevant. To prove that vortex shedding from other structures, such as supports of the wires, is also insignificant, we show in Fig. 6.4 the normalized energy spectra for the range of Reynolds numbers considered. No accidental high frequency peaks can be observed in these spectra.

We investigate next the dissipation rate test, which compares the mean energy dissipation rate ϵ computed either directly as a dissipative quantity from the velocity derivative (assuming isotropy of the flow), or as an inertial range quantity from the Kolmogorov equation for the third-order structure function.

$$\epsilon_{\mathrm{VSR}} = 15\nu \int_0^\infty k^2 E(k) \mathrm{d}k \tag{6.5}$$

$$\epsilon_{\mathrm{ISR}} = \frac{-S_3^L(r) + 6\nu(dS_2^L/dr)}{(4/5)r} \tag{6.6}$$

According to Moisy *et al.* [57], a more accurate procedure for the extraction of ϵ_{ISR} is to fit a forced version of the Kolmogorov equation (Novikov [62])

$$-\frac{S_3^L(r)}{r} + \frac{6\nu}{r}\frac{dS_2^L}{dr} = \frac{4}{5}\epsilon_{\mathrm{ISR}}\left(1 - \frac{5}{14}\frac{r^2}{L_f^2}\right), \tag{6.7}$$

where L_f is an external scale characterizing the forcing, but distinct from the longitudinal integral scale L_{11}. In order to determine ϵ_{ISR}, Eq. 6.7 was fitted to measured longitudinal structure functions S_2^L and S_3^L, with ϵ_{ISR} and L_f as free parameters. The value of ϵ_{ISR} is less sensitive to how well the dissipative scales are resolved. If the probe response does not diminish with the increase in the Reynolds number, then the ratio $\epsilon_{\mathrm{ISR}}/\epsilon_{\mathrm{VSR}}$ should be constant and close to 1. In Fig. 6.5(a) we can see that this ratio stays below 1 for all the Reynolds numbers considered.

The ratio $\epsilon_{\mathrm{ISR}}/\epsilon_{\mathrm{VSR}}$ increases with Reynolds number, most probably because ϵ_{VSR} is increasingly underestimated. This increase corresponds with an increase in the ratio of the Kolmogorov frequency $f_K = U/2\pi\eta$ and the sampling frequency, as is shown in Fig. 6.5(b). The latter figure also illustrates the two filtering strategies used: either filtering at the Shannon frequency f_c, or filtering close to the Kolmogorov frequency at f_{c2}. In the last case, the frequency response as a function of the Reynolds number is discontinuous when f_K grows larger than f_c, since f_{c2} cannot exceed f_c. We will demonstrate that the main conclusion of this chapter does not depend on the strategy chosen.

A final test that compares a dissipative range quantity which is affected by probe resolution and a macro-scale quantity which is unaffected by probe resolution is the measure of the dimensionless dissipation rate

$$C_{\epsilon_{\mathrm{VSR}}} = \epsilon_{\mathrm{VSR}} \frac{L_{11}}{{u_{\mathrm{rms}}}^3}, \tag{6.8}$$

where L_{11} is the integral length scale

$$L_{11} = \int_0^\infty \langle u(0)u(r)\ dr \rangle.$$

Over a very large range of Reynolds numbers, $C_{\epsilon_{\mathrm{VSR}}}$ was shown to be constant in a flow geometry similar to the one we have, but in a different experiment employing an entirely different setup (Pearson [68]). Constancy of C_ϵ is of course the essence of Kolmogorov's self-similar theory of turbulence.

To conclude this section, we observe a weak dependence of the ratio $\epsilon_{\mathrm{ISR}}/\epsilon_{\mathrm{VSR}}$ which may be caused by finite sampling frequency in our experiments. On the other hand, the dimensionless dissipation rate is found to be constant. Matters of time resolution will be discussed in detail in section 6.5, when we compare the measurement of G_{12} and G_{11}.

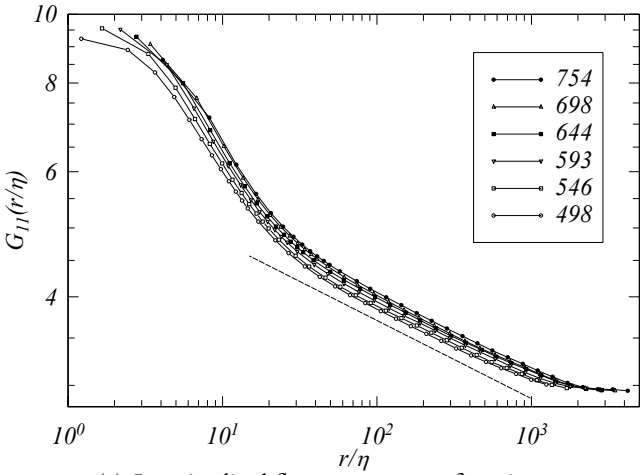

(a) Longitudinal flatness structure functions

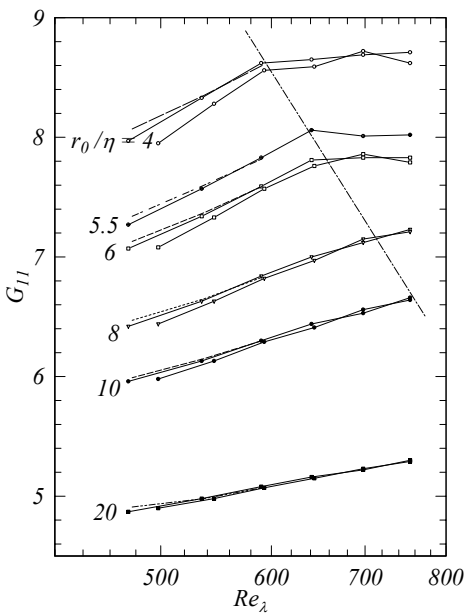

(b) Re_λ dependence of G_{11} at fixed r_0/η

Fig. 6.7: *(a) Evolution of the longitudinal flatness structure functions $G_{11}(r)$ with the normalized separation r/η for Re_λ varying from $\sim$ 450 to $\sim$ 750. The dashed line has slope $\zeta \sim -0.1$. (b) Values extracted from $G_{11}(r)$ for several separations r_0/η in the intermediate dissipative range. A second set of curves, produced in a separate experiment running over the same Re_λ range shows that the values are reproducible. The over-imposed dashed lines show the effect of the digital post-filtering on G_{11}, which is minimal. The diagonal dash-dotted line suggests a trend for the dependence of a break point in G_{11} on the separation r_0/η.*

6.4 Longitudinal flatness

The derivative flatness (Eq. 6.1) is the limit for vanishing separations r of the flatness structure function

$$G_{ij}(r) = \frac{\langle (u_i(\mathbf{x} + r\hat{\mathbf{e}}_j) - u_i(\mathbf{x}))^{2l} \rangle}{\langle (u_i(\mathbf{x} + r\hat{\mathbf{e}}_j) - u_i(\mathbf{x}))^2 \rangle^l} \tag{6.9}$$

with $l = 2$. For inertial range separations r, $G_{ij}(r)$ shows an algebraic dependence $G_{ij}(r) \sim r^{\zeta}$ with the exponent ζ related to the anomalous exponents of the structure functions of order 2 and 4, $\zeta = \zeta_4 - 2\zeta_2$. This is illustrated in Fig. 6.7(a), where $\zeta = -0.106$, which agrees with the well-accepted values of the exponents ζ_p (Arneodo *et al.* [6]). Also the derivative flatness

$$K_{ij} = \lim_{r \to 0} G_{ij}(r)$$

will be influenced by intermittency. This reflects Kolmogorov's refined similarity hypothesis in which the statistical properties of inertial- and dissipative-range quantities are linked (Kolmogorov [49]). It is precisely this effect that will be studied here. We have already indicated that resolution is an important issue in studies of the Reynolds number dependence of the derivative flatness $K_{ij}(r)$. In Fig. 6.7(a) it is seen that the smallest scale reached in $G_{11}(r)$ increases with increasing Reynolds number.

In order to estimate the value of $G_{11}(r)$ at $r = 0$ it is necessary to fit a polynomial $\mathcal{P}(r) = a + br^2 + cr^4$ to the measured $G_{11}(r)$ in the interval $r \in [0, r_1]$, where we choose $r_1/\eta \leq 20$. The polynomial is forced to an even order by the reflection property of $G_{11}(r)$. Even with this procedure, it is very difficult to estimate K_{11} reliably, since the fitting range will gradually shorten with the increase of the Reynolds number. It is a common practice to take instead the values measured at the first accessible separation r as representative for derivative quantities of turbulence such as flatness.

Rather than attempting to find the true flatness $K_{11} = G_{11}(r \to 0)$, we will evaluate G_{11} at fixed separations $r_0/\eta \geq 4$ at all the measured Reynolds numbers by substituting r_0 in the polynomial $\mathcal{P}(r)$. The result of the procedure for different r_0-values is shown in Fig. 6.7(b). The smallest r_0/η shown is also the smallest resolved separation of $G_{11}(r)$ at the largest $Re_\lambda = 754$. We observe that this length is already influenced by time filtering ($l_x/\eta > 1$). While for large r_0 the flatness structure function $G_{11}(r_0)$ smoothly increases with Re_λ, there is an apparent break around $Re_\lambda = 650$ at $r_0/\eta \leq 6$. Remarkably, this break occurs at approximately the same Re_λ where Tabeling and Willaime [86] found a transition of the derivative flatness. We also remark that the effect of the post-filtering that was done to remove high-frequency noise is insignificant. This is an important

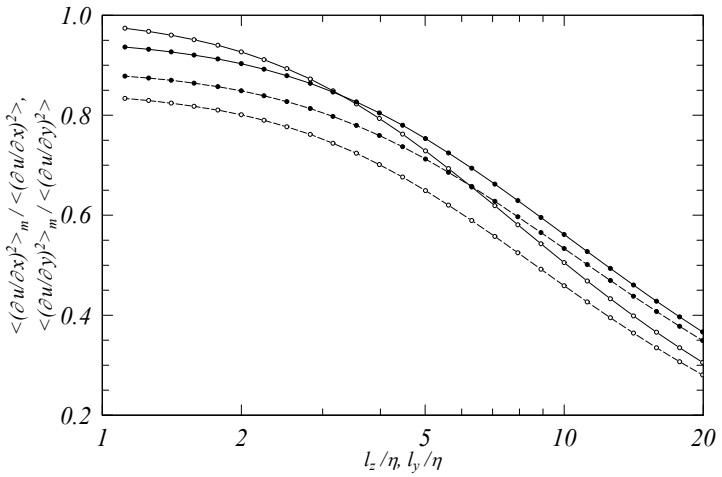

Fig. 6.8: *The influence of the time-filtering (corresponding to a scale $l_x/\eta = 1$) on the measured r.m.s. values of the longitudinal (○) and transverse(●) derivatives $\langle(\partial u/\partial x)^2\rangle_m$, $\langle(\partial u/\partial y)^2\rangle_m$ evaluated from the Pao model spectrum of turbulence. In the transverse case, a 2-probe configuration is used, with equal sensor lengths l_z/η, separated by l_y/η, equal to the sensor lengths. Both l_z/η and l_y/η are varied simultaneously. The longitudinal case is evaluated from a single wire configuration, where the length of the sensor l_y/η is varied. The curves show that the loss of resolution due to time-filtering (dashed lines) is larger when the r.m.s. of the longitudinal derivative is measured. When time-filtering is absent $l_x = 0$ (full lines), the situation is reversed and the longitudinal configuration is more accurate at measuring derivatives.*

observation, because our strategy of filtering at f_c has a nonuniform Reynolds number dependence.

A suspicious effect, however, is that the apparent transition Reynolds number seems to increase with increasing r_0. This suggests that this transition may be a resolution artefact. On the other hand, if we assume a resolution artefact, then the scaling with Re_λ is not right. Roughly, $\eta \sim Re_\lambda^{-3/2}$ so that if a transition occurs at $r_0/\eta = 4$ at $Re_\lambda \sim 580$, it would also occur at $Re_\lambda = (6/4)^{3/2} \cdot 580 \cong 1000$ at $r_0/\eta = 6$, which is significantly larger than the observed transition Reynolds number at this separation.

We conclude that at this point the observed transition hints at a resolution artefact, but it can not be completely ruled out that it may be genuine.

6.5 Transverse flatness

We have seen that a measurement of the flatness will invariantly encounter the limitations of the probe resolution. Therefore it is useful and instructive to compute the influence of averaging when measuring turbulent fluctuations that correspond to a model spectrum. To this aim we will consider measurements of both the longitudinal K_{11} and the transverse K_{12}.

A quite subtle problem in measuring K_{11} is the applicability of the Taylor's frozen turbulence hypothesis. Measuring derivatives involves the high frequencies, which are most affected by deviations from frozen turbulence. These problems are absent when measuring K_{12} by using two separate probes. The experimental arrangement is sketched in Fig. 6.1. Resolution of the small scales, which is needed for measurement of the derivatives, is limited by the finite wire length l_z, the finite probe separation l_y and the finite time resolution which corresponds to a length scale l_x through Taylor's hypothesis. Resolution limitations in y- and z-directions have been studied by Frenkiel [34, 33], Corrsin and Kovasznay [23] and Wijngaard [94, 95, 96]. Their calculations include more complicated hot-wire sensor configurations, such as $\times$-probes and vorticity sensors. They concluded that the size of the probes used should be of the order of the Kolmogorov microscale if an accurate measurement of the r.m.s. velocity derivatives is desired. Here we will also compute the effect of time filtering. It is our aim to compare for this case the longitudinal and transverse flatness.

As we do not know how to build model spectral densities that have a non-trivial flatness, we will only study the effect of averaging on $\langle(\partial u/\partial x)^2\rangle$ and $\langle(\partial u/\partial y)^2\rangle$, *i.e.* the denominator in the expression for the flatness.

The starting point is the isotropic spectral density

$$\Phi_{ij}(\mathbf{k}) = \frac{E(\mathbf{k})}{4\pi k^4}(k^2\delta_{ij} - k_i k_j), \tag{6.10}$$

where for $E(\mathbf{k})$ we take the isotropic Pao spectrum ([65])

$$E(\mathbf{k}) = E(k) = \alpha C^{2/3} k^{-5/3} \exp\left(-3/2\alpha(k\eta)^4\right) \tag{6.11}$$

In wavenumber space, the action of the averaging can be expressed by its spectral transfer functions

$$|H_z(k_z)|^2 = \frac{\sin^2(l_z k_z/2)}{(l_z k_z/2)^2}, \tag{6.12}$$

whereas the approximation to the average derivative $\langle(\partial u/\partial y)^2\rangle$ through a finite difference by 2 wires in the y-direction is given by

$$|H_y(k_y)|^2 = \frac{4}{l_y^2}\frac{\sin^2(l_y k_y/2)}{(l_y k_y/2)^2}. \tag{6.13}$$

Finally, the representation of the electronic low-pass filter in the spatial domain $|H_x(k_x)|^2$ is given by

$$|H_x(k_x - k_x^c)|^2, \tag{6.14}$$

with k_x the cut-off wavenumber. We assume that the sampling in time is fast enough so that the approximation to the longitudinal x-derivative becomes

$$\langle(\partial u/\partial x)^2\rangle \cong \int k_x^2 H_x^2(k_x - k_x^c) H_z^2(k_z) \Phi_{xx}(\mathbf{k}) d\mathbf{k}, \tag{6.15}$$

whereas the approximation of the transverse y-derivative through a finite difference becomes

$$\langle(\partial u/\partial y)^2\rangle \cong \int H_x^2(k_x - k_x^c) H_y^2(k_y) H_z^2(k_z) \Phi_{xx}(\mathbf{k}) d\mathbf{k} \tag{6.16}$$

As it suppresses the factor k_x^2, the influence of the time- (k_x-) filtering is more detrimental for the estimate of the longitudinal derivative than for the transverse one. This effect is illustrated in Fig. 6.8 where we show the result of a numerical evaluation of Eq. (6.15),(6.16), where instead of letting the time-filtering scale l_x grow above the Kolmogorov scale, we chose to have it fixed at $l_x/\eta = 1$ and then decrease the resolution ($1 \leq l_y/\eta,\ l_z/\eta \leq 20$) of the spatial filtering.

In our experiment $l_x/\eta \sim 4$, $l_y/\eta = 7.2$ and $l_z/\eta = 1.5$ for the largest Re_λ. In this situation the effect of the time-filtering is assessed by comparing the flatness structure functions at equal transverse and longitudinal separations $\Delta y = \Delta x \cong l_y/\eta$. As the separations Δy, Δx are of the same order as the time-filtering length-scale l_x and all close to η, we believe that the longitudinal $G_{11}(\Delta x)$ will be less accurately determined than the transverse $G_{12}(\Delta y)$, similar to what is observed for our model spectrum. The apparent transition in the longitudinal flatness function also shows in a cross-over of the curves in Fig. 6.7(a). The question is if a measurement of the transverse flatness function $G_{12}(r)$ will exhibit a similar cross-over. The functions $G_{11}(r)$ and $G_{12}(r)$ are compared in Fig. 6.9. Contrary to $G_{11}(r)$, $G_{12}(r)$ does not show a cross-over and increases monotonically with the Reynolds number. However, as the separation r in $G_{12}(r)$ is a true physical separation, the discrete distances of $G_{12}(r)$ are more sparse because the number of probes that can be compressed in a small volume is limited.

It is known that probe influence affects the measurement of spatial derivatives using 2 probes for $r/\eta \lesssim 3$ (Zhou *et al.* [98]). As our smallest separation is larger than this value, we believe that our spatial measurements of G_{12} are correct. Then, it can also be concluded from Fig. 6.9 that the transverse flatness K_{12} shows a stronger dependence on the Reynolds number than the longitudinal K_{11}.

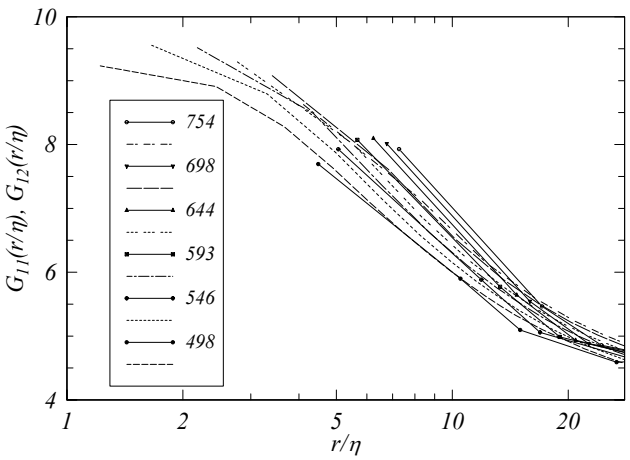

Fig. 6.9: *Comparison between measured values for the transverse and longitudinal flatness for separations r/η in the intermediate dissipative range scales, for different values of the Reynolds number, shown in the legend. The full lines represent the transverse flatness obtained from different sensors and the dashed lines represent the single-probe longitudinal flatness, simultaneously recorded at the indicated turbulence levels. The transverse flatness curves have the same shape, irrespective of Re_λ and no transitional behaviour is observed.*

6.6 Conclusions

We measured the longitudinal and transverse flatness structure functions of isotropic and homogeneous turbulence, $G_{11}(r)$ and $G_{12}(r)$, for separations r in the dissipative range, over a selected Reynolds number range, $Re_\lambda \cong 450 \ldots 800$. The longitudinal and transverse flatnesses K_{11}, respectively K_{12} were approximated by the values of the flatness structure functions $G_{11}(r)$ and $G_{12}(r)$ at the smallest separations that we could resolve with our experimental setup. We showed that a transition in the Reynolds number dependence of the longitudinal flatness $K_{11}(Re_\lambda)$ is most probably caused by the finite-time resolution of the experiment. This is corroborated by the transverse flatness, which does not show such a transition. Using a model spectrum to quantify errors in the experimental approximation of derivatives we verify that resolution problems are expressed differently in the longitudinal and transverse derivatives. For future work, it would be desirable to have a finer grid of spatial separations.

The transverse flatness is monotonously increasing with Re_λ and does not exhibit any sudden variation near the Re_λ of the suspected transition, but the smallest transverse scales that are resolved are larger than the longitudinal scales.

Chapter 7

TURBULENT WAKES OF FRACTAL OBJECTS

Abstract

Turbulence of a windtunnel flow is stirred using objects which have a fractal structure. The strong turbulent wakes resulting from three such objects which have different fractal dimensions are probed using multiprobe hot-wire anemometry in various configurations. Statistical turbulent quantities are studied within inertial and dissipative range scales in an attempt to relate changes in their self-similar behaviour to the scaling of the fractal objects.

7.1 Introduction

The self-similar structure of turbulence underlies Kolmogorov's well-known 1941 theory. In a modern geometrical phrasing of this theory, turbulent dissipation would be organized on a space-filling fractal set. In the same vein, small-scale intermittency results if this set is no longer space filling.

It is broadly believed that fully developed turbulence, when given enough time, creates its fractal structure *by itself*, no matter how the turbulent flow is excited. An intriguing idea is to impose a self-similar structure on the flow, for example by creating turbulence in the wake of a fractal object. The question is whether the imprint of the excitation can be seen in the turbulent structure of the wake. In other words, whether the scaling properties of the object can determine, at least for some time, the scaling properties of the turbulent wake that is shed off the object. Thus, we may be able to directly influence the scaling exponents of fully developed turbulence and their related turbulence dissipation field. As a practical application, this idea may lead to improved turbulence generators and objects with novel drag properties. It should be noted that a direct influence of the fractal stirring on the scaling properties of the velocity field was demonstrated in the context of a reduced-mode model (the GOY model)[63].

Preliminary experiments by Queiros-Conde & Vassilicos [74] have hinted such an effect, but the structure functions used were rather unorthodox. The problem was that these quantities made it difficult to unravel the effect of the finite size of the fractal object from the effect of its scale invariant structure. In the present study we attack this problem by measuring energy spectra and longitudinal as well as transverse structure functions. Our conclusion is that there may be a direct relation between the scaling properties of the fractal object and the turbulence that it creates. Whilst the latter conclusion may not sound firm, we believe that it is interesting to expose the caveats and ambiguities of the experimental techniques used to reach it.

The fractal turbulence generators used are those of [74]. They have (necessarily) finite size and create very strong turbulence. We demonstrate that it is precisely these two circumstances that make it difficult to establish a direct relation between the scaling of the generator and the scaling of the turbulent wake it sheds.

7.2 Experimental setup

Our fractal objects are self-similar constructions with the smallest scales limited to $1\,mm$ by manufacturing constraints (see [74] for a full description of these objects). With the size L of the fractal objects ranging between 17 and 37 cm, the number of iterations is limited to 4. A schematic view of these objects is provided in Fig. 7.1a. The wake of three objects of increasing fractal dimension (2.05, 2.17, 2.40) placed in the $0.7\,m \times 0.9\,m$ section of the tunnel was generated with a laminar flow that reaches $22\,ms^{-1}$ in an empty windtunnel. The measurements were done with a rake of 10 hot-wire probes at different positions behind fractal objects. Different orientations of the objects themselves with respect to the direction of the incoming flow of the windtunnel were used. The possible measurement configurations are sketched in Fig. 7.1b.

The wakes of the fractals are strongly turbulent, a feature that challenges the application of hot-wire anemometry. Hot-wire sensors cannot discriminate between positive and negative fluid velocities along the x-direction (see Fig. 7.1b) u and $-u$. In particular, the sensor information is ambiguous as to the direction of the velocity in a plane perpendicular to the wire if the relative turbulent fluctuations, u/U and v/U, are large (where U is the time-averaged fluid velocity in the x-direction and v is the fluid velocity in the y-direction – see Fig. 7.1b). Despite these disadvantages, hot-wire anemometry is still the only way to obtain statistically accurate measurements of the small-scale velocity field in strong turbulence. All standard turbulence statistics presented here are in terms of *spatial* velocity increments $u(x+r,t) - u(x,t)$ at equal times. Time-dependent measurements at

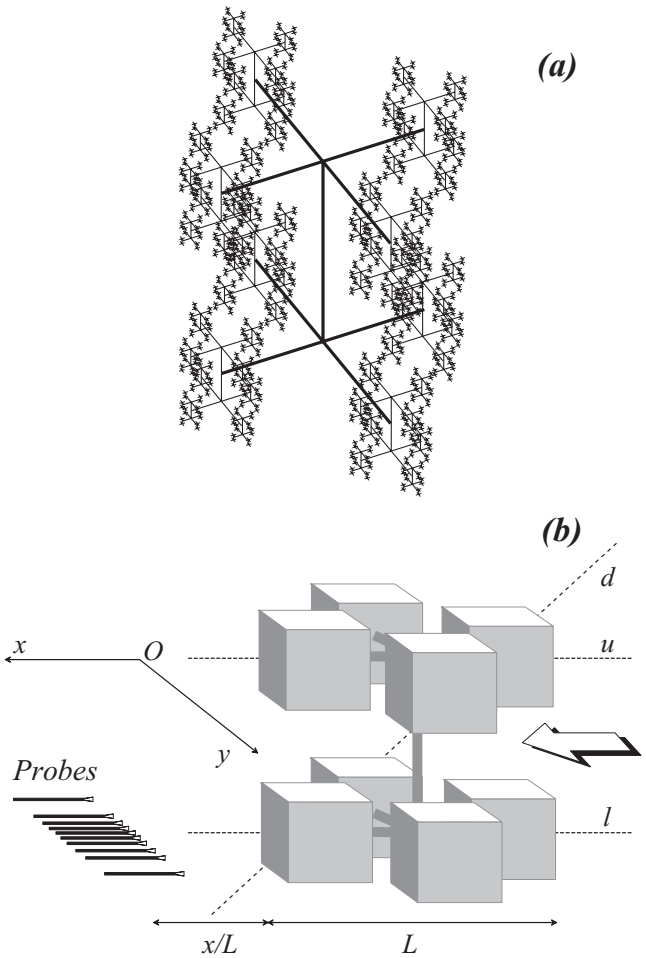

Fig. 7.1: *(a) Schematic representation of the self-similar construction of the fractal objects. (b) Fractal object in a typical measurement configuration. The arrow indicates the direction of the windtunnel flow; the different axes considered are denoted u, l and d. In the actual fractal object shown in (a), the cubes are replaced by self-similar copies of the object. For test purposes, an object without this fractal filling was constructed, which can therefore be viewed as a fractal where the self-similar structure was stopped after one iteration.*

a fixed spatial location are interpreted as space-dependent velocities using Taylor's frozen turbulence hypothesis. The validity of this assumption depends on the turbulence levels u'/U and v'/U (where primes indicate r.m.s. levels). As discussed later in this paper, the violation of the frozen turbulence hypothesis leads to subtle but significant changes of the spectrum at large wave-numbers. If our fractal objects could have infinitely many generations, the stirring of turbulence would be scale invariant at scales well within the size of the object. However, due to the flow reversal problem, the probe array cannot be placed closer to the objects than a distance approximately equal to its size L. Consequently, the largest length scale of the object is always in view, and the flow statistics are unavoidably influenced by the largest scale. This circumstance interferes with the geometrical scaling of the object and is responsible for at least part of the experimental observations, as we argue in the following section.

The large-scale imprint on the flow can be altered by rotating the fractal object with respect to the mean velocity. For example, the primary large-scale iterations of the fractal can be shielded by the smaller-scale iterations by rotating the fractal so that its diagonal axis (axis d in Fig. 7.1b) is oriented parallel to the mean flow's x-direction. A key point of this work is to separate this large-scale imprint from genuine effects of the object's fractal structure, something which [74] did not do. An overview of the experiments is given in table 7.1. Most experiments were done on the objects with fractal dimension D=2.05 and D=2.17. The object with D=2.40, which is more space-filling than the other two, has a very turbulent wake, and to avoid flow reversals, measurements could only be done at relatively large distances from the object, $x/L \geq 3$. In section 7.5 we report the results of experiments on a test object. In order to compare fractal and non-fractal stirring, the test object (see Fig. 7.1b) has the same large-scale structure as the D=2.17 object, but the structure on smaller scales is not filled in: it is a truncated fractal.

In order to study the imprint of the large-scale structure of a single object on the wake, we have done experiments with the D=2.05 object at various orientations with respect to the mean flow and the probe array at two positions relative to the object's geometric center. In the diagonal orientation (axis d in Fig. 7.1b aligned with the mean flow in the x-direction), the projection of the fractal object on a plane perpendicular to the mean flow is more homogeneous. With the velocity probes in the upper position, the support of the fractal is in view (not shown in the figure), therefore, most of the experiments were done behind the lower lobes of the fractal (position l in Fig. 7.1b). The array of velocity sensors was oriented perpendicularly to the mean flow direction and the 10 independent hot-wire sensors were placed such that their 45 distances were distributed approximately exponentially. Consequently, the probes crowd in the center part of

D	x/L	Configuration	Re_λ	u'/U
2.05	1	l	230	0.21
	1.5	d	210	0.13
	2	l	345	0.20
	2	u	370	0.23
	2.8	l	310	0.16
2.17	1	l	175	0.61
	2	l	220	0.34
	2	l	215	0.33
	3	l	250	0.20
2.40	3	l	250	0.43
	5	l	650	0.18
3	1	l	300	0.25
	1.8	l	310	0.16
	2.6	l	315	0.12

Tab. 7.1: *The measurements are grouped depending on the fractal dimension D of the object. For each object, different positions in the turbulent wake are probed, with the letters referring to Fig. 7.1. The object with dimension 3 is a test object that has the same large-scale structure as the D = 2.17 object, but which is truncated after one iteration.*

the array.

Each of the wires used has a sensitive length of 200 μm and was operated by a computerized constant temperature anemometer. The velocity signals were low-pass filtered at 10kHz and sampled synchronously at 20kHz. Each run was preceded by a calibration procedure in which the voltage to air velocity conversion for each wire was measured using a calibrated nozzle. The resulting 10 calibration tables were updated regularly during the run to allow for a (small) temperature increase of the air in our recirculating windtunnel. Adequate statistical convergence was ensured by collecting velocity readings over 6×10^6 integral time scales in runs that lasted approximately 2 hours. Repeated runs gave precise reproduction of measured statistics.

7.3 Dependence on orientation

Our purpose is to unravel the finite-size effect of the fractal stirrer on its turbulent wake from the effect of its scale-invariant structure. As the finite-size effect of the stirrer can be expected to depend on its orientation and position with respect to the velocity sensor, we systematically studied the turbulent wake of one

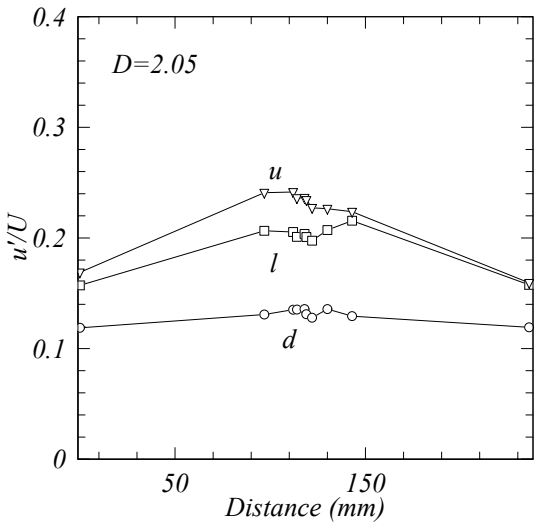

Fig. 7.2: *Turbulence intensity profiles for different configurations of the D=2.05 object, recorded at fixed separation* $x/L = 2$

fractal object (D=2.05) at a fixed separation from that object ($x/L = 2$), but at different orientations and with the velocity probes at different vertical positions relative to the object (l and u). These configurations are schematically indicated in Fig. 7.1b, with the object: diagonal (d), horizontal with the velocity probes behind the upper lobe (u), and horizontal with the velocity probes behind the lower lobe (l). The properties of the turbulent wakes in each of these three configurations is indicated in table 7.1, and the turbulent intensity profiles are drawn in Fig. 7.2. The diagonal orientation has the most homogeneous wake and the lowest turbulence levels but also the smallest turbulence Reynolds number. We conclude that the profiles of the turbulence intensity vary considerably with the orientation of the object.

An overview of the spectra of the u velocity across the wake is given in Fig. 7.3. There is a clear $k^{-5/3}$ scaling range with a bump at low frequencies reflecting the coherent shedding of vortices. A remarkable observation is that the shedding is very weakly pronounced. In the remainder of this paper we only show longitudinal spectra and structure functions from the center wire, where the velocity profile is most homogeneous. Throughout, we normalize all turbulence quantities on dissipation scales, $k^* = k\eta/2\pi$, $E^* = E(f)(2\pi/U)\langle\epsilon\rangle^{-2/3}\eta^{-5/3}$, where η is the Kolmogorov length scale, $\langle\epsilon\rangle$ is the mean dissipation rate and f is the frequency.

The different small k behaviours are more obvious when the spectra are com-

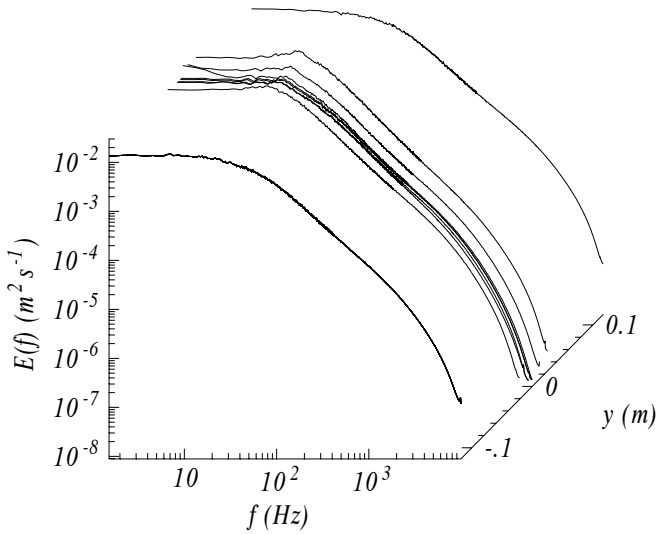

Fig. 7.3: *Turbulence spectra behind fractal object D=2.05 at $x/L = 2$ and configuration l. The low wave number bump in the spectra is more prominent in the central part of the wake.*

pensated by $k^{5/3}$ and plotted in linear-log axes, as in Fig. 7.4. The large-scale region of the spectrum for the object oriented horizontally contains more energy than that for the object oriented diagonally, while all spectra have a well defined scaling region. Spectra show the large-scale contamination of the wakes by the large scales of the object as low-frequency bumps. This large-scale contamination is virtually absent when the object is diagonally orientated, but Re_λ is too small in that orientation to yield a clear scaling range in structure functions, as shown later in this section. For large wave-numbers $k^* \gtrsim 0.1$, the spectra of this object become independent of orientation and position and collapse. Therefore, this part of the spectrum might reflect the intrinsic self-similar structure of the object and may be used to discriminate stirrers with different fractal dimension. This avenue is explored in detail in section 7.4.

The second-order longitudinal structure function $G_2^L(r)$ is the Fourier companion of the longitudinal spectrum. Still, it is useful to present it because we have also access to the transverse second-order structure function $G_2^T(r)$. Combining $G_2^L(r)$ and $G_2^T(r)$ gives access to the anisotropy of the wake. The exponents of the longitudinal structure functions appear to be close to values normally encountered for approximately homogeneous and isotropic turbulence. We obtain $\zeta_2^L = 0.73$, 0.78 and 0.76 for the d, l and u configurations, respectively.

In the customary longitudinal measurement configuration used so far, veloc-

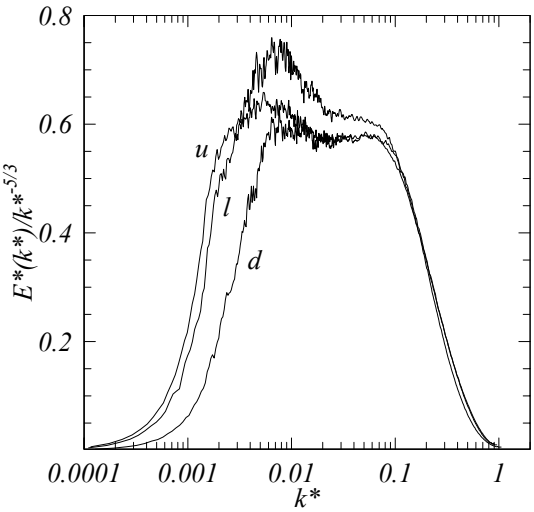

Fig. 7.4: *The compensated longitudinal spectra for different orientations of the D=2.05 object and separation $x/L = 2$. The low wave number peak is more pronounced for configurations u and l.*

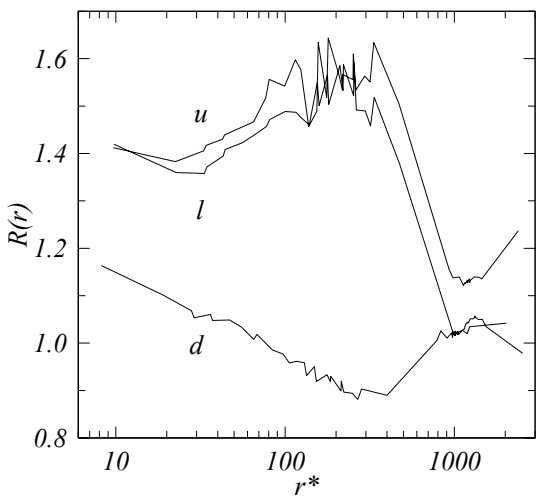

Fig. 7.5: *Anisotropy ratios for different orientations of D=2.05 object, measured at separations close to $x/L = 2$ behind the object.*

ity increments $\Delta u(\mathbf{r})$ are measured over a separation $\mathbf{r}$, where $\mathbf{r}$ points in the same direction as the measured velocity component u. Separations r then follow from time delays τ by invoking Taylor's frozen turbulence hypothesis $r = U\tau$. When the turbulence inhomogeneity across the wake is not too large, it is possible to measure the transverse structure functions with the true separation vector $\mathbf{r}$ oriented perpendicularly to U. The transverse second-order structure function scaling exponent is higher for the more inhomogeneous u configuration ($\zeta_2^T \sim 0.80$), while for orientation d there is no clear indication of a scaling range because the Reynolds number is too small in that case.

In isotropic turbulence the transverse and longitudinal structure functions are related through

$$\tilde{G}_2^T = G_2^L + \frac{r}{2}\frac{\mathrm{d}G_2^L}{\mathrm{d}r} \tag{7.1}$$

The ratio $R(r) = G_2^T/\tilde{G}_2^T$ between the directly measured G_2^T and the one computed using Eq. 7.1 is a measure of the anisotropy. Figure 7.5 shows the anisotropy of the wake for the three configurations used. As we use the u component in both longitudinal and transverse structure functions, $R(r)$ is trivially 1 for large r in homogeneous turbulence. The relatively large fluctuations of $R(r)$ in the u configuration are not due to lack of statistics, but are a consequence of the flow inhomogeneity across the wake. The horizontal axis of Fig. 7.5 corresponds to separations $y_i - y_j$ between probes, where y_i and y_j are the locations of the probes. Separations $y_i - y_j$ may be close to separations $y_k - y_l$, but the probes may be in very different regions of the wake. In the diagonal configuration the wake is more homogeneous and the fluctuations in $R(r)$ are smaller.

The third order longitudinal structure functions shown in Fig. 7.6 have scaling exponents around 1; the non-homogeneous configurations give ζ_3^L larger than 1, ~ 1.13 and 1.2 for the u and l positions, respectively, while d has $\zeta_3^L \sim 0.9$. Obviously, the small Reynolds number of the d configuration results in poor scaling of G_3^L. In the two horizontal configurations, one interpretation of the results might be that the large-scale energy transfer is enhanced thus leading to an apparent scaling exponent which is significantly larger than unity.

7.4 Comparison of D=2.05 and D=2.17 fractal objects

After having exposed the influence of the large-scale structure of the objects on their wake, let us now systematically compare the (apparent) inertial range scaling behaviour of the turbulent wakes of two objects, one with fractal dimension D=2.05 and one with D=2.17.

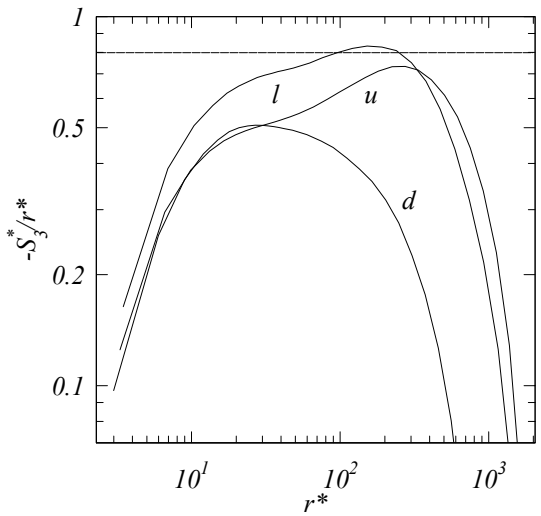

Fig. 7.6: *Third-order structure functions for different orientations of the D=2.05 object at separation $x/L = 2$. Non-homogeneous configurations l and d yield apparent scaling exponents larger than one. The horizontal line compares these results with the $S_3(r) = -4/5\langle\epsilon\rangle r$ Kolmogorov prediction.*

We do this by presenting spectra, turbulent intensities and third-order structure functions for increasing separations x/L behind each object at a single orientation l, which was chosen because its Reynolds number was typically a factor of 2 larger than for the more homogeneous diagonal configuration d, and because it was least influenced by the support of the fractal object. For the object with fractal dimension D=2.05, these distances are x/L =1, 2 and 2.8, while for the D=2.17 case we have x/L =1, 2 and 3. The D=2.17 object is smaller (L = 26cm) than the one with D=2.05 (L = 37cm). The turbulence intensity in the wakes of these two objects is shown in Fig. 7.7. Although the difference in fractal dimension of the two objects is small, Fig. 7.7 demonstrates that their wakes are very different. Close to the object at $x/L = 1$, the wake of the D=2.17 object is much more strongly turbulent and more inhomogeneous than that of the D=2.05 object. A remarkable difference is also the way in which the turbulence intensity decreases with increasing distance: the turbulence intensity behind the D=2.17 object decreases much faster with increasing distance, seen in Fig. 7.7.

The evolution of the energy spectra with increasing distance form the objects is shown in Fig. 7.8. The energy spectrum corresponding to the D=2.17 object has a strong x/L dependence in the range $1 \leq x/L \leq 3$ which is absent in the wake of the D=2.05 object.

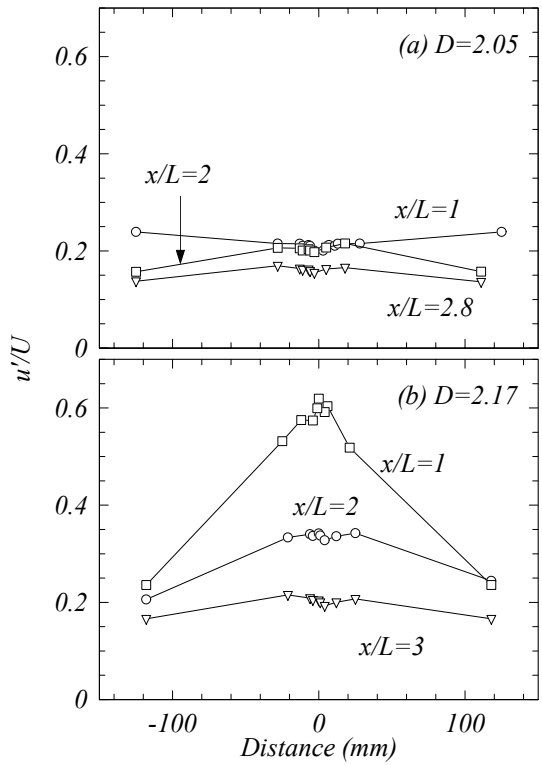

Fig. 7.7: *Turbulence intensity profiles for the (a) D=2.05 object and (b) D=2.17 object at different separations x/L, all for the same configuration l (see Fig. 7.1b). The intensity of the turbulent wakes produced by the the D=2.17 object grows significantly stronger as we move closer to the object.*

Not only does the D=2.17 object create stronger turbulence (Fig. 7.7), but it also distributes the turbulent energy over the scales in a different manner. Whilst at small x/L separations the spectrum of the D=2.05 object has a clear $k^{-5/3}$ scaling, that of the D=2.17 object has an apparent $E(k) \sim k^{-\alpha}$, with $\alpha > 5/3$. Alternatively, the enhancement of $E(k)$ at small k of the D=2.17 spectrum may be due to the influence of large-scale shedding. We have checked that, in spite of the high turbulence intensities, minimal flow reversals occur at separation $x/L = 1$, while at $x/L = 2$ behind the D=2.17 object they are absent (flow reversals are also not occurring at all other positions behind both objects where measurements are reported and the turbulence intensity is of the order of 20 %).

Despite the relatively small size of the objects and the relatively small Reynolds numbers of their wakes, the third-order longitudinal structure functions

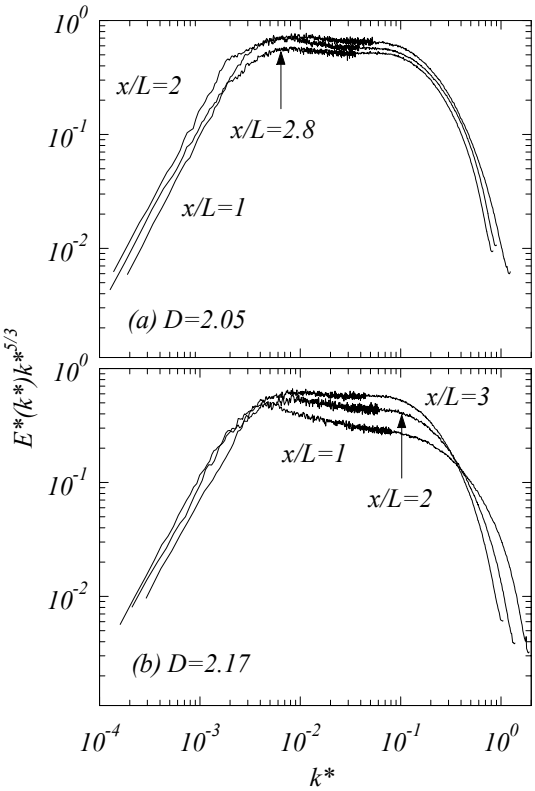

Fig. 7.8: *Comparison between compensated longitudinal spectra for 2 fractal objects (a) for the D=2.05 object and (b) for the 2.17 object. The measurements are done in the lower l configuration at different separations behind the object.*

in Fig. 7.9 show clear scaling behaviour. For the D=2.17 object, the longitudinal $G_3^L(r)$ shows a marked dependence on the distance x/L of the probe array to the fractal object. The scaling behaviour of the wake behind the D=2.17 object apparently changes with distance x/L. Such a change is virtually absent for the D=2.05 object and may be interpreted as a direct influence of the scaling properties of the object on the scaling properties of its wake. A caveat, however, is the small spectral gap which may give rise to a contamination of inertial range behaviour by large scales, that is the large-scale structure of the object. This contamination may be present in the spectra in Fig. 7.8 and may also affect G_3^L. This is suggestively illustrated in Fig. 7.10, where we plot side by side $G_3^L(r^*)$, and the energy spectrum as a function of $1/k^*$. It is seen that G_3^L shows similar structure at the same values $1/k^*$ as the spectrum. We conclude that the change of scaling

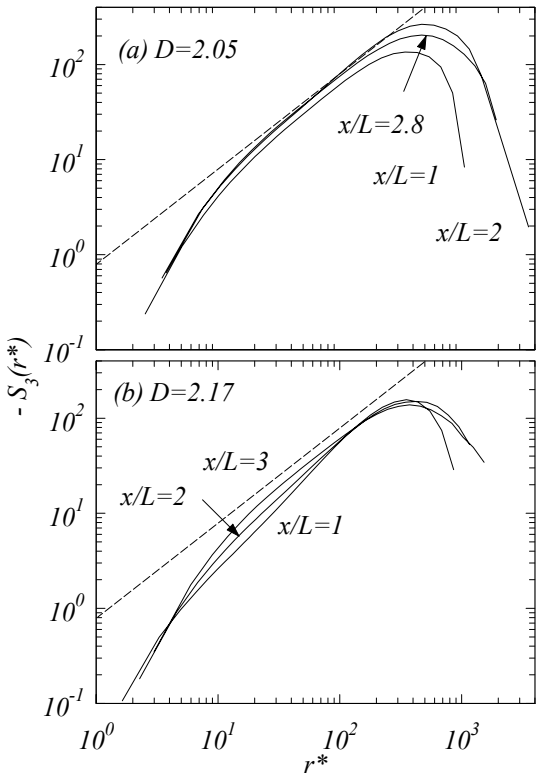

Fig. 7.9: *Third-order structure functions measured for 2 fractal objects in configuration l at different separations x/L, (a) for the D=2.05 object and (b) for the D=2.17 fractal object.*

behaviour with the fractal dimension of the object should be interpreted with great caution.

In section 7.3, we have seen that the dissipation range of the spectrum is independent of the object's orientation and thus independent of the large-scale structure of the object. In figure 7.11 we plot the spectra of the wakes for the D=2.05 and D=2.17 objects for various distances x/L. The plot is done such as to emphasize the approximate exponential behaviour of the spectrum for dissipative scales $E^*(k^*) \sim \exp -\beta k^*$. This well-known exponential behaviour can be explained by assuming a linear relation between the energy and its dissipation [70]. In various experiments [77], the exponent β was found to be $\beta \simeq 5.3$. Figure 7.11 shows a striking difference between the two objects. Whereas the exponent β remains close to 5.3 for all separations for the D=2.05 object, it depends strongly on x/L for the D=2.17 case. Perhaps this is a direct effect of the object's fractal dimension, but now on dissipative scales.

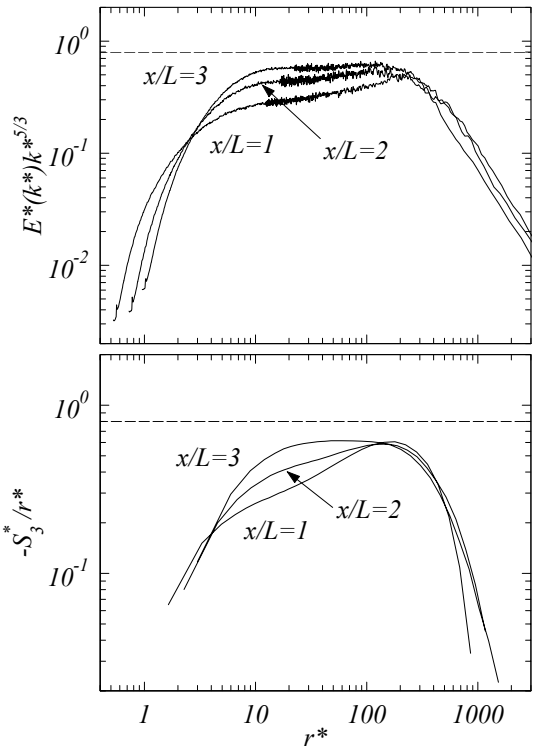

Fig. 7.10: *Third-order compensated structure functions and longitudinal compensated spectra for the D=2.17 object. The horizontal axis of the spectra is shown as a function of* $1/k^*$.

An important caveat is that, with x/L, the turbulence intensity changes too. As is evident from table 7.1, this change is much stronger for the D=2.17 object than for the D=2.05 object, where u'/U is approximately independent of x/L.

We interpret measured spectra as wave number spectra through invocation of Taylor's hypothesis. As stated in section 7.1 this assumption is challenged more strongly when the turbulence intensity increases. A first correction to the measured spectra arises from the fluctuating part u'/U of the velocity in translating time into space $x = (U + u')\tau$. Due to fluctuations of the advection velocity, the velocity is no longer sampled equidistantly in space and high wave number corrections result. Assuming isotropic spectra, these corrections were worked out in [38] to first order in u'^2/U^2, for a measured spectrum with an exponential tail $e^{-\beta k^*}$

$$E^{real}(k^*) = \left[1 - \frac{1}{2}\left(\frac{u'}{U}\right)^2\left(\frac{22}{9} + \frac{10}{3}\beta k^* + (\beta k^*)^2\right)\right] E^{meas}(k^*) \qquad (7.2)$$

where E^{real} is the underlying true spatial spectrum and E^{meas} is the measured spec-

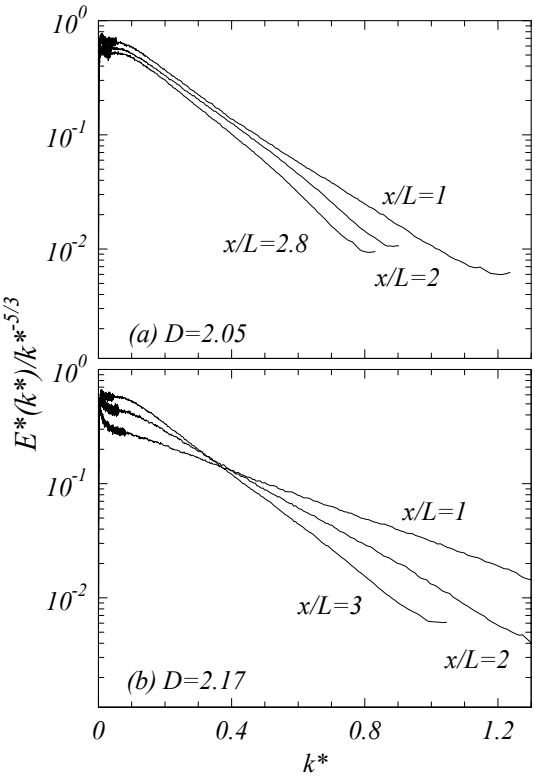

Fig. 7.11: *Dissipative tails of the energy spectra for (a) D=2.05 object and (b) D=2.17 object measured for configuration l and different separations x/L. The log-linear plot emphasizes the approximate exponential behaviour of turbulence spectra tails $E^*(k^*) \sim exp-\beta k^*$.*

trum through the use of Taylor's hypothesis [1]. Assuming an underlying spectrum $E^{real}(k^*)$ with a shape that does not change with the turbulent intensity u'/U, Eq.7.2 predicts that the shape of the measured spectrum $E^{meas}(k^*)$ depends on the turbulence intensity. Actually, this dependence is such that the measured β *decreases* with increasing intensity, just as is observed in Fig. 7.11. In Fig. 7.12 we assume a real spectrum with $E(k^*) \sim e^{-5.3k^*}$, compute its appearance in the turbulence levels encountered in our experiment and compare it to the actually measured spectra. It appears that Eq. 7.2 can explain the measured dependence of β on u'/U albeit qualitatively rather than quantitatively. It must be noted, however, that the turbulence level in our experiment can be as high as 60%, whereas Eq. 7.2 is only first order in $(u'/U)^2$.

[1] This relation holds for the one-dimensional projection of the spectrum

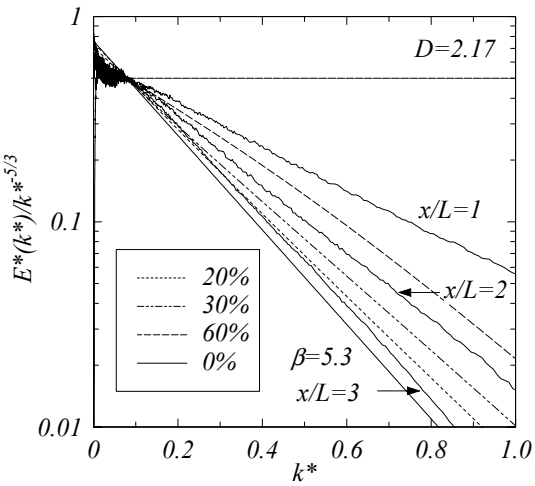

Fig. 7.12: *Comparison between the measured spectra tails for the D=2.17 object and effects of correction to the Taylor hypothesis. Full lines: measured spectra at* $x/L = 1$ *(turbulence intensity* $u'/U = 61\%$*), ,* $x/L = 2$ *(*$u'/U = 34\%$*) and* $x/L = 3$ *(*$u'/U = 20\%$*). Dashed lines: spectra computed from Eq. 7.2 by assuming an underlying spectrum* $E^*(k^*) \sim \exp -\beta k^*$ *with* $\beta = 5.3$ *at various turbulence intensities.*

These observations make it difficult to establish a direct relation between the dissipative properties of the wake and the fractal dimension of the object, other than a trivial effect of the increased turbulence intensity.

7.5 Turbulent wake of a truncated fractal

In the previous section we compared the turbulent wakes of two fractal objects that had different fractal dimensions. We found significant differences between the wakes shed off these different fractal dimensions. A much cruder test is to compare these wakes to the wake shed by a non-fractal object. To this aim we constructed an object that has the same large scale structure as the D=2.17 object, but that lacks its fractal structure, *i.e.* we stopped at the first iteration of the self-similar refinement. The large-scale dimensions of this object are the same as those of the D=2.17 fractal.

We studied the turbulent wake of this object through turbulence measurements similar to those performed on fractals. Accordingly, its scaling properties were investigated in the configuration l, at varying separations behind the object $x/L = 1, 1.8$ and 2.6.

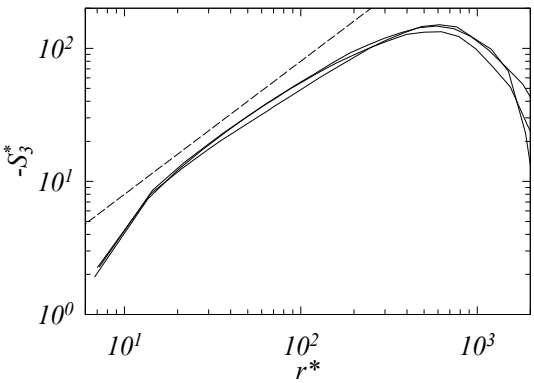

Fig. 7.13: *Third order longitudinal structure functions measured in the wake of a truncated fractal at separations $x/L = 1, 1.6$ and 2.6 in configuration l. The dashed line is the $-(4/5)r^*$ exact result for isotropic and homogeneous turbulence.*

The charactersitics of the turbulent wakes are listed in Table 7.1; whilst the Reynolds numbers are comparable to those of the fractal objects, the turbulence intensities are smaller. This clearly demonstrates that it is not their large-scale structure that makes fractal objects better turbulence generators, but their (self-similar) refinement of length scales.

The inertial range scaling properties of the wake of the truncated fractal object are very different from those of the true fractal object. The third-order structure functions, shown in Fig. 7.13 no longer depend on the x/L separation and now have an apparent slope *less* than 1, compared to the structure functions in Fig. 7.9b. In Fig. 7.14 we compare the large wavenumber behaviour of the longitudinal spectra for three positions x/L in the wake of the truncated fractal object. These positions are comparable to those used for the self-similar fractal objects in Fig. 7.11. As for the third-order structure functions, also the dissipative tails of the spectra now become independent of the separation x/L. This can only partly be explained by the reduced turbulence intensities of the truncated fractal wake, which range from $u'/U = 0.25$, at the smallest separation $x/L = 1$, to $u'/U = 0.12$ at $x/L = 2.6$.

7.6 Conclusions

We can clearly distinguish between the scaling properties of turbulence stirred by a fractal object that has a range of refined scales and that of a truncated fractal. However, for self-similar fractals we found it difficult to conclude a relation be-

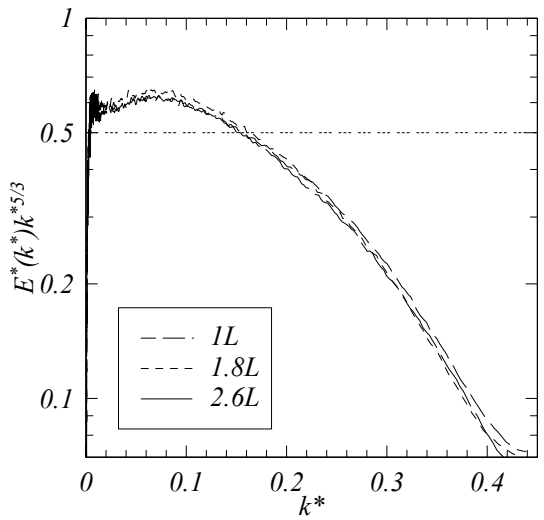

Fig. 7.14: *Large wavenumber tails for the turbulent wake of a truncated fractal, measured in configuration l at three increasing separations $x/L =$ 1, 1.6 and 2.6, as indicated in the legend.*

tween the dimension of the object (which quantifies the manner of refinement) and the scaling properties of the turbulent wake.

We have observed suggestive effects in the measured spectra and structure functions, but they could not be firmly distinguished from the influence of the finite size of the objects. In order to achieve such clear distinction we need larger Reynolds numbers and/or larger fractal objects that fill the windtunnel cross-section. In this respect, it is interesting to point to recent work where a plane grid with a few scales (but not a fractal) was found to produce high Reynolds numbers ([68]).

Whilst we may not have yet achieved our goal, we have found a few remarkable large-scale properties of wakes shed by fractal objects. Vortex shedding off fractal objects has a very weakly pronounced energy spectrum signature. It is even possible to rotate the fractal objects so as to nearly fully inhibit this vortex shedding signature but at the cost of very significantly lowering the Reynolds number of the turbulence in the wake. In our experiment, such an orientation had the effect of somehow shielding the largest scale features of the fractals and resulted in a Reynolds number too low for a well-defined scaling range to be seen in the third order longitudinal structure function. It is puzzling, however, that the energy spectrum of the lowest fractal dimension object (D=2.05) in that orientation does exhibit a decade of fairly well-defined $k^{-5/3}$ scaling.

We gratefully acknowledge financial support by the “Nederlandse Organ-

isatie voor Wetenschappelijk Onderzoek (NWO)" and "Stichting Fundamenteel Onderzoek der Materie (FOM)". We are indebted to Gerard Trines, Ad Holten and Gerald Oerlemans for technical assistance. JCV acknowledges the support of the Royal Society.

SAMENVATTING

Turbulentie is de chaotische, onvoorspelbare en scherp onregelmatige dynamiek die we in elk stroming kunnen aantreffen. Zijn structuur en onverwachte manier van optreden is het gevolg van complexe dynamica met heel verschillende schalen, die zich van microns, in turbulente plasmas, tot duizenden lichtjaren in spiraalvormige melkwegstelsels uitstrekken. De beschrijving van turbulentie blijft, tot nu toe, een raadsel: het is niet mogelijk om gesloten vergelijkingen voor de statistische eigenschapen van de fluctuerende vloeistof af te leiden. Daarom wordt turbulentie soms ook het laatste onopgeloste probleem van de klassieke natuurkunde genoemd.

Beginend met het pionierwerk van A.N. Kolmogorov in 1941, trok de *universaliteit* van stationaire turbulentie de aandacht van de natuurkunde. Zijn beroemde gelijksvormigheidshypotheses blijven ook vandaag de dag de meest opmerkelijke bijdragen aan de statistische beschrijving van turbulentie. Ze zijn, ondanks discrepanties en verfijningen nog steeds wel gefundeerd in de turbulentie gemeenschap.

In de laatste jaren, worden nieuwerwetse concepten van wiskundige oorsprong, zoals representaties van Lie groepen, fractale modellen en de theorie van grote deviaties, van wiskundige oorsprong, toenemend toegepast als grensverleggende non-klassieke hulpmiddelen. Ze vormen een alternatieve statistische beschrijving van turbulentie. De taak van het experimentele werk die hier wordt gepresenteerd is niet alleen om grondig de voorspellingen van zulke modellen met reele stromingen te vergelijken, maar dan ook om de richtingen aan te duiden voor nadere onderzoek. Om dit doel te behalen, wij hebben experimenten verricht, met nadruk op de geometrische eigenschappen van de kleine schalen van turbulentie, die een nieuwlicht werpen op de oorsprong van het *intermittentie* verschijnsel.

De experimenten werden in de windtunnel faciliteit van de TU/e uitgevoerd. Wij hebben de techniek van lijn-sensoren, bedoeld om turbulente snelheidsvelden te meten, verbeterd, terwijl de experimentomstandigheden geoptimaliseerd werden, door ontwerp van nieuwe turbulentie generatoren. Multipele hetedraad anemometrie werd als meettechniek gebruikt om in verschillende turbulente stromingen lange tijdreeksen van de snel varieerende snelheidsvelden op

te nemen. Roosters met een innovatief ontwerp werden gebruikt om de aanvankelijk laminaire windtunnel stroming te beroeren, zodat de resulterende stationaire turbulente stroming de juiste karakteristieken heeft.

Het proefschrift omvat verschillende onderwerpen, zoals de invloed van fractale generators op de intieme structuur van turbulentie, schalingseigenschappen van structuurfuncties in homogeen afgeschoven turbulentie en decompositie van vrijwel-isotropische turbulentie in niet vereenvoudigbare representaties van de SO(3) rotatie-groep.

SUMMARY

Turbulence is the chaotic, unpredictable and sharply irregular motion that can be encountered in any fluid. Its structure and unpredictable behaviour involves complex dynamics of very different scales, ranging from microns in turbulent plasmas up to thousands of light-years in spiral galaxies. The description of turbulence remains a conundrum: it is not possible to arrive at closed equations for the statistical properties of the fluctuating flow. Turbulence is therefore sometimes called the last unsolved problem of classical physics.

Starting with the pioneering work of A.N. Kolmogorov in 1941, the *universality* of stationary turbulence came to the attention of physics. His famous similarity hypotheses still remain today the most remarkable contributions to the statistical description of turbulence, although deviations and refinements of the original formulations are well-established in the turbulence research community.

In recent years, modern mathematical concepts, such as representations of Lie groups, fractal models and the theory of large deviations, are increasingly used as innovative, non-classical tools trying to provide alternative descriptions and new models of turbulence. The task of the experimental work presented in this thesis is not only to thoroughly confront predictions of such models with real flows, but also to indicate the directions in which the research interests should develop and focus. In order to achieve this goal, we perform experiments with special emphasis on the geometrical properties of the small scales of turbulence, which shed new light on the origins of the phenomenon of *intermittency*.

The experiments were performed in the windtunnel facility of the TU/e. We have perfected the technique of array sensors to measure the turbulent velocity fields, whereas the conditions of the experiments were optimized by designing new turbulence generators. Multiple hot-wire anemometry is used as measurement technique to sample simultaneously in high Reynolds-number turbulence very long time-series of the fast-varying velocity fields in different types of flows. Grids of innovative design are used to stir the initially laminar flow of the windtunnel, resulting in stationary turbulent flows with finely-tuned properties.

The thesis covers subjects as the influence of fractal generators on the inner structure of turbulence, scaling properties of the structure functions in homogeneous sheared turbulence and decomposition of the near-isotropic turbulence on

irreducible representations of the SO(3) rotation group.

BIBLIOGRAPHY

[1] A. Celani, A. Lanotte, A. M., and Vergassola, M. Fronts in passive scalar turbulence. *Phys. Fluids 13*, 6 (June 2001), 1768–1783.

[2] Antonia, R. A., and Pearson, B. Effect of initial conditions on the mean energy dissipation rate and the scaling exponent. *Flow, Turbul. Combust. 64* (2000), 95–117.

[3] Antonov, N. V., Vasiliev, A. N., Millard, P., and Adzhemyan, L. T. *Field Theoretic Renormalization Group in Fully Developed Turbulence*. Taylor and Francis, 1999.

[4] Arad, I., Dhruva, B., Kurien, S., L'vov, V. S., Procaccia, I., and Sreenivasan, K. R. Extraction of anisotropic contributions in turbulent flows. *Phys. Rev. Lett. 81*, 24 (December 1998), 5330–5333.

[5] Arad, I., L'vov, V. S., and Procaccia, I. Correlation functions in isotropic and anisotropic turbulence: The role of the symmetry group. *Phys. Rev. E 59*, 6 (June 1999), 6753–6765.

[6] Arneodo, A., Baudet, C., Belin, F., Benzi, R., Castaing, B., Chabaud, B., Chavarria, R., Ciliberto, S., Camussi, R., Chilla, F., B.Dubrulle, Gagne, Y., Hebral, B., Herweijer, J., Marchand, M., Maurer, J., Muzy, J., Naert, A., Noullez, A., Peinke, J., Roux, F., Tabeling, P., van de Water, W., and Willaime, H. Structure functions in turbulence, in various flow configurations, at Reynolds number between 30 and 5000, using extended self-similarity. *Europhys. Lett. 34*, 6 (May 1996), 411–416.

[7] Atta, C. W. V., and Antonia, R. A. Reynolds number dependence of skewness and flatness factors of turbulent velocity derivatives. *Phys. Fluids 23*, 2 (February 1980), 252–257.

[8] Balkovsky, E., and Lebedev, V. Instanton for the Kraichnan passive scalar problem. *Phys. Rev. E 58*, 5 (November 1998), 5576–5795.

[9] Belin, F., Maurer, J., Tabeling, P., and Willaime, H. Observation of intense filaments in fully developed turbulence. *J. Phys. Paris II 6* (1996), 573–584.

[10] Benzi, R., Ciliberto, S., Tripiccione, R., Baudet, C., Massaioli, F., and Succi, S. Extended self-similarity in turbulent flows. *Phys. Rev. E*, 48 (1993), 29.

[11] Biferale, L., and Toschi, F. Anisotropic homogeneous turbulence: Hierarchy and intermittency of scaling exponents in the anisotropic sectors. *Phys. Rev. Lett. 86*, 21 (May 2001), 4831–4834.

[12] Boratav, O. On longitudinal and lateral moment hierarchy in turbulence. *Phys. Fluids 9*, 11 (November 1997), 3120–3122.

[13] Bruun, H. *Hot-wire anemometry*. Oxford University Press, New York, 1995.

[14] Cambon, C., and Teissedre, C. Application of spherical harmonics to representation and computation of the kinematic field for an homogeneous anisotropic turbulence. *Comptes rendus de l'Academie des Sciences, Serie II 301*, 2 (June 1985), 65–68.

[15] Camussi, R., and Guj, G. Orthonormal wavelet decomposition of turbulent flows: intermittency and coherent structures. *J. Fluid Mech. 348* (1997), 177–199.

[16] Camussi, R., and Guj, G. Experimental analysis of intermittent coherent structures in the near field of a high Re turbulent jet flow. *Phys. Fluids 11*, 2 (February 1999), 423–431.

[17] Celani, A., Lanotte, A., Mazzino, A., and Vergassola, M. Universality and saturation of intermittency in passive scalar turbulence. *Phys. Rev. Lett. 84*, 11 (March 2000), 2385–2388.

[18] Chen, S., Sreenivasan, K. R., and Nelkin, M. Inertial range scalings of dissipation and enstrophy in isotropic turbulence. *Phys. Rev. Lett. 79*, 7 (1997), 1253–1256.

[19] Chen, S., Sreenivasan, K. R., Nelkin, M., and Cao, N. Refined similarity hypothesis for transverse structure functions in fluid turbulence. *Phys. Rev. Lett. 79*, 12 (September 1997), 2253–2256.

[20] Chertkov, M. Instanton for random advection. *Phys. Rev. E 55*, 3 (March 1997), 2272–2735.

[21] Comte-Bellot, G., and Corrsin, S. The use of a contraction to improve to isotropy of grid-generated turbulence. *J. Fluid Mech. 25* (1966), 657–682.

[22] Comte-Bellot, G., and Corrsin, S. Simple eulerian time correlation of full- and narrow-band velocity signals in grid-generated, 'isotropic' turbulence. *J. Fluid Mech. 48* (1970), 273–337.

[23] Corrsin, S., and Kovasznay, L. S. G. On the hot-wire length correction. *Phys. Rev. 75*, 12 (June 1949), 1954.

[24] Dhruva, B., Tsuji, Y., and Sreenivasan, K. R. Transverse structure functions in high-Reynolds-number turbulence. *Phys. Rev. E 56*, 5 (November 1997), R4928–R4930.

[25] Dimotakis, P. The mixing transition in turbulent flows. *J. Fluid Mech. 409* (2000), 69–98.

[26] Douady, S., Couder, Y., and Brachet, P. Direct observation of the intermittency of intense vorticity filaments in turbulence. *Phys. Rev. Lett. 67* (1991), 983–986.

[27] Emsellem, V., Kadanoff, L. P., Lohse, D., Tabeling, P., and Wang, Z. J. Transitions and probes in turbulent helium. *Phys. Rev. E 55* (March 1997), 2672–2681.

[28] F. H. Champagne, V. G. H., and Corrsin, S. Experiments on nearly homogeneous turbulent shear flow. *J. Fluid Mech. 41* (1970), 81.

[29] F. Moisy, H. Willaime, J. S. A., and Tabeling, P. Passive scalar intermittency in low temperature helium flows. *Phys. Rev. Lett. 86*, 21 (2001), 4827–4830.

[30] Farge, M. Wavelet transforms and their applications to turbulence. *Annu. Rev. Fluid Mech. 24* (1992), 395–457.

[31] Ferchichi, M., and Tavoularis, S. Reynolds number effects on the fine structure of uniformly sheared turbulence. *Phys. Fluids 12*, 11 (2000), 2942–2953.

[32] Feynman, R. P. *The Feynman lectures on physics II*. Addison-Wesley, 1963.

[33] Frenkiel, F. Erratum: The influence of the length of a hot wire on the measurements of turbulence. *Phys. Rev. 76*, 5 (September 1949), 686.

[34] Frenkiel, F. The influence of the length of a hot wire on the measurements of turbulence. *Phys. Rev. 75*, 8 (April 1949), 1263–1264.

[35] Frisch, U. *Turbulence: The legacy of A.N. Kolmogorov*. Cambridge University Press, Cambridge, 1995.

[36] Fung, J., Hunt, J., Malik, N., and Perkins, R. Kinematic simulation of homogeneous turbulent flows generated by unsteady random Fourier modes. *J. Fluid Mech. 236* (1992), 281–318.

[37] Garg, S., and Warhaft, Z. On the small scale structure of simple shear flow. *Phys. Fluids 10*, 3 (March 1998), 662–673.

[38] Gledzer, E. On the Taylor hypothesis corrections for measured energy spectra of turbulence. *Physica D 104*, 2 (1997), 163–183.

[39] Gledzer, E., Villermaux, E., Kahalerras, H., and Gagne, Y. On the log-Poisson statistics of the energy dissipation field and related problems of developed turbulence. *Phys. Fluids 8*, 12 (December 1996), 3367–3378.

[40] Grossmann, S., and Lohse, D. Universality in fully developed turbulence. *Phys. Rev. E 50*, 4 (October 1994), 2784–2789.

[41] Grossmann, S., Lohse, D., and Reeh, A. Application of extended self-similarity in turbulence. *Phys. Rev. E 56*, 5 (November 1997), 5473–5478.

[42] Harris, V. G., Graham, J. A., and Corrsin, S. Further experiments in nearly homogeneous turbulent shear flow. *J. Fluid Mech. 81* (1977), 657.

[43] Hatakeyama, N., and Kambe, T. Statistical laws of random strained vortices in turbulence. *Phys. Rev. Lett. 79*, 7 (August 1997), 1257–1260.

[44] He, G., Chen, S., Kraichnan, R., Zhang, R., and Zhou, Y. Statistics of dissipation and enstrophy induced by localized vortices. *Phys. Rev. Lett. 81*, 21 (November 1998), 4636–4639.

[45] Hinze, J. *Turbulence*. McGraw-Hill, 1959.

[46] J. Jiménez, A. A. Wray, P. G. S., and Rogallo, R. S. The structure of intense vorticity in isotropic turbulence. *J. Fluid Mech. 255* (1993), 65–90.

[47] Jones, M. N. *Spherical harmonics and tensors for classical field theory*. Research Studies Press; Wiley, Letchword; Chichester, 1985.

[48] Kolmogorov, A. The local structure of turbulence in incompressible viscous fluid flow for very large Reynolds numbers. *Dokl. Akad. Nauk. 26* (1941), 115. Reprinted in Proc. Roy. Soc. London, Ser. A **434**, 9-13 (1991).

[49] Kolmogorov, A. A refinement of previous hypothesis concerning the local structure of turbulence in incompressible viscous fluid at high Reynolds number. *J. Fluid Mech. 13* (1962), 82–85.

[50] Kurien, S., L'vov, V. S., Procaccia, I., and Sreenivasan, K. R. Scaling structure of the velocity statistics in atmospheric boundary layers. *Phys. Rev. E 61*, 1 (January 2000), 407–421.

[51] Kurien, S., and Sreenivasan, K. R. Anisotropic scaling contributions to high-order structure functions in high-Reynolds-number turbulence. *Phys. Rev. E 62*, 2 (August 2000), 2206–2212.

[52] Landau, L., and Lifshitz, E. *Fluid mechanics*, 2nd ed. Pergamon Press, Oxford, 1987.

[53] Lumley, J. Similarity and the turbulent energy speatrum. *Phys. Fluids 10*, 1 (April 1967), 855–858.

[54] Lumley, J. L. Similarity and the turbulent energy spectrum. *Phys. Fluids 10* (1967), 855.

[55] Lvov, V. S., Podivilov, E., and Procaccia, I. Invariants for correlations of velocity differences in turbulent fields. *Phys. Rev. Lett. 79*, 11 (September 1997), 2050–2052.

[56] Moffat, H., Kida, S., and Ohkitani, H. Streched vortices –the sinews of turbulence; large-Reynolds-number-asymptotics. *J. Fluid Mech. 259* (1994), 241.

[57] Moisy, F., Tabeling, P., and Willaime, H. Kolmogorov equation in a fully developed turbulence experiment. *Phys. Rev. Lett. 82*, 20 (May 1999), 3994–3997.

[58] Mouri, H., Hori, A., and Kawashima, Y. Vortex tubes in velocity fields of laboratory isotropic turbulence. *Phys. Lett. A 276* (October 2000), 115–221.

[59] Mouri, H., Takaoka, M., and Kubotani, H. Wavelet identification of vortex tubes in a turbulence velocity field. *Phys. Lett. A 261* (October 1999), 82–88.

[60] Mydlarski, L., and Warhaft, Z. On the onset of high-Reynolds-number grid generated wind tunnel turbulence. *J. Fluid Mech. 320* (1996), 331.

[61] Noullez, A., Wallace, G., Lempert, W., Miles, R., and Frisch, U. Transverse velocity increments in turbulent flow using the relief technique. *J. Fluid Mech. 339* (1997), 287–307.

[62] Novikov, A. *Zh. Eksp. Theor. Fiz. 47* (1964), 1919.

[63] Okkels, F., Mazzi, B., and Vassilicos, J. A shell-model approach to fractal-induced turbulence. *Eur. Phys. B 28* (2002), 243–251.

[64] P. Chainais, P. A., and Pinton, J. Intermittency and coherent structures in a swirling flow: A wavelet analysis of joint pressure and velocity measurements. *Phys. Fluids 11*, 11 (July 1999), 3524–3539.

[65] Pao, Y. Structure of turbulent velocity and scalar fields at large wavenumbers. *Phys. Fluids 8* (1965), 1063–1065.

[66] Parisi, G., and Frisch, U. A multifractal model of intermittency. In *Turbulence and predictability in geophysical fluid dynamics and climate dynamics*, M.Ghil, R. Benzi, and G. Parisi, Eds. North Holland, Amsterdam, 1985, pp. 84–87.

[67] Pearson, B. unpublished, 2001.

[68] Pearson, B., Krogstad, P.-A., and van de Water, W. Measurements of the turbulent energy dissipation rate. *Phys. Fluids 14*, 3 (March 2002), 1288–1290.

[69] Perry, A. *Hot-wire anemometry*. Clarendon Press, Oxford, 1982.

[70] Pope, S. *Turbulent Flows*. Cambridge University Press, 2000.

[71] Porta, A. L., Voth, G. A., Crawford, A. M., Alexander, J., and Bodeschatz, E. Fluid particle accelerations in fully developed turbulence. *Nature 409* (2001), 1017–1019.

[72] Procaccia, I., Ching, E. S. C., Constantin, P., Kadanoff, L. P., Libchaber, A., and Wu, X.-Z. Transitions in convective turbulence: The role of thermal plumes. *Phys. Rev. A 12* (December 1991), 8091–8102.

[73] Pumir, A. Turbulence in homogeneous shear flows. *Phys. Fluids 8* (1996), 3112.

[74] Queiros-Conde, D., and Vassilicos, J. Turbulent wakes of 3D fractal grids. In *Intermittency in turbulent flows*, J. Vassilicos, Ed. Cambridge University Press, 2001, pp. 136–167.

[75] Richardson, L. *Weather prediction by numerical process*. Cambridge University Press, England, 1922.

[76] Rose, W. G. Results of an attempt to generate a homogeneous turbulent shear flow. *J. Fluid Mech. 25* (1966), 97.

[77] Saddoughi, S. G., and Veeravali, S. V. Local isotropy in turbulent boundary layers at high Reynolds number. *J. Fluid Mech. 268* (1994), 333–372.

[78] Saffman, P., and Pullin, D. Calculation of velocity structure functions for vortex models of isotropic turbulence. *Phys. Fluids 8*, 11 (November 1996), 3072–3084.

[79] She, Z. S., Jackson, E., and Orszag, S. A. Intermittent vortex structure in homogeneous isotropic turbulence. *Nature 144* (1991), 226–228.

[80] She, Z.-S., and Leveque, E. Universal scaling laws in fully developed turbulence. *Phys. Rev. Lett. 72*, 3 (January 1994), 336–339.

[81] Shen, X., and Warhaft, Z. The anisotropy of the small scale structure in high Reynolds number $Re_\lambda \gg 1000$ turbulent shear flow. *Phys. Fluids 12*, 11 (2000), 2976–2989.

[82] Shen, X., and Warhaft, Z. Longitudinal and transverse structure functions in sheared and unsheared wind-tunnel turbulence. *Phys. Fluids 14*, 1 (2002), 370–381.

[83] Siggia, E. D. Numerical study of small scale intermittency in three dimensional turbulence. *J. Fluid Mech. 107* (1981), 375.

[84] Sreenivasan, K., Vainshtein, S., Bhiladvala, B., i. San Gil, Chen, S., and Cao, N. Asymmetry of velocity increments in fully developed turbulence and the scaling of low order moments. *Phys. Rev. Lett. 77*, 8 (August 1996), 1488–1491.

[85] Stolovitzky, G., Sreenivasan, K., and Juneja, A. Scaling functions and scaling exponents in turbulence. *Phys. Rev. E 48* (1993), R3217–R3220.

[86] Tabeling, P., and Willaime, H. Transition at dissipative scales in large-Reynolds-number turbulence. *Phys. Rev. E 65* (June 2002).

[87] Tabeling, P., Zocchi, G., Belin, F., Maurer, J., and Willaime, H. Probability density functions, skewness, and flatness in large Reynolds number turbulence. *Phys. Rev. E 53* (1996), 1613–1621.

[88] Tavoularis, S., and Karnik, U. Further experiments on the evolution of turbulent stresses and scales in uniformly sheared turbulence. *J. Fluid Mech. 204* (1989), 457.

[89] Tritton, D. *Physical Fluid Dynamics*, 2nd ed. Clarendon Press, Oxford, 1988.

[90] Tsinober, A. *An informal introduction to turbulence*. Kluwer Academic Publishers, 2001.

[91] van de Water, W., and Herweijer, J. Comment on "Extended self-similarity in turbulent flows". *Phys. Rev. E 51*, 3 (March 1995), 2669–2671.

[92] van de Water, W., and Herweijer, J. Anomalous scaling and anisotropy in turbulence. *Physica Scripta T67* (1996), 136–140.

[93] van de Water, W., and Herweijer, J. A. High-order structure functions of turbulence. *J. Fluid Mech. 387* (1999), 3–37.

[94] Wyngaard, J. Measurement of small-scale turbulent structure with hot wires. *J. Phys. E: Sci. Instrum. 1* (1968), 1105–1108.

[95] Wyngaard, J. Spatial resolution of the vorticity meter and other hot-wire arrays. *J. Phys. E: Sci. Instrum. 2* (1969), 983–987.

[96] Wyngaard, J. Spatial resolution of a resistance temperature sensor. *Phys. Fluids 14* (1971), 2052–2054.

[97] Yachot, V. Passive scalar advected by a rapidly changing random velocity field: Probability density of scalar differences. *Phys. Rev. E 55* (1997).

[98] Zhou, T., Antonia, R. A., and Chua, L. P. Performance of a probe for measuring turbulent energy and temperature dissipation rates. *Exp. Fluids 33* (2002), 334–345.

ACKNOWLEDGEMENTS

To fully describe how many things changed for me since my arrival four years ago in the Netherlands, it is a task that perhaps requires an amount of work comparable to that needed for completing this thesis. I can only think that most of the good things came from inside this wonderful group of people that I had the privilege to work with during all this time that maybe passed too quickly.

I would like to bring my warm thanks to our most treasured technicians that breathed new life in the old windtunnel: Gerard, Ad, Gerald, Freek, Jan, Herman and Gert; without your appetite for challenge, your engineering talent and especially large doses of Dutch patience and perseverance, nothing would have been possible. Special thanks go to Gerard and Gerald who were the first to encourage me to speak Dutch.

I would especially like to thank Willem for his daily course in experimental physics, for stimulating my intuition, for almost educating me in how to become a good physicist and many other academic-related aspects, but also for awakening my interest in (very contagious) turbulent activities: ice-skating and cycling.

I am grateful to GertJan, Gijs Ooms and Christos Vassilicos for their attent reading of the thesis and useful suggestions.

I sincerely thank ALL the students and PhD students that I met during my stay here for the unforgettable *borrels* and enthusiastic lunch discussions, wether they had a "subtle" political twist or they were filled with passion when it came to sharing personal interests. I would like to express my gratitude to our very efficient secretaries, especially Marjan, for being experts in softening cultural differences and in the art of Dutch know-how, both issues that foreign students fear when they are fresh to the Netherlands.

I would like to thank my dear friends that are there when needed, for quite some years now: Mada and Flo, George and Bogdan, Gabi, Vali and Ionela. For their utmost care, love and support, I am grateful to my brother Cristi and my parents.

CURRICULUM VITÆ

◊ **Born on January 8, 1974, in Craiova, România**

◊ **Secondary school "Fraţii Buzeşti", Craiova, 1985-1988**

◊ **Highschool "Nicolae Bălcescu", Craiova, 1988-1992**

◊ **Bachelor of Science in Physics, University of Craiova, 1992-1997**

◊ **Tempus Program Exchange Student, University of Swansea, Wales, 1995**

◊ **Master of Science in Theoretical Physics** (Quantum Field Theory and Gauge Fields), **University of Craiova, România, 1998**

◊ **Ph.D. in Physics, Department of Fluid Dynamics, University of Technology Eindhoven, 2002**

◊ starting January 2003 **Postdoc, Department of Fluid Dynamics, University of Twente**